



Title	Die-attach Bonding Process Using Metallic Microparticles for High-temperature Applications
Author(s)	Gao, Runhua
Citation	大阪大学, 2021, 博士論文
Version Type	VoR
URL	https://doi.org/10.18910/82246
rights	
Note	

The University of Osaka Institutional Knowledge Archive : OUKA

<https://ir.library.osaka-u.ac.jp/>

The University of Osaka

Doctoral Dissertation

**Die-attach Bonding Process Using Metallic
Microparticles for High-temperature
Applications**

GAO RUNHUA

January 2021

Graduate School of Engineering,
Osaka University

博士学位論文

金属マイクロサイズ粒子を利用した高温実装
用ダイアタッチ接合プロセス

GAO RUNHUA

2021年1月

大阪大学大学院工学研究科

Supervisor

Prof. Hiroshi Nishikawa, Ph. D.

Joining and Welding Research Institute

Osaka University

Doctoral Committee

Prof. Hiroshi Nishikawa, Ph. D.

Joining and Welding Research Institute

Osaka University

Prof. Soshu Kirihara, Ph. D.

Joining and Welding Research Institute

Osaka University

Prof. Yuji Ohishi, Ph. D.

Division of Sustainable Energy and Environmental Engineering

Osaka University

To my parents and my lovely wife

Contents

Contents	I
List of figures	V
List of tables	XI
Chapter 1 Research Background	1
1.1 Development of semiconductor materials for power devices	1
1.2 Die attach process and materials for high-temperature application	4
1.2.1 High-melting-temperature solders.....	4
1.2.2 Transient liquid phase (TLP) bonding.....	5
1.2.3 Metallic nanoparticle (MNP) bonding	10
1.3 Motion of the research.....	14
1.4 Theoretical basis and scope.....	14
1.4.1 Metallic microparticle (MMP) bonding	14
1.4.2 Redox reaction assist.....	16
1.4.3 Ultrasonic vibration assist	17
1.5 Scope of this study	18
References.....	20
Chapter 2 Bonding process using preoxidized Cu microparticles under formic acid atmosphere	29
2.1 Introduction.....	29
2.2 Experimental	30
2.2.1 Sample fabrication.....	30
2.2.2 Characterization	32
2.3 Result and discussion	32
2.3.1 Transformation of the Cu microparticles during preoxidation process.....	32
2.3.2 Transformation of the preoxidized Cu microparticles in formic acid atmosphere.....	38
2.3.3 Cu/Cu joints assembled with preoxidized Cu microparticles and the bonding mechanism.....	39
2.4 Conclusion.....	42
Reference.....	43
Chapter 3 Rapid ultrasonic-assisted bonding process using Ag microparticles under ambient atmosphere	45
3.1 Introduction	45

II

3.2	Experimental	46
3.2.1	Materials and sample fabrication	46
3.2.2	Method and processing	48
3.2.3	Characterization methods.....	49
3.3	Results and discussions.....	49
3.3.1	Effects of ultrasonic vibration on bonding process and sintered joints.....	49
3.3.2	Evolution of sintered microparticles under ultrasonic vibration	50
3.3.3	Effects of the ultrasonic vibration on the joint interfaces	56
3.3.4	Enhancing Mechanism of ultrasonic vibration on microparticle bonding	59
3.4	Conclusions.....	62
	Reference	63
	Chapter 4 Ultrasonic-assisted bonding process using organic-protected Cu microparticles	65
4.1	Introduction.....	65
4.2	Experimental	66
4.2.1	Sample fabrication	66
4.2.2	Testing and characterization	67
4.3	Results and discussion	68
4.3.1	Protective solvent and bonding parameters.....	68
4.3.2	Microstructures of joints assembled with ultrasonic-assisted bonding.....	75
4.3.3	Mechanism of microparticle bonding and its reinforcement	78
4.4	Conclusion	80
	Reference	82
	Chapter 5 Long-term reliability and failure mechanism of the joints assembled with metallic microparticles.....	85
5.1	Introduction.....	85
5.2	Experimental	86
5.2.1	Preparation of aged joint specimens	86
5.2.2	Characterization methods.....	87
5.3	Results and discussion	88
5.3.1	Shear strength of the joints assembled with different materials and processes.....	88
5.3.2	Microstructure transformation of the Cu/Cu joints obtained by reductive sintering of preoxidized Cu microparticles	89
5.3.3	Microstructure transformation of the Ag-sintered joints obtained with the ultrasonic process	93

5.3.4	Microstructure transformation of the Cu/Cu joints obtained by ultrasonic-assisted bonding method using organic-protected Cu microparticles.....	99
5.3.5	Effects of substrates, and bonding methods on the long-term reliability of Cu microparticle-sintered joints	101
5.4	Conclusions	103
	Reference.....	105
Chapter 6 Summary and future works.....		107
6.1	Summary	107
6.2	Environmental assessment on various die-attach materials and corresponding bonding processes	109
6.3	Future work	112
6.3.1	Optimization of the reductive sintering process.....	112
6.3.2	Improvement of the ultrasonic process and other antioxidation methods.....	112
6.3.3	Reliability assessment of proposed bonding processes for real application.....	113
	Reference.....	114
Research achievements.....		117
Acknowledgment.....		119

List of figures

Figure 1.1 Schematic of an IGBT power module.	4
Figure 1.2 A schematic illustration of the mechanical of the TLP process (a binary eutectic system is taken as an example) [40].	7
Figure 1.3 IMC growth and fracture positions at the (a-e) Cu-Sn and (f-j) Ni-Sn TLP bonded joints; (k) shear strength of Cu-Sn and Ni-Sn TLP bonded joints reduced with increasing bonding time, which cause thick IMC layers [52].	9
Figure 1.4 Transmission electron microscope (TEM) image of a single copper NP with a thick graphene layer of 3 nm (left) and a corresponding schematic illustration (right); (b) Thermogravimetric analysis (TGA) confirms the thermal stability of these NPs up to 165 [70].	12
Figure 1.5 Ellingham Diagram for Ag and Cu oxide [97].	15
Figure 1.6 A example illustrating formation of in-situ nanoscale structures and their sintering. (a) particles without oxidation, (c, d) in-situ nanoscale structures formed after oxidation, (e, f) sintering of nanoscale structures in formic acid atmosphere, (b) XRD patterns of the particles in (a), (c) and (e) [106].	17
Figure 1.7 Schematic diagram of stress reduction due to excitation of acoustic softening and stress superposition [111].	17
Figure 2.1 The Cu parent microparticles used in this study.	30
Figure 2.2 Illustration of paste and bonding specimen fabrication.	30
Figure 2.3 The heating profile of the bonding process.	31
Figure 2.4 Schematic diagram of the bonding machine.	31
Figure 2.5 TG and DTA curves of the (a) Cu microparticles and (b) as-fabricated paste mixed preoxidized Cu microparticles with 15 wt.% terpineol.	33
Figure 2.6 Microstructural changes in Cu microparticles preoxidized at 280 °C for : (a, b) 0 min, (c, d) 10 min, (e, f) 20 min, (g, h) 30 min, and (i, j) 40 min.	35
Figure 2.7 XRD pattern of Cu microparticles preoxidized at 280 °C for different periods.	36
Figure 2.8 The average thickness of oxide layers on Cu microparticles preoxidized at 280°C for different time.	37
Figure 2.9 Schematic diagram of transformation on Cu microparticle surfaces.	37
Figure 2.10 Transformation of the preoxidized Cu microparticles by formic acid atmosphere: (a-c) schematic diagram, and (d) a SEM imgae of the Cu microparticles preoxidized for 30 min and reduced	

VI

for 30 min.....	39
Figure 2.11 Shear strength of bonded Cu/Cu joints assembled at 300 °C under different conditions: (a) 0, 10, 20, 30, and 40 min of preoxidation + 30 min of reductive sintering and (b) 30 min of preoxidation + 10, 20, 30, and 40 min of reductive sintering.	40
Figure 2.12 The Cu/Cu joints assembled by reductively sintering 30-min preoxidized Cu microparticles at 300 °C for 30 min: (a) XRD pattern of the sintered matrix, (b, c) cross-sectional SEM images of the joints, and (d, e) fracture surface of the joints showing linkages between microparticles.	40
Figure 2.13 The transformation of the Cu microparticles after different process: (a) schematic diagram, and (b) corresponding SEM images.....	41
Figure 3.1 Materials used in this study: (a) the chestnut-burr-like Ag microparticles, and (b) a schematic of the joint specimen.....	46
Figure 3.2 Thermal properties of (a) the Ag paste with temperature rising from 20 – 500 °C, and (b) the Ag paste at different constant temperatures and atmosphere.....	47
Figure 3.3 Joint specimen fabrication: (a) schematic diagram of the modified ultrasonic-assisted bonding machine, and (b) the heating profile of the process.....	48
Figure 3.4 Real-time actual temperatures when the specimens were assembling at 300 °C by the non-ultrasonic process and the ultrasonic process with an ultrasonic power of 8 W.....	50
Figure 3.5 Shear strength of the joints assembled at setting temperature of 300 °C for 250 s with (a) an ultrasonic power of 8 W and various ultrasonic time, and (b) an ultrasonic time of 250 s and various ultrasonic power.	51
Figure 3.6 Fracture surfaces and cross sections of the joints assembled at a setting temperature of 300 °C with a fixed ultrasonic power of 8 W and ultrasonic time of (a, f) 0 s, (b, g) 50 s, (c, h) 100 s, (d, i) 150 s, and (e, j) 250 s.....	52
Figure 3.7 Fracture surfaces and cross sections of the joints assembled at a setting temperature of 300 °C with a fixed ultrasonic time of 250 s and ultrasonic power of (a, g) 1 W, (b, h) 2 W, (c, i) 3 W, (d, j) 6 W. (see 0 W and 8 W in Figure 3.6 (a, f) and Figure 3.6 (e, j), respectively)	53
Figure 3.8 Microstructural evolution of the Ag microparticles in the ultrasonic process (250 s, 8 W): (a) stages presented in (b - k), and fracture surface (left column) and cross-section (right column) SEM images of the joints after (b, c) 50 s, (c, d) 100 s, (e, f) 150 s, (g, h) 200 s and (i, j) 250 s of the process.	54
Figure 3.9 Cross-sectional SEM images, EBSD OIMs, and distributions of grain size of the joints	

assembled at 300°C for 250 s by (a, b, c) the non-ultrasonic process and (d, e, f) the ultrasonic process (250 s, 8 W).	55
Figure 3.10 STEM image showing the micro bridges formed with the ultrasonic process (250 s, 8 W). Ag twins were identified by [110] diffraction pattern at the white circle.....	55
Figure 3.11 Cross-section images of the joints assembled at 300 °C for 250 s by (a, d, g) the non-ultrasonic process and the ultrasonic process with an ultrasonic time of 250 s and an ultrasonic power of (b, c, h) 3 W, and (c, f, i) 8 W.	56
Figure 3.12 Elements distribution of the interfaces obtained at 300 °C with an ultrasonic power of 8 W and an ultrasonic time of 250 s at (a) the upper interface and (b) the bottom interface.	57
Figure 3.13 Cross-section STEM images showing interfaces of the joint assembled at 300 °C with an ultrasonic power of 8 W and an ultrasonic time of 250 s: (a) the upper interface and (b) the bottom interface, and (c) EDS line scanning in (a).	58
Figure 3.14 SEM images showing fracture positions of the joints assembled at 300 °C by (a, b) the non-ultrasonic process and the ultrasonic process with an ultrasonic power of (c, d) 3 W and (e, f) 8 W.	59
Figure 3.15 Schematic diagram illustrating the formation of dense layers in the ultrasonic process.....	61
Figure 4.1 Schematic diagram of (a) the paste fabrication and (b) the joint specimen. (R. T.: room temperature).	66
Figure 4.2 Influence of protective solvents on shear strength of joints: (a) shear strength of joints assembled using different protective solvents, and (b) heating profile used to prepare joints for this solvent test. (TA: α -Terpineol + L-ascorbic acid; GA: glycerol + L-ascorbic acid).	69
Figure 4.3 DSC and TG curves of the as-fabricated paste with temperature rising from 20 – 500 °C at a rate of 20 °C/min in the air.	70
Figure 4.4 Figure 4.4 DSC curves of the pastes with different protective solvents in the air or N ₂ atmosphere at a fixed temperature of 200 °C: (a) glycerol + N ₂ , (b) glycerol + air, (c) L-ascorbic acid and glycerol + N ₂ , and (d) L-ascorbic acid and glycerol + air.	71
Figure 4.5 Influence of total process time on (a) shear strength and (b) oxide and carbon content of the joints, and (c) profile used to prepare joints for this trial.	72
Figure 4.6 Influence of ultrasonic time and pressure on the joints: (a) Shear strength of the joints assembled with different ultrasonic time and pressure, and (b) heating profile used to prepare joints for this test.	74
Figure 4.7 Optimized profile of the process and the measured actual temperature of the joint specimen	

VIII

during heating without ultrasonic vibration.....	74
Figure 4.8 Fracture surfaces of joints assembled under a pressure of 7 MPa by (a) non-ultrasonic process and (b) by ultrasonic process, and under a pressure of 14 MPa by (c) non-ultrasonic process and (d) by ultrasonic process. (US: ultrasonic vibration).....	75
Figure 4.9 Cross-sectional SEM images of joints assembled under a pressure of 7 MPa by (a) non-ultrasonic process and b) by ultrasonic process, and under a pressure of 14 MPa by (c) non-ultrasonic process and (d) by ultrasonic process, and (e) EDS results of different regions marked in the images. ...	76
Figure 4.10 STEM images show (a) the bonding interfaces between the Cu microparticles, (b, c, and e) enlarged view of the marked area in the image (a), and (f) EDS line scanning result of the marked area in image (b).	78
Figure 4.11 Schematic diagram illustrating (a) densification in a macroscopic view, and (b) dynamic recrystallization occurred at deformed micro region in a microscopic view. (IGB: interfacial grain boundary, DR: Dynamic recrystallization)	79
Figure 5.1 Joint samples prepared with different conditions after ageing for various time intervals.....	87
Figure 5.2 Shear strength of the #1 - 4 joints after the aging for different time intervals.	88
Figure 5.3 Fracture surfaces of the #1 joints after aging for different time intervals.	90
Figure 5.4 Debonding of the sintered matrix of #1 joints after aging for 1008 h: (a) schematic diagram, and (b) SEM images of the detached surfaces on (b) the upper disk, (c) upper area of the sintered matrix, (d) bottom area of the sintered matrix, and (e) the bottom disk.	91
Figure 5.5 Cross-sectional SEM images of the #1 joints after aging for different time.	91
Figure 5.6 TEM of bonding interface of the #1 joint after aging for 504 hours: (a) STEM images, (b) enlarged view in image(a), and (α , β) diffraction pattern of the areas marked by white points.	92
Figure 5.7 Schematic diagram of failure modes of the #1 joints (a) before and (b) after aging, and (c) voids formation during aging.....	93
Figure 5.8 Fracture surfaces of the #3 joints after aging for different time.	94
Figure 5.9 Cross-sectional SEM images of the #3 joints after aging for different time.	95
Figure 5.10 Porosity and size of voids (average diameters) with increasing aging time.....	96
Figure 5.11 Schematic diagram of failure modes of #3 joints after aging.	97
Figure 5.12 EPMA results of the #3 joint after aging for different time.....	98
Figure 5.13 Fracture surfaces of the #4 joints after aging for different time.	99
Figure 5.14 Cross-sectional SEM images of #4 joints after aging for different time	100

Figure 5.15 Schematic diagram of the fracture mode of the #4 joints before (a, c) and after aging (b, d).
..... 101

Figure 5.16 EMPA results showing element distribution at bonding interfaces of #1 and #2 joints before
and after aging for 504 h..... 102

List of tables

Table 1.1 Some physical properties (at 300 K) of typic semiconductors of three generations [4, 11-14]. 3

Table 1.2 Different forms of materials used in the TLP process [48-54].....8

Table 1.3 Comparison of the three die-attach bonding methods..... 14

Table 3.1 Relationship between ultrasonic amplitude and output power of the bonding device.48

Table 4.1 Solvents and reductive agents used for the bonding process using Cu in the air atmosphere [1-8].....68

Table 5.1 Different process and conditions used in this study to obtain bonding joints.....86

Table 6.1 Comparison of various die-attach materials in term of the environmental perspective [2, 3, 7-9]..... 110

Table 6.2 Comparison of various die-attach process [2, 3, 7, 10, 11]..... 111

Chapter 1

Research Background

1.1 Development of semiconductor materials for power devices

Nowadays, human activities highly rely on electrical appliances for living, manufacturing, and transportation, promoting development in power semiconductor devices that regulate the flow of electricity [1]. As power devices usually serve systems that is operated over a broad spectrum of power levels and frequencies, semiconductors used in such devices require a wide bandgap to maintain stability under high-switch-speed, high-voltage, high-current, and high-temperature serving condition [1, 2]. As the base materials, semiconductors greatly affect the performance of power devices. For example, the highest breakdown voltage capability of a Si-based insulated gate bipolar transistor (IGBT) is 6.5 kV, and it can only operate at a temperature below 200 °C, due to the limitation of Si properties [3]. Fortunately,

with developments of materials science, there have been considerable breakthroughs in semiconductors, which recently have been developed into the third generation:

- i) First generation: elemental semiconductors, such as silicon (Si) and germanium (Ge). Due to their process maturity and well-controlled cost, they have served commercially for over 50 years. However, they do not have ideal device characteristics [1], because their relatively narrow energy gaps (bandgaps) induce some drawbacks (such as low voltage blocking capability, etc.) and limit their performance in power devices [2].
- ii) Second generation: compound semiconductors, such as: GaAs, InP, and GaAsP. They were expected to be applied in high-speed supercomputers, while Si semiconductors with water cooling could compete with them [4]. Recently, they are widely researched for optoelectronic terahertz devices [5-7].
- iii) Third generation: wide bandgap (WBG) semiconductors, such as: SiC, GaN, and AlN. They exhibit wide bandgaps, high thermal conductivities, high breakdown field, high electron mobility, and excellent chemical stability; thus, they have shown great potential and become available recently in applications of power devices, especially for automobile and switching [8-10].

Physical properties (at 300K) of some typical semiconductors are shown in **Table 1.1**. It is worth noting that properties of compound semiconductors are very dependent on temperatures and their impurities [4]. From **Table 1.1**, it is evident that 4H-polytype SiC, a typical WBG semiconductor, exhibit three times of energy gap comparing with Si, and its breakdown field is also one order of magnitude larger. Therefore, WBG semiconductors could serve under more complex operating conditions, allowing power devices to operate in environments with high voltage and temperatures over 400 °C.

Due to their superior properties, WBG semiconductors are expected to be adopted industrially for next-generation power devices and now have been widely used in components such as IGBT modules [15], semiconductor field-effect transistors (MOSFETs) [16], field-effect transistors (FETs) [17], high electron mobility transistor (HEMT) [18], etc. An IGBT module, as shown in **Figure 1.1**, is taken for example, which represents the most commercial and advanced electronic devices that are increasingly applied into power supply applications. The IGBT die is the most critical core in the device system; other components such as heat sink, encapsulant, and metalized substrate fix the die and maintain its efficiency. a die-attach layer is applied between semiconductors and substrate, attaching dies to metalized substrates

Table 1.1 Some physical properties (at 300 K) of typic semiconductors of three generations [4, 11-14].

Materials	1st generation		2nd generation		3rd generation	
	Si	Ge	GaAs	InP	4H-SiC	GaN
Energy gap (eV)	1.1	0.7	1.4	1.4	3.0	3.4
Thermal conductivity ($\text{W}\cdot\text{cm}^{-1}\cdot\text{K}^{-1}$)	1.4	0.6	0.5	0.7	4.9	1.3
Breakdown field ($10^8\cdot\text{V}\cdot\text{m}^{-1}$)	0.3	0.1	0.7	0.5	3.5	~5
Electron mobility ($\text{cm}^2\cdot\text{V}^{-1}\cdot\text{s}^{-1}$)	1400	3800	8500	6060	1000	≤ 1000
Dielectric constant (static)	11.9	16.2	13.2	12.6	9.7	8.9
Reference	[4, 11]	[4, 12]	[4]	[4, 12]	[13]	[13, 14]

and achieving a bonding with excellent thermal and electrical conductivity by some packaging processes; therefore, it is remarkably essential for system stable operation.

As devices using WBG semiconductors are geared towards high-load and high-temperature applications, their die-attach layers, as the critical connects providing thermal, electrical, and mechanical support, also serve under such severe conditions; therefore, die-attach materials need to meet the rather stringent requirements, including good ductility and conductivity, relatively high solidus (260 °C or higher) and liquidus temperatures (400 °C or higher), and excellent corrosion resistance, thermal-cycle reliability, and thermo-mechanical fatigue resistance [19, 20]. Low-cost materials that meet the requirements in the solidus temperature, liquidus temperature, and conductivity are especially favorite. Another issue is the long-term reliability of die-attach materials for high-temperature applications: the interfaces forming between die-attach materials and metallization layers of chips and substrates should have long-term chemical and mechanical stabilities [21].

Based on these requirements, many satisfying die-attach materials, as well as corresponding die-attach methods, have been researched. The processes used in most common die-attach methods including the soldering method (reflow), transient liquid phase (TLP) bonding method, and sintering of metallic nanoparticles (MNPs), will be discussed accordingly to categories in the next section.

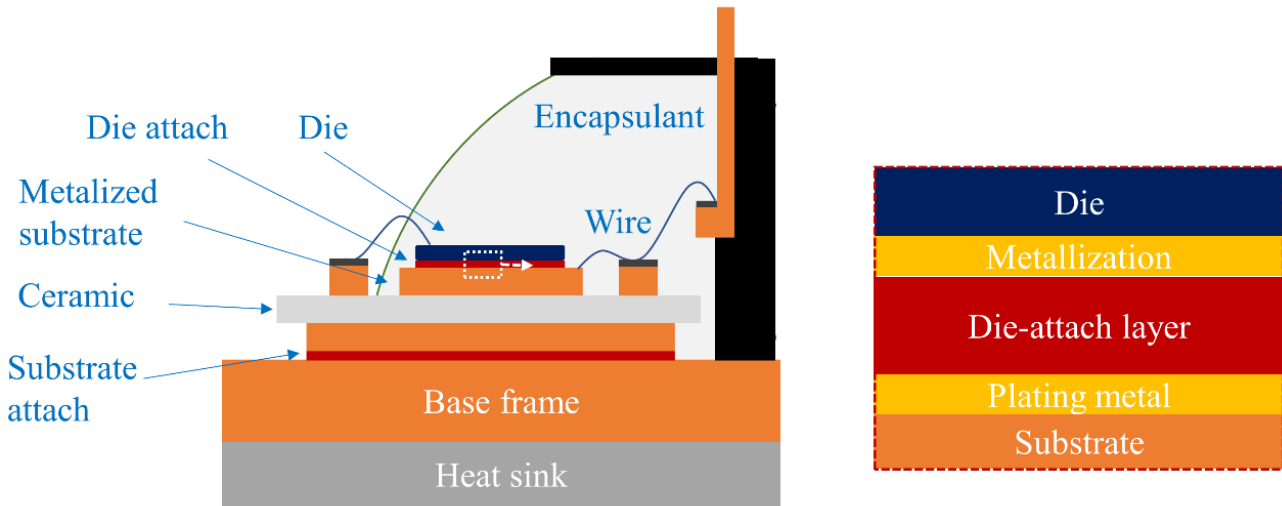


Figure 1.1 Schematic of an IGBT power module.

1.2 Die attach process and materials for high-temperature application

1.2.1 High-melting-temperature solders

High-Pb solders (Pb-based solders containing 85 wt.% or more lead) are generally utilized as die-attach materials for power devices in applications such as automatics and aerospace. However, the Restriction of Hazardous Substances (RoHS) directive adopted in 2003 by the EU prohibits the use of certain hazardous substances, including Pb, in electrical and electronic equipment [22]. Although high-temperature solders were exempted from the RoHS directive [23], the recast of the RoHS directive (RoHS2) passed in 2011 set deadlines for eliminating exemption of high-Pb solders without acceptable alternatives [22]. Considering the impending deadlines, many researchers have developed and evaluated various Pb-free solders for power devices, including Au-based solders, Zn-based solders, Bi-based solders, etc.

Au-based solders generally exhibit high stiffness, excellent resistance to thermal fatigue, and creep fracture, while the relatively high costs in both solder fabrication and soldering facilities limit their applications [24]. Among them, Au-Sn solders are the most used solders for high-temperature applications for its excellent mechanical properties, superior corrosion resistance, and feasibility of fluxless soldering [25]. However, due to their high stiffness, they hardly accommodate thermal stress, which could be transferred to chips and cause damages; therefore, Au-Sn solders are unsuitable for application in large modules. Au-Ge solders are also promising candidates for high-temperature applications, which possess no IMC phase. But, their high melting temperatures (e.g., Au₈₈Ge, 356 °C) limit their applications, as few modules could withstand such high processing temperatures. Nevertheless, it has been reported that

the addition of low melting point metals such as In, Sb, and Sn to Au-Ge solders could bring down melting temperatures and improves ductility [26].

Zn-base solders have risen attention in high-temperature applications because of their low cost and possibility of mass manufacturing. Among them, Zn-Sn solders have been believed to be the best substitute due to their excellent ductility, mechanical properties, electrical properties, thermal properties, and minimal formation of IMCs [27-29]. The shear strength behavior of Zn-Sn solders with different Sn contents has been investigated [30], and their electrical properties and oxidation resistance also have been proven [31, 32]. Furthermore, researchers have tried the addition of metals such as Al and Mg to improve further their reliability [29, 32, 33].

Bi-based solders are alternative solutions for high-temperature applications. Among them, Bi-Ag solders, such as Bi2.5Ag and Bi11Ag solders, are promising choices because their acceptable liquidus temperatures (e.g., 262.5 °C, Bi2.5Ag) [34], proper stiffness, and reasonable cost. However, due to their inferior conductivity and workability, the development of Bi-Ag solders is still ongoing [35]. Lalena et al. have composited Bi-11Ag-0.5Ge alloys to improve thermal conductivity, while the wettability of the solder remains inferior [36].

In summary, although many solder materials are promising and acceptable solutions for high-temperature applications (some typical high-temperature solders are listed in **Table 1.2**), while they are more or less limited by their properties in many application scenarios. Since there is no cost-effective high-temperature solder that could fully replace Pb-contained solders, the development of new materials and bonding methods are gaining attention.

1.2.2 Transient liquid phase (TLP) bonding

The transient-liquid phase (TLP) bonding, patented in 1971 [38], is a process that is now widely used to joining high melting point alloys at relatively low temperatures, which combines the characteristics of liquid-phase joining and diffusion bonding [39]. Like soldering, the TLP employed an alloy as an interlayer material, which melts and then solidifies to form a bond joining surfaces together. The difference is that soldering completes melting and solidification steps by temperature changes, while the TLP forms a liquid interlayer spreading two joining surfaces and a solid joint at a constant temperature; namely, the TLP is an isothermal process, and the interlayer melts and solidifies due to interdiffusion with the base material [40]. Eutectic alloy systems are mostly applied in the TLP process since the liquidus temperature of a eutectic alloy decreases during alloying. Taking a simple binary eutectic system as an

Table 1.2 Comparison of typical solders for high-temperature applications. T_m : liquidus temperature, CTE: coefficient of thermal expansion [22, 36, 37].

Materials	T_m (°C)	CTE (ppm/K)	Modulus (GPa)	Reference
Au20Sn	280	16	68	[37]
Au12Ge	356	12	-	[37]
Zn30Sn	360	30	-	[22]
Bi11Ag	360	-	13.28	[36]

example, we usually divide the TLP process into four distinctly different stages [40, 41]; these stages are assumed to occur sequentially for ease of understanding, as illustrated in **Figure 1.2**:

- i) Substrate dissolution
- ii) Homogenization
- iii) Isothermal solidification
- iv) Solid-state homogenization

During the substrate dissolution stage, a metal B is assembled between two pieces of metal A (**Figure 1.2 a**) and melts when the temperature rises to a specific point T_B , which is lower than the melting point of the metal B. The melting of B is attributed to interdiffusion at interfaces, which mixes the metal A and B atoms to form an interlayer. As a result, as shown in the phase diagram in **Figure 1.2 b**, the composition of the interlayer at interfaces changes, and the interlayer starts to melt at interfaces when the concentration reaches C^{La} . This process could occur very fast and be characterized as a widening of melted interlayer into substrates.

Since the interlayer first melts at interfaces when the central part of the interlayer is still solid, the liquid is inhomogeneous and supersaturated. Therefore, in the homogenization stage, it will continue dissolving interlayer, widening the liquid zone towards to center. In this stage, the interlayer completely melts to liquid, and its composition homogenizes via diffusion. If the TLP process stays in this stage for sufficient time, the gradient of concentration in the liquid will be eliminated, and the concentration profile becomes flat, reaching the equilibrium value C^{La} , as shown in **Figure 1.2 c**.

In the isothermal solidification stage, metal B atoms in liquid start to diffuse into metal A substrates, and the melting point of the liquid at solid/liquid interface consequently raises, induce solidification occurs. As shown in **Figure 1.2 d**, a local equilibrium is maintained at the solid/liquid interfaces; therefore, the liquid zone narrows until completely solidifies with the diffusion of metal B atoms in metal A, while

process temperature still maintains at T_B (**Figure 1.2 d**). This stage is a slow process since it relies on solid-state diffusion of metal B atoms.

Finally, homogenization occurs after the complete solidification of interlayers when process temperature is still holed at T_B , as shown in **Figure 1.2 d**. Just like the isothermal solidification step, the homogenization of solid joint relies on long-range solid-state diffusion of A and B atoms and is a slow process. It is worth noting that the ideal TLP model we described above uses a eutectic system, while not all TLP interlayers are eutectic formers [41].

Because of the characteristic that the bonding interlayer has a higher melting point than the process temperature, the TLP bonding method has been widely used to bond high-melting materials at relatively low temperatures [42]. The interlayer materials used for the TLP process could be many different forms, such as pastes, electroplating, foils, and powders, as listed in **Table 1.3**. Because Cu is widely used as a metallization layer on ceramic substrates for power devices (e.g., direct bonding copper (DBC)), Sn-Cu binary eutectic system has become a popular TLP system and been most researched. Chu et al. compared Cu-Sn and Ni-Sn sandwich TLP structure system, indicating Cu-Sn joints are more reliable and reveal exceptionally smooth fracture surfaces [43]. Boscoand and Zok investigated critical interlayer thickness

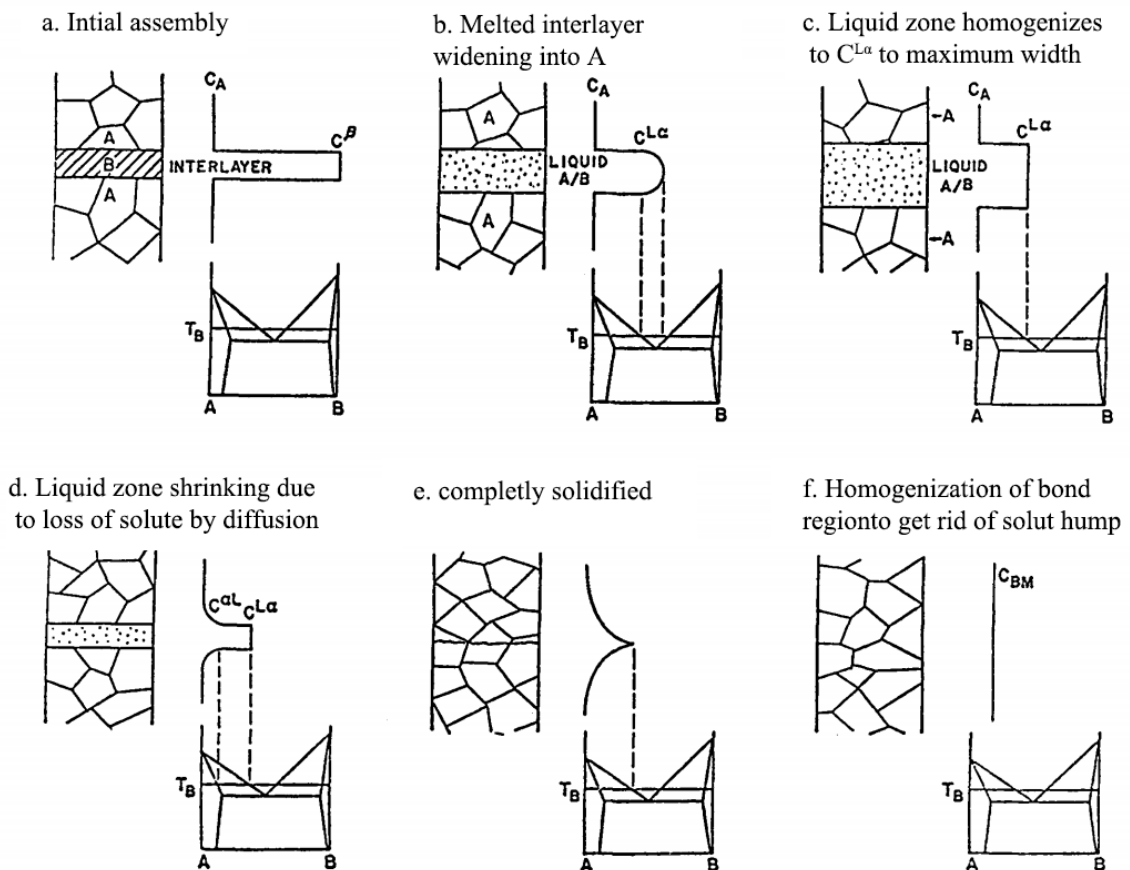


Figure 1.2 A schematic illustration of the mechanical of the TLP process (a binary eutectic system is taken as an example) [40].

for averting pore formation in the Cu-Sn TLP system and provide an optimized thickness to ensure robust bonds at minimum bonding time [44]. Li et al. studied interfacial microstructures and diffusion-kinetic constants for the Cu_6Sn_5 and Cu_3Sn growth in a Cu/Sn/Cu sandwich TLP system [45]. Marauska et al. utilized Sn to attach micro-electro-mechanical system (MEMS) chips electroplating Cu and Au, confirming the hermeticity and reliability of the TLP bonding method in practice. Liu et al. introduce ultrasonic vibration into TLP bonding, finding Cu-Sn intermetallic joints were rapidly formed, and grains were remarkably refined [46]. Rajendran et al. recently developed a novel transient liquid phase bonding material by consequent electroless plating of Cu and Sn on a multi-walled carbon nanotube, obtaining a well-packed voidless TLP joint with a shear strength of 35.3 MPa [47].

The TLP bonding method also has apparent drawbacks. First, ideal isothermal homogenization is difficult to achieve, hence the inevitable formation of secondary phases. A long solid-state homogenization time is inevitable to eliminate the second phase [41]. The second drawback is that joints obtained by the TLP bonding method mainly composed of IMCs, which is fragile and could cause reliability issues [55]. For example, Byung-Suk Lee et al. found the mechanical strength and reliability of Cu-Sn and Ni-Sn TLP bonding reduced when the joints were fully transformed into $\text{Cu}_6\text{Sn}_5/\text{Cu}_3\text{Sn}$, and shear strength reduced with increasing bonding time, as shown in **Figure 1.3** [52]. The relationship between the thickness of IMC layers and time could be expressed as Fick's law [56]:

$$\Delta x^2 = Dt \quad (1.6)$$

Where D is interdiffusion coefficient, which could be calculated by Arrhenius relation:

$$D = D_0 \exp\left(\frac{-Q}{RT}\right) \quad (1.7)$$

Table 1.2 Different forms of materials used in the TLP process [48-54].

Interlayer materials	Material forms	Substrates	References
Sn-Bi + Cu particles	Paste	Cu	[48]
Sn-coated Cu	Paste	Cu	[49]
Ni-P	Thin foil	Ni	[50]
Sn	Sheet	Ni	[51]
Sn	Electroplating	Cu, Ni	[52]
Sn	Electroplating	Cu, Au	[53]
Sn-coated Cu	Powders	Cu	[54]

D_0 : intrinsic diffusivity

Q : activation energy

R : Boltzmann constant

T : temperature in Kelvin degree

It is evident from **Eq. (1.6, 1.7)** that the thickness of IMC layers increased with increasing time and serving temperature, so the thermal stability of TLP joints could be an issue. The third drawback is that in dissolution state, interlayer materials that are not completely consumed by substrate have low melting points may cause components to fail at high temperatures [57]. Therefore, studies for alternatives to overcome these drawbacks have been a hot spot in the microelectronic packaging for power devices.

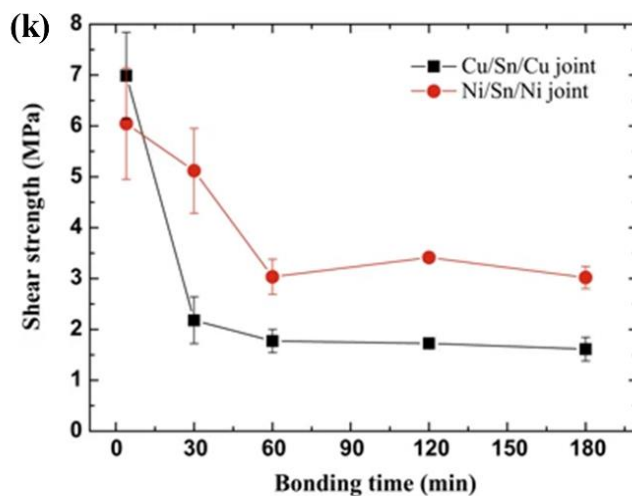
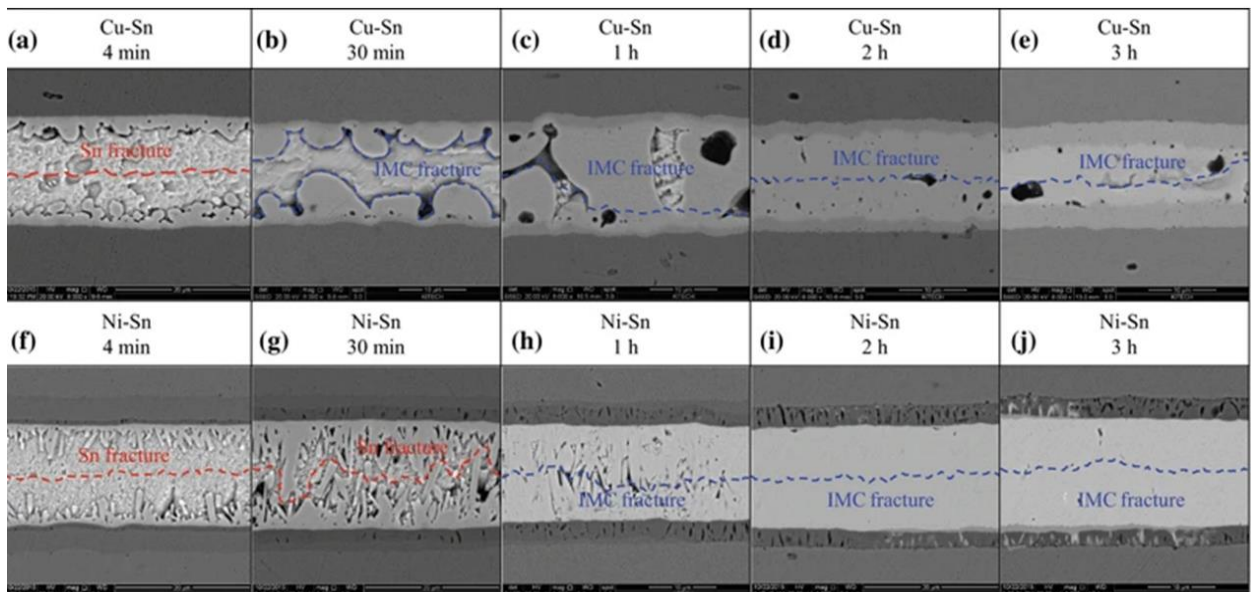


Figure 1.3 IMC growth and fracture positions at the (a-e) Cu-Sn and (f-j) Ni-Sn TLP bonded joints; (k) shear strength of Cu-Sn and Ni-Sn TLP bonded joints reduced with increasing bonding time, which cause thick IMC layers [52].

1.2.3 Metallic nanoparticle (MNP) bonding

In recent years, the sintering process using metallic nanoparticles (hereinafter referred to as MNP bonding) has emerged as a promising die-attach process because of its capability of assembling one-metal-system joints with high melting points at relatively low temperatures. This characteristics may avoid the formation and growth of IMCs. Unlike soldering and the TLP bonding that relies on the formation of IMCs, MNP bonding is a solid-state material transport process based on atomic diffusion driven by the reduction of total surface energy and/or interfacial energy [58]. The principle of this method is to increase the total surface energy by decreasing the total surface area of the particles; namely, particles significantly reduced in the melting point when the particle size decreased to nanoscales, and they could be readily sintered at low temperatures to assemble a sintered joint [59]. The essence of the sintering at low temperature is the process that high-energy free surfaces transformed into low-energy grain boundaries and later would be eliminated due to grain growth. The atoms on particle surfaces, which are different from atoms inside particles, possess unsaturated bonds on exposed surfaces. The sum of these unsaturated bonds is called total surface energy, and the ratio of the total surface energy to the particle surface area is the specific surface energy. It is convincible that in a surface atom, the unsaturated bonds increase with the increase of particle curvature, that is, the specific surface energy increases with the decrease of particle size [58, 60]. Additionally, with the total volume fixed, the reduction in particle size could increase both the number of particles and the total surface area. In addition to reducing particle size, surface treatments, such as ion surface activation, could also be used to increase total surface energy [61], while their commercial applications are limited due to the strict process environment required and high cost.

Different ideal model and behaviors could explain the sintering of nanoparticles according to their shapes and size, but generally, solid-state sintering could be expressed by three distinct stages [62]:

- i) Initial stage: includes formation of sintering necks, which is mainly attributed to surface material transport between particles.
- ii) Intermedia stage: includes densification of sintering structures and interconnection of pores.
- iii) Final stage: pore isolation.

For ease of understanding, we assume particles involved in sintering are all spherical particles of the same size and illustrate the transformation of sintered microstructures as follows.

In the initial stage, the sintering model could be divided into two cases when the sintering neck formed according to whether shrinkage occurs between particles. In the former case, distances between

particles barely change when the sintering necks' diameter increases; in the lateral case, distances between particles decrease with the increasing diameter of sintering necks. The primary driven forces for the sintering neck formation are differences in bulk pressure, vacancy concentration, and vapor pressure between particle surfaces, which induce material transport [62]. Major material transport paths include lattice diffusion, grain boundary diffusion, surface diffusion, viscous flow, etc. According to different parameters such as particle size and shapes, dominant material transport paths could differ.

When sintering necks have formed between particles, as sintering proceeds, it comes to the intermediate stage. In this stage, the density of sintered structures would be significantly increased, and pores between particles merge or disconnected from each other to become larger and independent. Coble developed two models to describe this process: the channel pore and the isolated pore model [63, 64]. After pore isolation, namely in the final stage, continuous sintering further reduces pore size (interparticle distance) and achieve higher density. It is reported that applying extra pressure after pore isolation could increase the density of sintered structures, even to full densification due to the change of densification mechanism [65].

Generally, conductivity and reliability are the most concerning qualities of die-attach bonding; therefore, Ag and Cu nanoparticles are generally believed to be promising materials for the bonding methods, due to their excellent thermal and electrical conductivity, and reasonable mechanical performance [66, 67]. The major challenge of reduction in process temperature, as mentioned, has faded with the development of nanoparticle fabrication. The MNPs are usually fabricated by wet chemical processes, with organic layers coated on their surfaces to protect them from oxidation and aggregation [68, 69]. When the temperature rises to a certain point, the organic layer is supposed to decompose or be consumed to avoid hindering sintering. For example, as shown in **Figure 1.4**, Luechinger et al. synthesized Cu nanoparticles that were in-situ coated with protective shells of graphene, which gasify in the lateral process [70]. Yan et al. prepared polyvinylpyrrolidone coated Ag nanoparticle as a paste for pressureless bonding [71]. They indicated that polyvinylpyrrolidone could prevent the coalescence of Ag nanoparticles and decompose when heating in the air. Then, by using polyvinylpyrrolidone as a solvent, Jianfeng et al. prepared a Cu nanoparticle paste, which was successfully sintered to assemble a Cu-sintered joint in the air [72]. Despite many similarities between Ag and Cu nanoparticle paste, they have their advantages and drawbacks and thus been applied in different scenarios.

The MNP bonding using Ag nanoparticle for electronic packaging was patented in 1989 by Schwarzbauer [73], and later was optimized to a faster process [74]. Nowadays, the Ag nanoparticle is

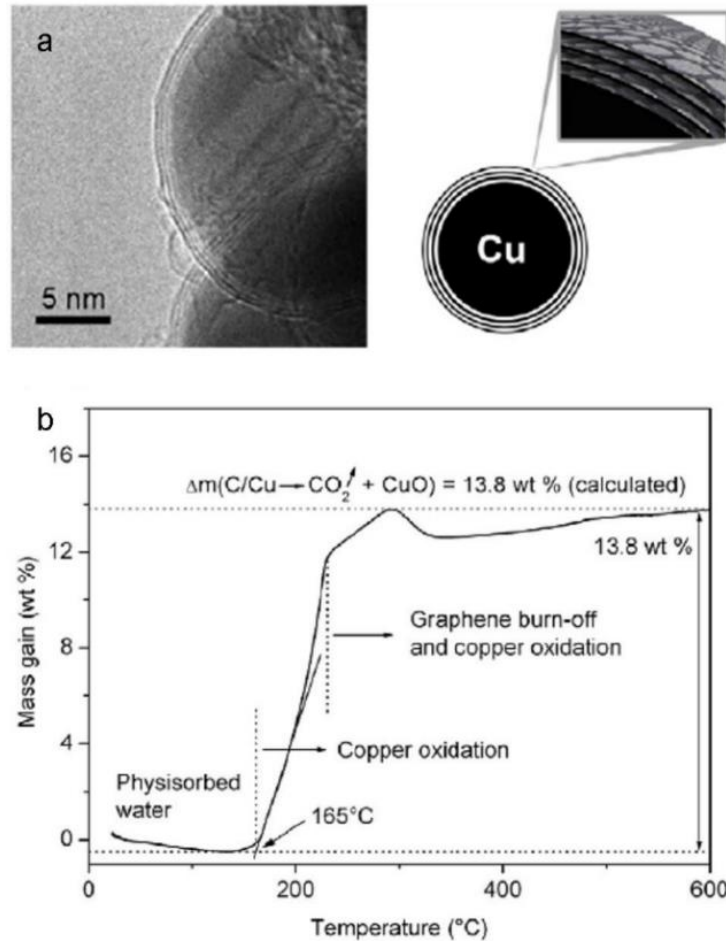


Figure 1.4 Transmission electron microscope (TEM) image of a single copper NP with a thick graphene layer of 3 nm (left) and a corresponding schematic illustration (right); (b) Thermogravimetric analysis (TGA) confirms the thermal stability of these NPs up to 165 [70].

the most popular material for MNP bonding methods and has been widely researched. Alarifi et al. fabricated sintered Ag nanoparticles to bond copper wire to copper foil at low temperatures down to 160 °C [75]. Wang et al. sintered the citrate-coated Ag nanoparticle paste to assemble Ag-sintered joints with an average shear strength of ~25 MPa, finding that sintering of the Ag nanoparticles would not be hindered once chemical bonds that connect the organic shells with the Ag nanoparticles are broken [76]. This is an interesting finding because most researchers believe that residue of organic shells hinders sintering and try to decompose them during processes as much as possible. They then thinned the organic shells, obtained Ag sintered joints at 150-200 °C in a very short period with high shear strength [77]. Yan et al. prepared an Ag nanoparticle paste based on the polyol method and investigated sintering behaviors of Ag nanoparticles at different bonding pressure [78]. Chua and Siow studied long-term reliability of sintered Ag joint and investigated oxidation behaviors of joints obtained with DBC and Ag-plated substrates [79]. They claim that bonding formed at nanoparticle/substrate interface could be attributed to common Ag oxide formation.

Although Ag sintering bonding exhibits adequate mechanical properties and oxidation resistance, its

poor electromigration resistance at high current densities limits its commercial application in high current circumstances [80]. The electromigration, which was first reported in 1861, refers to the phenomenon that metal atoms move with electrons when an electric field is applied to the metal [81]. Many researchers have reported that the electromigration induces voids in metal interconnects, which raise reliability concerns for semiconductors in high-current or high-power applications [82-84]. Additionally, as mentioned in *Chapter 1.2.1*, DBCs are widely used as substrates for power semiconductors in high-temperature applications. However, it is difficult for Ag MNP to bond with tenacious oxide layers on DBC substrates. It has been reported that Ag substrates provide the best sintering interfaces for Ag nanoparticle sintering due to their similarity in atomic spacing [79], and noble metals are generally electroplated on substrates as metallization. Therefore, despite excellent performance in conductivity and mechanical performance, the Ag-sintered joint is not the most perfect and favorable in industries for high-current power devices.

Since Cu shows extraordinary conductivity and resistance to electromigration [80], the MNP bonding using Cu nanoparticles has emerged recently. In many cases of Cu-sintered joints, metallization of both substrates and semiconductors, which is also referred to as contact metals, contains only Cu, making the bonded structure a single-metal bonding joint (hereinafter referred to as Cu/Cu joints). Zinn et al. used Cu nanoparticles that can be processed around 200 °C to package fully functional LED test boards [85]. Schnabl et al. use Cu nanoparticles to assemble functional LED test boards and a small camera board with a 48 pad CMOS sensor quad-flat no-lead chip and a 10 in flexible electronics demo [86]. They have proven its feasibility in industries. Li et al. achieved a reliable Cu/Cu joint by sintering Cu nanoparticles with an average size of 60.5 nm in an Ar-H₂ gas mixture atmosphere [87]. They also proved good long-term reliability and thermal stability of the Cu/Cu joint through an aging test. Yamakawa et al. investigated a low-temperature bonding process utilizing Cu nanoparticle paste without the addition of sintering promoter, obtaining a joint with a shear strength of above 30 MPa even at a temperature of 250 °C [88]. Nishikawa et al. obtained a Cu/Cu joint using Cu nanoparticle paste and investigated the effect of heating conditions on the joint strength of the joint [89]. Kobayashi et al. prepared Cu nanoparticles in an aqueous solution for the MNP bonding, further inducing the cost of manufacturing of Cu nanoparticles [90].

Although Cu nanoparticle is a potential alternative to Ag nanoparticle for die-attach bonding, they are extremely vulnerable to oxidation: native oxide layers could be readily formed and covered on the nanoparticle surfaces, hindering sinter and cause inferior mechanical performance. Therefore, Cu nanoparticles are most sintered in an inert or reductive gas atmosphere; it makes processes not compatible

Table 1.3 Comparison of the three die-attach bonding methods.

Methods	Reliability	Conductivity	Process time	Cost	Serving temperature
Soldering	Fair	Fair	Good	Good	Poor
TLP bonding	Fair	Fair	Poor	Fair	Fair
MNP bonding	Fair	Good	Fair	Poor	Good

with most facilities currently using and require complex steps. The preservation of Cu nanoparticles also raises concern because they tend to lose nanoscale features due to quick agglomeration and oxidation.

1.3 Motion of the research

On the basis of the above discussion, a bonding method including corresponding bonding materials should be evaluated by the following aspects: reliability of joints, thermal and electrical conductivities of joints, whole process time, cost of material manufacturing and processing, and highest serving temperature. A comparison is shown in **Table 1.3**, which summarizes the die attach bonding methods we have discussed above. Currently, the soldering and the TLP bonding methods are widely used for die attaching. The MNP bonding method, despite its relatively high cost, is adopted for severe serving conditions. Especially, the Cu/Cu joint, fabricated through the MNP bonding method, is the most preferred joint for high-current power devices. However, MNPs exhibit many undesirable features, such as spontaneous agglomeration, the tendency of oxidation, and potential pollution [90, 91]. Micro-scale particles (microparticles) exhibit better oxidation resistance, little agglomeration, and few hazards to the environment due to their lower surface energy. Therefore, microparticles are considered as possible candidates for filling materials of the metallic particle bonding method.

1.4 Theoretical basis and scope

1.4.1 Metallic microparticle (MMP) bonding

Just like MNP bonding, the most used microparticles for MMP bonding are Ag, Cu, and their oxide. Nishikawa et al. sintered chestnut-burr-like Ag microparticles, which are believed to have higher surface energy than sphere microparticles, at a temperature of 300 °C and a pressure of 10 MPa for 10 min to obtain a joint with a shear strength of ~30 MPa [92]. Hirose et al. fabricated paste mixing Ag₂O microparticles and triethylene glycol, achieving bonding at 300 °C through a chemical reaction that induced in-situ formation of Ag nanoparticles [93]. Mu et al. mixed Ag₂O microparticles with triethylene glycol to fabricate a paste, which was used to assemble bonding joints at a temperature of 250 °C and a

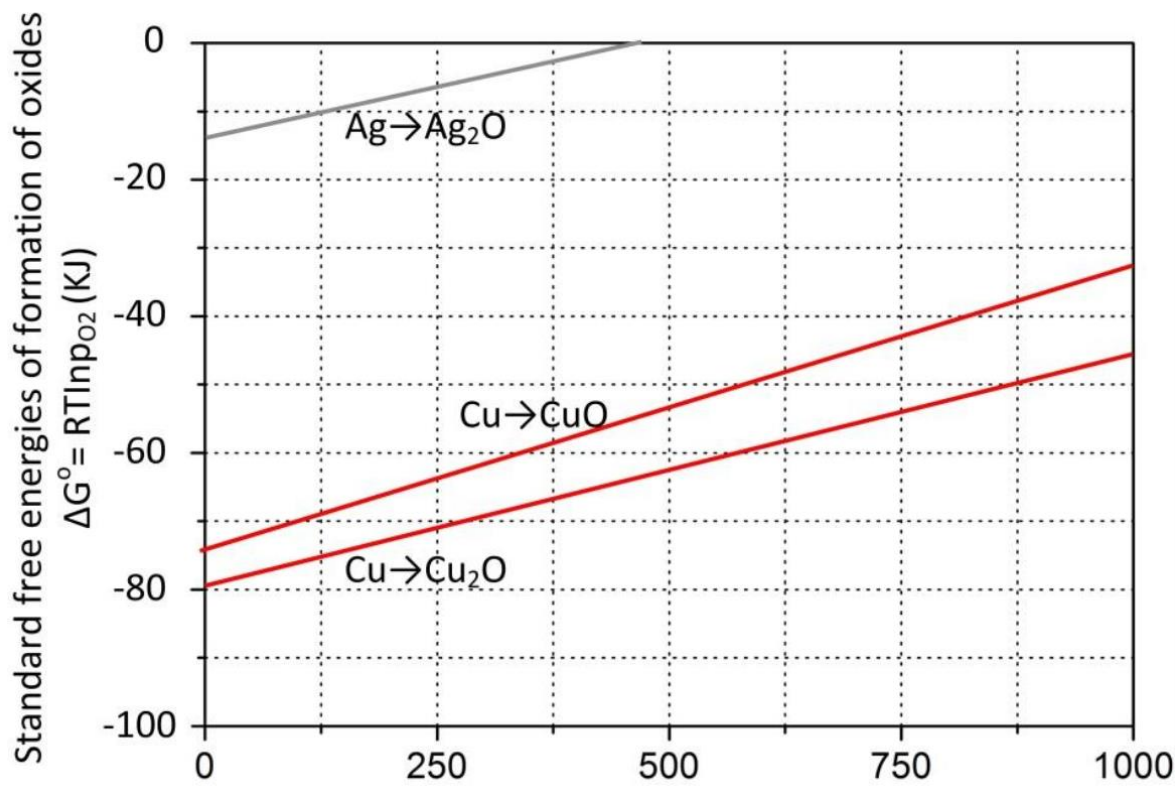


Figure 1.5 Ellingham Diagram for Ag and Cu oxide [97].

pressure of 2 MPa [94]. Cu and Cu oxide also have been extensively researched. Yao et al. mixed CuO and polyethylene glycol 1000 to compose a filler material and assembled a Cu/Cu joint by the redox reaction of CuO [95]. They believe that the redox reaction formed Cu nanoparticles, which play a critical role in the sintering bonding method. Liu et al. developed a reduction-oxidation bonding process, in which Cu microparticles are oxidized first then sintered in a formic-acid atmosphere by reductive reaction [96]. They claimed that in-situ Cu₂O nanoparticles homogeneously formed on Cu microparticles by thermal oxidation, and are subsequently reduced to a Cu nanotexture and sintered in a formic-acid atmosphere, which is a suitable reductive atmosphere for reflow soldering of electronic packaging.

In cases of filling materials for MMP bonding, Cu and Ag differ from oxidation resistance, sinterability, and electromigration resistance. The oxidation resistance for metal can be evaluated by the Gibbs free energy of formation of its oxide: that is, the higher Gibbs energy required for oxide formation, the better oxidation resistance of the metal. As shown in the Ellingham diagram in **Figure 1.5**, the oxidation resistance of Cu inferior to that of Ag; a native Cu₂O layer can form on the surface of Cu at room temperature, while Ag oxidation barely occurs even at 200 °C [97]. The native oxide layers on Cu microparticles will passivate the surface, hindering their sintering by decreasing interdiffusion rate. Therefore, bonding methods of Cu microparticles either use an inert gas (e.g., N₂) to protect Cu microparticles from oxidation or use reductive gas (e.g., H₂) or solvent (polyethylene glycol) to reduce

Cu oxide. In contrast, Ag microparticles can be sintered in an ambient atmosphere, which greatly simplifies the bonding process. Additionally, the sinterability of Cu microparticles is naturally inferior to that of Ag microparticles, because the self-diffusion coefficient of Ag is much higher than that of Cu at same temperatures [98]; this results that Ag microparticles with the same particle size require lower energy (e.g., temperature, pressure) than Cu microparticles do to obtain a joint with target bonding quality. Kim et al. have reported that sintering neck, which is recognized as the initial step of sintering, formed faster in Ag cases comparing to Cu, due to the higher self-diffusion coefficient of Ag [99]. Some researchers have used Ag and Cu microparticles to assemble sintered joints at similar temperatures, pressure, and atmosphere conditions; the shear strength of Ag sintered joints is obviously higher than Cu sintered joints [92, 100]. Finally, as discussed in *Chapter 1.2.3*, poor electromigration resistance of Ag limits its applications, and Cu/Cu joints have been widely used for applications where Ag is not suitable [85, 88, 101-103].

In summary, the Cu/Cu joint exhibits more advantages in high-current power devices due to its excellent electromigration resistance, while its poor sinterability makes the development of the corresponding bonding process highly challenging. Although several researchers have involved chemical treatments and assistant pressures in bonding processes [95, 104, 105], these methods are hardly satisfying because of their long process time and high applied pressure. Therefore, developing a low-temperature die-attach bonding process using Cu microparticles to assemble reliable Cu/Cu joints has been a research hotspot in recent years. In this study, redox reaction and low-power ultrasonic vibration were involved as assisting approaches for Cu microparticle bonding, and their feasibility and theoretical basis were discussed as follows.

1.4.2 Redox reaction assist

Redox reaction assists are most utilized through two mechanisms to promote bonding: the in-situ formation of nanoscale structures and the formation of common second phases at interfaces. The former is achieved by controlling chemical reactions that occur on the material surfaces, forming second-phase nuclei that aggregate into nanoscale structures. The bonding mechanism of the in-situ nanoscale structures can be described taking Liu's ORB bonding process as an example, as shown in **Figure 1.6** [106]. The Cu microparticles are first oxidized by a precisely controlled process to form oxide nanoparticles, which are subsequently reduced to pure Cu nanostructure by a formic acid atmosphere and sintered simultaneously. As for the formation of a common second phase at interfaces, when a second phase

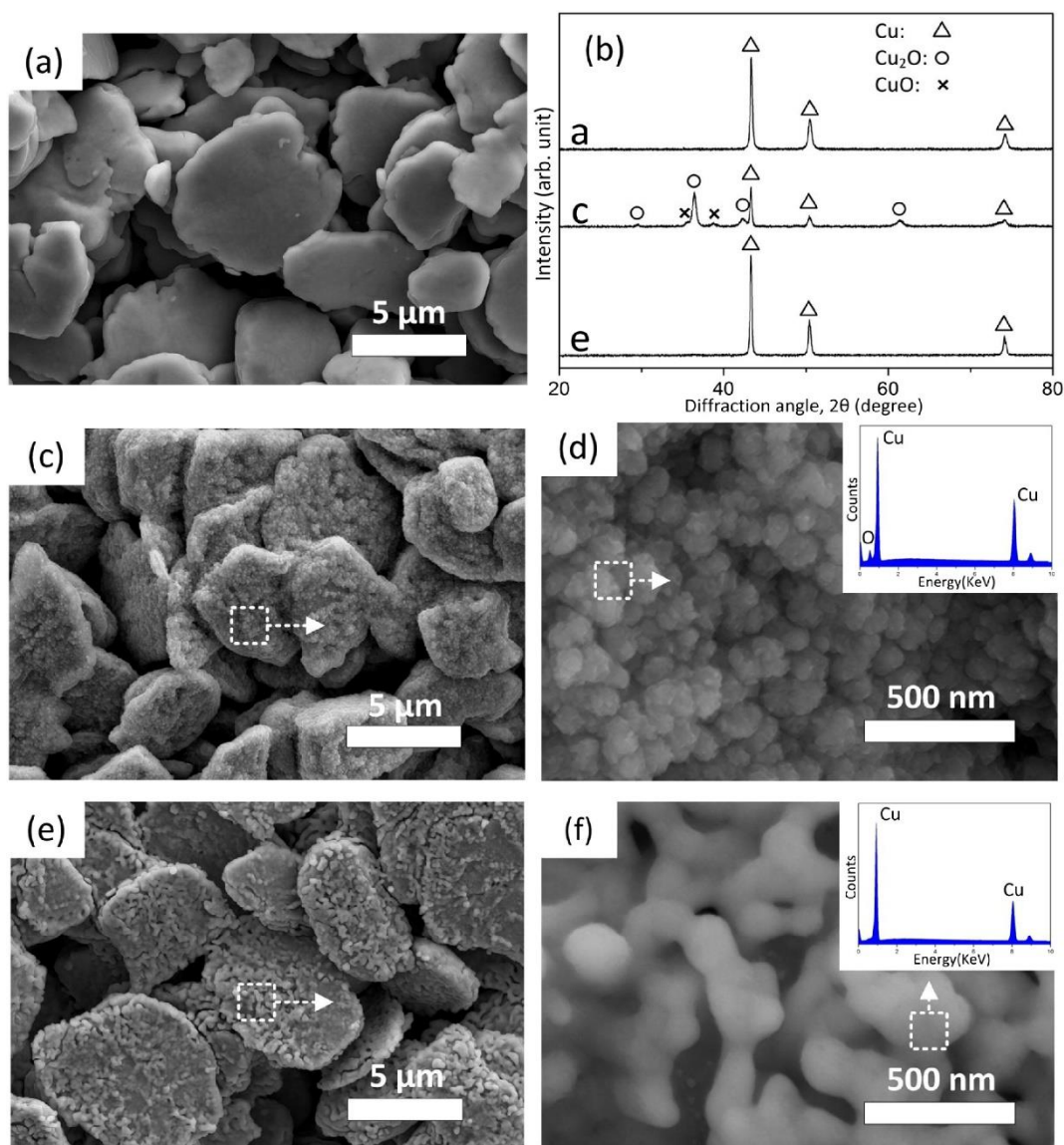


Figure 1.6 A example illustrating formation of in-situ nanoscale structures and their sintering. (a) particles without oxidation, (c, d) in-situ nanoscale structures formed after oxidation, (e, f) sintering of nanoscale structures in formic acid atmosphere, (b) XRD patterns of the particles in (a), (c) and (e) [106].

formed at an interface of two high-energy free surfaces, it will replace the free surfaces with lower-energy grain boundaries, which will be later eliminated with the growth of grains, driven by solid-state interdiffusion. It is a method that requires sufficient diffusion time rather than precise control of reactions. Fundamentally, both the two methods promote the sintering of MMPs by increasing surface energy through chemical treatment, which is pretty feasible.

1.4.3 Ultrasonic vibration assist

Ultrasonic vibration, as an assisting energy source, has been used in soldering processes [107], powder solidification [108], and powder sintering [109]. It has been reported that with ultrasonic vibration, the sintering of pulverized materials dramatically promoted; this is because the highly localized interfacial slip causes localized high temperatures, the disruption and dispersion of surface oxide, breakdown of

asperities and interpenetration of adjacent boundaries, direct metallic contact, and the formation of local lattice bonds [110]. Additionally, high-frequency vibration reduces forming load in forming processes, because it enhances the dislocation motion and reduce the lattice resistance to dislocations, thus, to soften the material and reduce the flowing stress during the forming process, as shown in **Figure 1.7** [111]. This effect is called as the acoustic softening effect. Ji et al. developed a rapid ultrasonic-assisted fluxless soldering method, through which they achieved intermetallic-phase-composed joints using Sn-0.7 Cu solder for high-temperature applications [112]. Zhao et al. applied ultrasonic vibration to Cu/Sn/Cu transient liquid phase bonding and found that the Cu_3Sn phase nucleated randomly and grew unidirectionally within the entire joint [107]. Additionally, ultrasonic vibration has been applied to the fabrication of solder materials. Shu et al. consolidated Sn/In nanosolder particles into nanosolder films using the ultrasonic powder consolidation method [108]. They reported that the nanosolder film, which prevents the nanoparticles from oxidation, is comparable to Sn/In solders. Despite the many applications of ultrasonic vibration in the soldering and fabrication of solder materials, there have been few attempts at utilizing ultrasonic vibration to assist the bonding of metallic microparticles for die-attach.

1.5 Scope of this study

The purpose of this study was to develop bonding methods to assemble reliable high-performance Cu/Cu joints using Cu microparticles for high-temperature applications. Attempts were made to deal with the present challenges in low-temperature sintering of Cu microparticles. Two approaches, including reductive reaction and low-power ultrasonic vibration, were presented to improve the sinterability of Cu microparticles, and the enhancement mechanisms of the two approaches were studied separately. Based on the study of the mechanisms, Cu/Cu joints were successfully assembled by sintering Cu microparticles in the air at a low temperature with the ultrasonic assist.

In chapter 1, the background of WBG semiconductors for high-temperature applications was introduced. Several common die-attach processes for WBG semiconductor packaging and their mechanism were described and compared. Based on the discussion, MMP bonding methods involving low-power ultrasonic vibration and redox reaction for obtaining Cu/Cu joints were proposed.

In chapter 2, we developed a bonding process that sinters preoxidized Cu microparticles in a formic-acid atmosphere at 300 °C to obtain Cu/Cu joints with suitable mechanical performance.

In chapter 3, we investigated the feasibility of a low-power ultrasonic-assisted bonding process with Ag microparticles. Effects of ultrasonic vibration on sintered microstructure, fracture modes of sintered

joints, and enhancement were clarified.

In chapter 4, Cu/Cu joints were successfully assembled by sintering Cu microparticles at a low actual temperature of 200 °C for 15 min, with the double strengthening of low-power ultrasonic vibration and redox reaction. The influence of process parameters such as bonding pressure, reductive agent, and ultrasonic time were investigated, and the bonding mechanism was studied.

In chapter 5, sintered joints fabricated using the methods introduced in Chapter 2 – 4 with their corresponding optimized parameters were isothermally aged at 200 °C. Through the comparison of their microstructure involution, the effects of particle materials, substrates, and bonding methods on the long-term reliability were studied.

In chapter 6, the study was summarized, and the environmental assessments of the proposed methods and corresponding materials were analyzed.

References

1. Baliga, B.J., *Fundamentals of power semiconductor devices*, Springer Science & Business Media, (2010) 1-3.
2. Millán, J., A review of WBG power semiconductor devices, CAS 2012 (International Semiconductor Conference), (2012) 57-66.
3. Millan, J., P. Godignon, X. Perpiñà, A. Pérez-Tomás, and J. Rebollo, A survey of wide bandgap power semiconductor devices. *IEEE transactions on Power Electronics*, **29** (2013) 2155-2163.
4. Oda, O., *Compound semiconductor bulk materials and characterizations*, World Scientific, 2007,
5. Bertulis, K., A. Krotkus, G. Aleksejenko, V. Pačebutas, R. Adomavičius, G. Molis, and S. Marcinkevičius, GaBiAs: A material for optoelectronic terahertz devices. *Applied physics letters*, **88** (2006) 201112.
6. Joyce, H.J., C.J. Docherty, Q. Gao, H.H. Tan, C. Jagadish, J. Lloyd-Hughes, L.M. Herz, and M.B. Johnston, Electronic properties of GaAs, InAs and InP nanowires studied by terahertz spectroscopy. *Nanotechnology*, **24** (2013) 214006.
7. Parkinson, P., J. Lloyd-Hughes, Q. Gao, H.H. Tan, C. Jagadish, M.B. Johnston, and L.M. Herz, Transient terahertz conductivity of GaAs nanowires. *Nano Letters*, **7** (2007) 2162-2165.
8. Buttay, C., D. Planson, B. Allard, D. Bergogne, P. Bevilacqua, C. Joubert, M. Lazar, C. Martin, H. Morel, and D. Tournier, State of the art of high temperature power electronics. *Materials Science and Engineering: B*, **176** (2011) 283-288.
9. Chow, T.P. and R. Tyagi, Wide bandgap compound semiconductors for superior high-voltage unipolar power devices. *IEEE Transactions on Electron Devices*, **41** (1994) 1481-1483.
10. Yoder, M.N., Wide bandgap semiconductor materials and devices. *IEEE Transactions on Electron Devices*, **43** (1996) 1633-1636.
11. Berger, L.I., *Semiconductor materials*, CRC press, (1996) 56-64.
12. Dargys, A. and J. Kundrotas, *Handbook on physical properties of Ge, Si, GaAs and InP*, Science and Encyclopedia Publ., (1994) 31-82; 189-228.
13. Arai, K. and S. Yoshida, Fundamentals and applications of SiC devices [in Japanese]. *Ohmsha, Tokyo*, (2003) 12.
14. Levinshtein, M.E., S.L. Rumyantsev, and M.S. Shur, *Properties of Advanced Semiconductor Materials: GaN, AlN, InN, BN, SiC, SiGe*, John Wiley & Sons, (2001) 1-31.
15. Khanna, V.K., *Insulated gate bipolar transistor IGBT theory and design*, John Wiley & Sons,

- (2004) 1-2.
16. Treu, M., E. Vecino, M. Pippan, O. Häberlen, G. Curatola, G. Deboy, M. Kutschak, and U. Kirchner, The role of silicon, silicon carbide and gallium nitride in power electronics, 2012 International Electron Devices Meeting, (2012) 7.1. 1-7.1. 4.
 17. Choi, J., D. Tsukiyama, Y. Tsuruda, and J.M.R. Davila, High-frequency, high-power resonant inverter with eGaN FET for wireless power transfer. *IEEE Transactions on Power Electronics*, **33** (2017) 1890-1896.
 18. Mitova, R., R. Ghosh, U. Mhaskar, D. Klikic, M.-X. Wang, and A. Dentella, Investigations of 600-V GaN HEMT and GaN diode for power converter applications. *IEEE transactions on power electronics*, **29** (2013) 2441-2452.
 19. Hartnett, A. and S. Buerki, Process and reliability advantages of AuSn eutectic die attach. *Proc. 42nd IMAPS*, (2009) 281-287.
 20. Lalena, J., N. Dean, and M. Weiser, Ge-doped Ag-Bi: A new Pb-free power die attach solder. *Proc. Honeywell Electron. Mater., 131th Annu. TMS Meet. Exhibit*, (2002) 1-18.
 21. Manikam, V.R. and K.Y. Cheong, Die attach materials for high temperature applications: A review. *IEEE Transactions on Components, Packaging and Manufacturing Technology*, **1** (2011) 457-478.
 22. Menon, S., E. George, M. Osterman, and M. Pecht, High lead solder (over 85%) solder in the electronics industry: RoHS exemptions and alternatives. *Journal of Materials Science: Materials in Electronics*, **26** (2015) 4021-4030.
 23. Parliament, E., Directive 2002/95/EC of the European Parliament and of the Council of 27 January 2003 on the restriction of the use of certain hazardous substances in electrical and electronic equipment. *Official Journal of the European Union*, **37** (2003) 19-23.
 24. Yoon, J.-W., H.-S. Chun, and S.-B. Jung, Reliability analysis of Au–Sn flip-chip solder bump fabricated by co-electroplating. *Journal of materials research*, **22** (2007) 1219-1229.
 25. Chin, H.S., K.Y. Cheong, and A.B. Ismail, A review on die attach materials for SiC-based high-temperature power devices. *Metallurgical and Materials Transactions B*, **41** (2010) 824-832.
 26. Chidambaram, V., J. Hald, and J. Hattel, Development of Au–Ge based candidate alloys as an alternative to high-lead content solders. *Journal of alloys and compounds*, **490** (2010) 170-179.
 27. Musa, S.A., M. Salleh, M.A. Anuar, and S. Norainiza, Zn-Sn based high temperature solder-A short review, *Advanced Materials Research*, (2013) 518-521.
 28. Zeng, G., S. McDonald, and K. Nogita, Development of high-temperature solders.

- Microelectronics Reliability*, **52** (2012) 1306-1322.
29. Lee, J.-E., K.-S. Kim, K. Suganuma, M. Inoue, and G. Izuta, Thermal properties and phase stability of Zn-Sn and Zn-In alloys as high temperature lead-free solder. *Materials transactions*, **48** (2007) 584-593.
 30. Mahmudi, R. and M. Eslami, Shear strength of the Zn–Sn high-temperature lead-free solders. *Journal of Materials Science: Materials in Electronics*, **22** (2011) 1168-1172.
 31. Kim, S., K.-S. Kim, S.-S. Kim, and K. Suganuma, Interfacial reaction and die attach properties of Zn-Sn high-temperature solders. *Journal of Electronic Materials*, **38** (2009) 266-272.
 32. Kim, S., K.-S. Kim, S.-S. Kim, K. Suganuma, and G. Izuta, Improving the reliability of Si die attachment with Zn-Sn-based high-temperature Pb-free solder using a TiN diffusion barrier. *Journal of electronic materials*, **38** (2009) 2668.
 33. Shimizu, T., H. Ishikawa, I. Ohnuma, and K. Ishida, Zn-Al-Mg-Ga alloys as Pb-free solder for die-attaching use. *Journal of electronic materials*, **28** (1999) 1172-1175.
 34. Massalski, T.B., Binary alloy phase diagrams. *ASM international*, **3** (1992) 2874.
 35. Song, J.-M., H.-Y. Chuang, and Z.-M. Wu, Interfacial reactions between Bi-Ag high-temperature solders and metallic substrates. *Journal of electronic materials*, **35** (2006) 1041-1049.
 36. Lalena, J.N., N.F. Dean, and M.W. Weiser, Experimental investigation of Ge-doped Bi-11Ag as a new Pb-free solder alloy for power die attachment. *Journal of electronic materials*, **31** (2002) 1244-1249.
 37. Kisiel, R. and Z. Szczepański, Die-attachment solutions for SiC power devices. *Microelectronics reliability*, **49** (2009) 627-629.
 38. Paulonis, D.F., D.S. Duvall, and W.A. Owczarski, *Diffusion bonding utilizing transient liquid phase*. 1972, Google Patents.
 39. Chidambaram, V., J. Hattel, and J. Hald, High-temperature lead-free solder alternatives. *Microelectronic Engineering*, **88** (2011) 981-989.
 40. Tuah-Poku, I., M. Dollar, and T.B. Massalski, A study of the transient liquid phase bonding process applied to a Ag/Cu/Ag sandwich joint. *Metallurgical Transactions A*, **19** (1988) 675-686.
 41. Gale, W. and D. Butts, Transient liquid phase bonding. *Science and technology of welding and joining*, **9** (2004) 283-300.
 42. Greve, H., S.A. Moeini, and F.P. McCluskey, Reliability of paste based transient liquid phase sintered interconnects, 2014 IEEE 64th Electronic Components and Technology Conference

- (ECTC), (2014) 1314-1320.
43. Chu, K., Y. Sohn, and C. Moon, A comparative study of Cu/Sn/Cu and Ni/Sn/Ni solder joints for low temperature stable transient liquid phase bonding. *Scripta Materialia*, **109** (2015) 113-117.
 44. Bosco, N. and F. Zok, Critical interlayer thickness for transient liquid phase bonding in the Cu–Sn system. *Acta Materialia*, **52** (2004) 2965-2972.
 45. Li, J., P. Agyakwa, and C. Johnson, Interfacial reaction in Cu/Sn/Cu system during the transient liquid phase soldering process. *Acta Materialia*, **59** (2011) 1198-1211.
 46. Liu, J., H. Zhao, Z. Li, X. Song, H. Dong, Y. Zhao, and J. Feng, Study on the microstructure and mechanical properties of Cu-Sn intermetallic joints rapidly formed by ultrasonic-assisted transient liquid phase soldering. *Journal of Alloys and Compounds*, **692** (2017) 552-557.
 47. Rajendran, S.H., J. Do Hyun, J. Wook Sang, and J. Jae Pil, Transient Liquid Phase Bonding of Copper Using Sn Coated Cu MWCNT Composite Powders for Power Electronics. *Applied Sciences*, **9** (2019) 529.
 48. Mokhtari, O. and H. Nishikawa, Transient liquid phase bonding of Sn–Bi solder with added Cu particles. *Journal of materials science: materials in electronics*, **27** (2016) 4232-4244.
 49. Liu, X., S. Zhou, and H. Nishikawa, Thermal stability of low-temperature sintered joint using Sn-coated Cu particles during isothermal aging at 250 °C. *Journal of Materials Science: Materials in Electronics*, **28** (2017) 12606-12616.
 50. Abdelfatah, M. and O. Ojo, Formation of eutectic-type microconstituent during transient liquid phase bonding of nickel: influence of process parameters. *Materials Science and Technology*, **25** (2009) 61-67.
 51. Yoon, S.W., M.D. Glover, and K. Shiozaki, Nickel–tin transient liquid phase bonding toward high-temperature operational power electronics in electrified vehicles. *IEEE Transactions on Power Electronics*, **28** (2012) 2448-2456.
 52. Lee, B.-S., S.-K. Hyun, and J.-W. Yoon, Cu–Sn and Ni–Sn transient liquid phase bonding for die-attach technology applications in high-temperature power electronics packaging. *Journal of Materials Science: Materials in Electronics*, **28** (2017) 7827-7833.
 53. Marauska, S., M. Claus, T. Lisec, and B. Wagner, Low temperature transient liquid phase bonding of Au/Sn and Cu/Sn electroplated material systems for MEMS wafer-level packaging. *Microsystem technologies*, **19** (2013) 1119-1130.
 54. Chen, H., T. Hu, M. Li, and Z. Zhao, Cu@ Sn core–shell structure powder preform for high-

- temperature applications based on transient liquid phase bonding. *IEEE Transactions on Power Electronics*, **32** (2016) 441-451.
55. Jung, D., A. Sharma, M. Mayer, and J. Jung, A review on recent advances in transient liquid phase (TLP) bonding for thermoelectric power module. *Reviews on Advanced Materials Science*, **53** (2018) 147-160.
56. Honrao, C., T.-C. Huang, M. Kobayashi, V. Smet, P.M. Raj, and R. Tummala, Accelerated SLID bonding using thin multi-layer copper-solder stack for fine-pitch interconnections, 2014 IEEE 64th Electronic Components and Technology Conference (ECTC), (2014) 1160-1165.
57. Lang, F., H. Yamaguchi, H. Nakagawa, and H. Sato, High temperature resistant joint technology for SiC power devices using transient liquid phase sintering process, 2012 13th International Conference on Electronic Packaging Technology & High Density Packaging, (2012) 157-161.
58. Siow, K.S., *Die-Attach Materials for High Temperature Applications in Microelectronics Packaging*, Springer, (2019) 8-17.
59. Buffat, P. and J.P. Borel, Size effect on the melting temperature of gold particles. *Physical review A*, **13** (1976) 2287.
60. Vitos, L., A. Ruban, H.L. Skriver, and J. Kollar, The surface energy of metals. *Surface science*, **411** (1998) 186-202.
61. Kim, T., M. Howlader, T. Itoh, and T. Suga, Room temperature Cu–Cu direct bonding using surface activated bonding method. *Journal of Vacuum Science & Technology A: Vacuum, Surfaces, and Films*, **21** (2003) 449-453.
62. Kang, S.-J.L., *Sintering: densification, grain growth and microstructure*, Elsevier, (2004) 40-75.
63. Coble, R. and T. Gupta, *Intermediate stage sintering*, in *Sintering and related phenomena*, Gordon and Breach. (1967) 423-444.
64. Coble, R.L., Sintering crystalline solids. I. Intermediate and final state diffusion models. *Journal of applied physics*, **32** (1961) 787-792.
65. Yoon, K.J. and S.-J.L. Kang, Densification of ceramics containing entrapped gases during pressure sintering. *Journal of the European Ceramic Society*, **6** (1990) 201-202.
66. Wu, Z., J. Cai, J. Wang, Z. Geng, and Q. Wang, Low-Temperature Cu-Cu Bonding Using Silver Nanoparticles Fabricated by Physical Vapor Deposition. *Journal of Electronic Materials*, **47** (2018) 988-993.
67. Ishizaki, T., A. Kuno, A. Tane, M. Yanase, F. Osawa, T. Satoh, and Y. Yamada, Reliability of Cu

- nanoparticle joint for high temperature power electronics. *Microelectronics Reliability*, **54** (2014) 1867-1871.
68. Dastjerdi, R. and M. Montazer, A review on the application of inorganic nano-structured materials in the modification of textiles: focus on anti-microbial properties. *Colloids and Surfaces B: Biointerfaces*, **79** (2010) 5-18.
69. Magdassi, S., M. Grouchko, and A. Kamyshny, Copper nanoparticles for printed electronics: routes towards achieving oxidation stability. *Materials*, **3** (2010) 4626-4638.
70. Luechinger, N.A., E.K. Athanassiou, and W.J. Stark, Graphene-stabilized copper nanoparticles as an air-stable substitute for silver and gold in low-cost ink-jet printable electronics. *Nanotechnology*, **19** (2008) 445201.
71. Yan, J., G. Zou, A.-p. Wu, J. Ren, J. Yan, A. Hu, and Y. Zhou, Pressureless bonding process using Ag nanoparticle paste for flexible electronics packaging. *Scripta Materialia*, **66** (2012) 582-585.
72. Jianfeng, Y., Z. Guisheng, H. Anming, and Y.N. Zhou, Preparation of PVP coated Cu NPs and the application for low-temperature bonding. *Journal of Materials Chemistry*, **21** (2011) 15981-15986.
73. Schwarzbauer, H., *Method of securing electronic components to a substrate*. 1989, Google Patents.
74. Schwarzbauer, H., *Method and apparatus for fastening electronic components to substrates*. 1990, Google Patents.
75. Alarifi, H., A. Hu, M. Yavuz, and Y.N. Zhou, Silver nanoparticle paste for low-temperature bonding of copper. *Journal of Electronic Materials*, **40** (2011) 1394-1402.
76. Wang, S., H. Ji, M. Li, and C. Wang, Fabrication of interconnects using pressureless low temperature sintered Ag nanoparticles. *Materials Letters*, **85** (2012) 61-63.
77. Wang, S., M. Li, H. Ji, and C. Wang, Rapid pressureless low-temperature sintering of Ag nanoparticles for high-power density electronic packaging. *Scripta Materialia*, **69** (2013) 789-792.
78. Yan, J., D. Zhang, G. Zou, L. Liu, H. Bai, A. Wu, and Y.N. Zhou, Sintering bonding process with Ag nanoparticle paste and joint properties in high temperature environment. *Journal of Nanomaterials*, **2016** (2016) 5284048.
79. Chua, S. and K.S. Siow, Microstructural studies and bonding strength of pressureless sintered nano-silver joints on silver, direct bond copper (DBC) and copper substrates aged at 300 C. *Journal of Alloys and Compounds*, **687** (2016) 486-498.
80. Morisada, Y., T. Nagaoka, M. Fukusumi, Y. Kashiwagi, M. Yamamoto, and M. Nakamoto, A low-temperature bonding process using mixed Cu–Ag nanoparticles. *Journal of electronic materials*,

39 (2010) 1283-1288.

81. Huntington, H., *Diffusion in Solids: Recent Developments, 1st edition. AS Nowick and JJ Burton*, New York: Academic Press, (1975) 303-352.
82. Chen, C.-M. and S.-W. Chen, Electromigration effect upon the Sn/Ag and Sn/Ni interfacial reactions at various temperatures. *Acta materialia*, **50** (2002) 2461-2469.
83. Morris, J., C.-U. Kim, and S. Kang, The metallurgical control of electromigration failure in narrow conducting lines. *JOM*, **48** (1996) 43-46.
84. Hummel, R., Electromigration and related failure mechanisms in integrated circuit interconnects. *International materials reviews*, **39** (1994) 97-112.
85. Zinn, A., R. Stoltenberg, A. Fried, J. Chang, A. Elhawary, J. Beddow, and F. Chiu, nanoCopper based solder-free electronic assembly material. *Nanotech*, **2** (2012) 71-74.
86. Schnabl, K., L. Wentlent, K. Mootoo, S. Khasawneh, A. Zinn, J. Beddow, E. Hauptfleisch, D. Blass, and P. Borgesen, Nanocopper Based Solder-Free Electronic Assembly. *Journal of Electronic Materials*, **43** (2014) 4515-4521.
87. Li, J., X. Yu, T. Shi, C. Cheng, J. Fan, S. Cheng, G. Liao, and Z. Tang, Low-temperature and low-pressure Cu-Cu bonding by highly sinterable Cu nanoparticle paste. *Nanoscale research letters*, **12** (2017) 1-6.
88. Yamakawa, T., T. Takemoto, M. Shimoda, H. Nishikawa, K. Shiokawa, and N. Terada, Influence of joining conditions on bonding strength of joints: efficacy of low-temperature bonding using Cu nanoparticle paste. *Journal of electronic materials*, **42** (2013) 1260-1267.
89. Nishikawa, H., T. Hirano, and T. Takemoto, Bonding process of Cu/Cu joint using Cu nanoparticle paste. *Transactions of JWRI*, **40** (2011) 33-36.
90. Kobayashi, Y., T. Shirochi, Y. Yasuda, and T. Morita, Metal-metal bonding process using metallic copper nanoparticles prepared in aqueous solution. *International journal of adhesion and adhesives*, **33** (2012) 50-55.
91. Taghavi, S.M., M. Momenpour, M. Azarian, M. Ahmadian, F. Souri, S.A. Taghavi, M. Sadeghain, and M. Karchani, Effects of nanoparticles on the environment and outdoor workplaces. *Electronic physician*, **5** (2013) 706.
92. Nishikawa, H., X. Liu, X. Wang, A. Fujita, N. Kamada, and M. Saito, Microscale Ag particle paste for sintered joints in high-power devices. *Materials Letters*, **161** (2015) 231-233.
93. Hirose, A., H. Tatsumi, N. Takeda, Y. Akada, T. Ogura, E. Ide, and T. Morita, A novel metal-to-

- metal bonding process through in-situ formation of Ag nanoparticles using Ag₂O microparticles. *Journal of Physics: Conference Series*, **165** (2009) 012074.
94. Mu, F., Z. Zhao, G. Zou, H. Bai, A. Wu, L. Liu, D. Zhang, and Y.N. Zhou, Mechanism of low temperature sintering-bonding through in-situ formation of silver nanoparticles using silver oxide microparticles. *Materials transactions*, **54** (2013) 872-878.
95. Yao, T., T. Matsuda, T. Sano, C. Morikawa, A. Ohbuchi, H. Yashiro, and A. Hirose, In Situ Study of Reduction Process of CuO Paste and Its Effect on Bondability of Cu-to-Cu Joints. *Journal of Electronic Materials*, **47** (2018) 2193-2197.
96. Liu, X. and H. Nishikawa, Low-pressure Cu-Cu bonding using in-situ surface-modified microscale Cu particles for power device packaging. *Scripta Materialia*, **120** (2016) 80-84.
97. Howard, S., Ellingham diagrams: standard Gibbs energies of formation for oxides. *SD School of Mines and Technology, Rapid City, SD*, (2006), 25-31.
98. Hough, R., An investigation of the surface self-diffusion coefficients of pure copper and silver by the grain boundary grooving technique. *Scripta Metallurgica*, **4** (1970) 559-561.
99. Kim, S.J., E.A. Stach, and C.A. Handwerker, Fabrication of conductive interconnects by Ag migration in Cu–Ag core-shell nanoparticles. *Applied Physics Letters*, **96** (2010) 144101.
100. Liu, X. and H. Nishikawa, Pressureless sintering bonding using hybrid microscale Cu particle paste on ENIG, pure Cu and pre-oxidized Cu substrate by an oxidation–reduction process. *Journal of Materials Science: Materials in Electronics*, **28** (2017) 5554-5561.
101. Nishikawa, H., T. Hirano, T. Takemoto, and N. Terada, Effects of joining conditions on joint strength of Cu/Cu joint using Cu nanoparticle paste. *Open Surface Science Journal*, **3** (2011) 60-64.
102. Li, J., X. Yu, T. Shi, C. Cheng, J. Fan, S. Cheng, G. Liao, and Z. Tang, Low-Temperature and Low-Pressure Cu–Cu Bonding by Highly Sinterable Cu Nanoparticle Paste. *Nanoscale research letters*, **12** (2017) 255.
103. Dai, Y., M. Ng, P. Anantha, Y. Lin, Z. Li, C.L. Gan, and C.S. Tan, Enhanced copper micro/nano-particle mixed paste sintered at low temperature for 3D interconnects. *Applied Physics Letters*, **108** (2016) 263103.
104. Fujimoto, T., T. Ogura, T. Sano, and A. Hirose, Joining of pure copper using Cu nanoparticles derived from CuO paste, Pan Pacific Microelectronics Symposium (Pan Pacific), (2016) 1-6.
105. Liu, X. and H. Nishikawa, Pressureless sintering bonding using hybrid microscale Cu particle

- paste on ENIG, pure Cu and pre-oxidized Cu substrate by an oxidation–reduction process. *Journal of Materials Science: Materials in Electronics*, **28** (2016) 5554-5561.
106. Xiangdong, L., Novel bonding process using surface-modified microscale Cu particles for high-temperature electronic packaging. (2017), 118-119.
107. Zhao, H., J. Liu, Z. Li, Y. Zhao, H. Niu, X. Song, and H. Dong, Non-interfacial growth of Cu₃Sn in Cu/Sn/Cu joints during ultrasonic-assisted transient liquid phase soldering process. *Materials Letters*, **186** (2017) 283-288.
108. Shu, Y., S. Gheybi Hashemabad, T. Ando, and Z. Gu, Ultrasonic powder consolidation of Sn/In nanosolder particles and their application to low temperature Cu-Cu joining. *Materials & Design*, **111** (2016) 631-639.
109. Zhao, X., S. Zhao, and Q. Han, Effects of vibration direction on the mechanical behavior and microstructure of a metal sheet undergoing vibration-assisted uniaxial tension. *Materials Science and Engineering: A*, **743** (2019) 472-481.
110. Doumanidis, C.C., Nanomanufacturing of random branching material architectures. *Microelectronic Engineering*, **86** (2009) 467-478.
111. Hu, J., T. Shimizu, T. Yoshino, T. Shiratori, and M. Yang, Evolution of acoustic softening effect on ultrasonic-assisted micro/meso-compression behavior and microstructure. *Ultrasonics*, (2020) 106107.
112. Ji, H., Y. Qiao, and M. Li, Rapid formation of intermetallic joints through ultrasonic-assisted die bonding with Sn–0.7Cu solder for high temperature packaging application. *Scripta Materialia*, **110** (2016) 19-23.

Chapter 2

Bonding process using preoxidized Cu microparticles under formic acid atmosphere

2.1 Introduction

Formic acid is now widely researched in soldering processes as a reductive atmosphere [1-4], and it was also reported to promote the sintering of Cu nanoparticles [5]. When it adsorbs on the surface of Cu oxide, it dissociates into formate anion and H^+ at temperatures above 177 °C [6], which are reactants for Cu oxide to form pure Cu. In this chapter, we developed a bonding process sintering preoxidized Cu microparticles in a formic acid atmosphere. We first discuss the transformation of Cu microparticles during preoxidation and then analyze the reduction of the preoxidized Cu microparticles by formic acid. Based on these observations, the effects of each treatment on the microstructures and performance of the Cu/Cu joints are analyzed along with the bonding mechanism.

2.2 Experimental

2.2.1 Sample fabrication

Spherical Cu microparticles with an average diameter of $4.2\ \mu\text{m}$ (1400YM, Mitsui Mining & Smelting Co., Ltd.) were used as parent microparticles, as shown in **Figure 2.1**. α -Terpineol was used as the solvent to make the paste, which does not react with other ingredients in the paste and will quickly evaporate at temperatures over $210\ ^\circ\text{C}$. Then, the Cu microparticles were first preoxidized in an oven (FH-360, Toyo Seisakusho Kasha, Ltd.) at $280\ ^\circ\text{C}$ (setting temperature) for preoxidation, and then were ground to separate the microparticles. Subsequently, pastes were prepared by mixing preoxidized Cu with terpineol

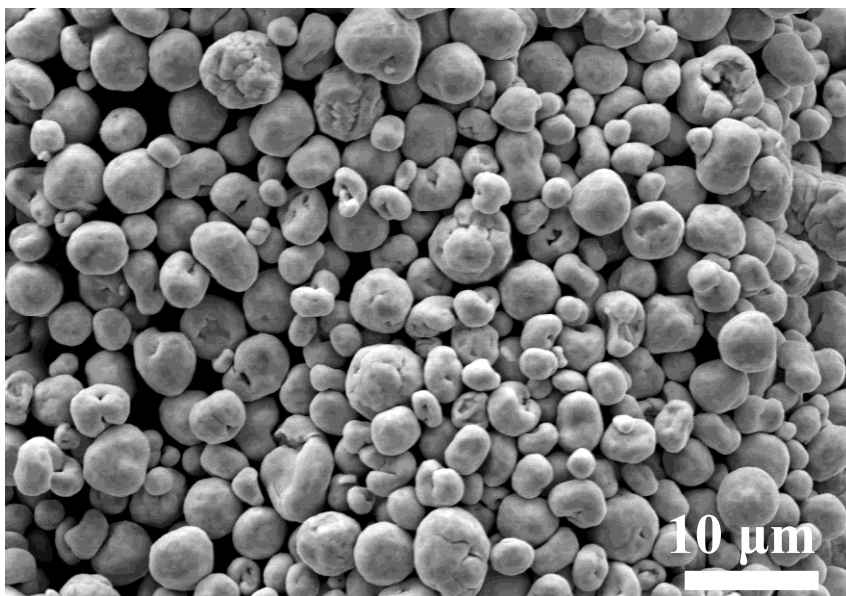


Figure 2.1 The Cu parent microparticles used in this study.

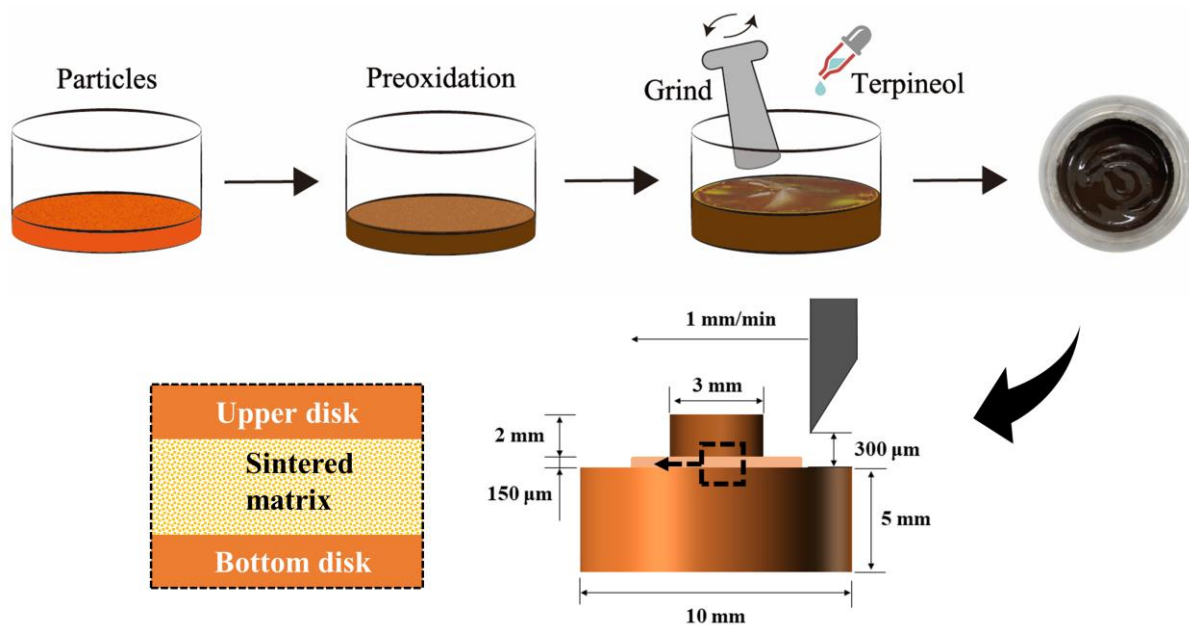


Figure 2.2 Illustration of paste and bonding specimen fabrication.

in the 85/15 wt.%/wt.% ratio. Two types of oxygen-free Cu cylindrical disks were used to fabricate the bonding joints; their dimensions and the paste-fabrication process are illustrated in **Figure 2.2**.

The Cu disks were first cleaned ultrasonically in dilute hydrochloric acid (4%) and rinsed with ethanol; latter, a 150 μm -thick paste layer was stencil-printed on the surface of the bottom disk. Finally, the upper disk was mounted on the as-printed paste to obtain a bonding specimen. A large-area bonding machine (RB-100D, Ayumi Industry Co., Ltd) was used for the bonding process. The bonding temperature should be decided according to the dissociation temperature of formic acid [6] and the reaction temperature of formic acid and Cu oxide [3]. It is reported that the reaction between Cu oxide and formic acid is activated at temperatures above 200 $^{\circ}\text{C}$ and is accelerated with increasing temperature [7]. Based

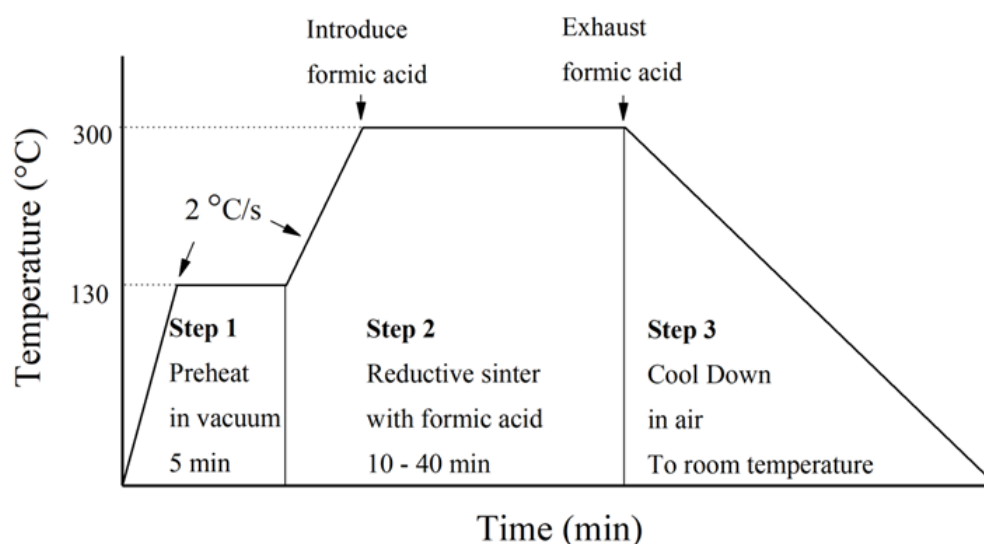


Figure 2.3 The heating profile of the bonding process.

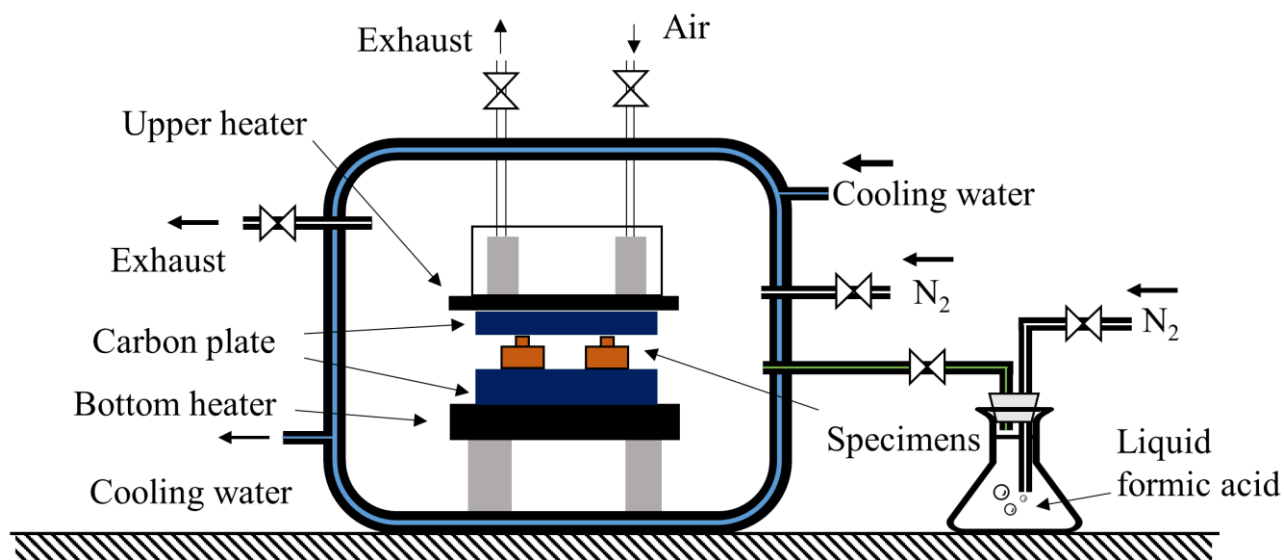


Figure 2.4 Schematic diagram of the bonding machine.

on other bonding processes using formic acid atmosphere [8, 9], peak bonding temperature was determined to be 300 °C. The specimens were preheated at 130 °C in vacuum and then heated to the 300 °C and maintained there for different duration (10 - 40 min) in a formic acid atmosphere (the temperature profile is shown in **Figure 2.3**). When the heater reached the peak temperature, formic acid was introduced into the chamber by passing dry N₂ through the formic acid solution, which results in an atmosphere constituting of ~97% N₂ and 3% formic acid. The bonding machine, as illustrated in **Figure 2.4**, heated the specimens from the top and bottom in an airtight chamber. With a carbon plate placing on, the specimens are actually under a pressure during the process. The actual pressure on each specimen can be calculated by $P = \frac{W}{nA}$, where W is the weight of the upper carbon plate (226 g), n is the number of specimens (3 in this study), A is the bottom area of the upper disk (7.056 mm²). In this study, the actual pressure on each specimen was measured and calculated to be ~0.1 MPa (0.07 N), which may be considered as negligible.

2.2.2 Characterization

The mechanical performance of the bonding was evaluated in terms of shear strength on a shear tester (STR-1000, Rhesca) with a head speed of 1 mm/min; the fly height was set at 200 μm from the surface of the bottom Cu disk, as shown in **Figure 2.1**. Three specimens were tested in each bonding condition, and their average shear strength was determined. The microstructures of fracture surfaces and their cross-sections were characterized by field emission scanning electron microscopy (FESEM; SU-70, Hitachi) and an electron probe microanalyzer (EPMA; JXA-8530F, JEOL) equipped with SEM. As Cu readily deforms during mechanical polishing, which makes it difficult to evaluate the density of the sintered matrix, a cross-section polisher (SM-09010, JEOL) was used to fabricate cross-sectional samples. The crystal structures of the specimens were identified by X-ray diffractometry (XRD; Ultima IV, Rigaku) using Cu-Kα radiation ($\lambda = 1.5405 \text{ \AA}$).

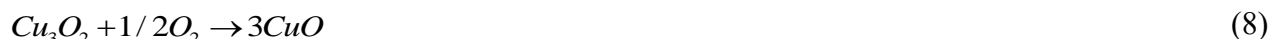
2.3 Result and discussion

2.3.1 Transformation of the Cu microparticles during preoxidation process

As mentioned, the Cu microparticles are supposed to be preoxidized at a certain temperature determined by their thermal properties. The weight loss (TG) and differential thermal analysis (DTA) curves of the Cu microparticles in the air were measured by a simultaneous thermogravimetric analyzer (STA7200, Hitachi) with a temperature rate of 20 °C /min, and results are shown in **Figure 2.5 a**. An

endothermic peak appears with an obvious increase at 257 °C; then another exothermic peak appears at ~350 °C accompanied with the weight starting to increase rapidly from this temperature. The weight finally increased to 109 wt.% by the end of the test.

Obviously, the exothermic peaks and weight increase are contributed to oxidation of the Cu microparticles. Eight reactions are involved in the formation and decomposition of Cu oxide [10]:



It is noted that Cu_3O_2 , a mid product, is the metastable defect structure of Cu_2O and will transform to CuO and Cu_2O at temperatures above 250 °C (Eq.(7) and Eq.(8)) [10, 11]. Therefore, in this study, the existence of Cu_3O_2 is ignored, and Cu_2O and CuO are considered to be the main products of Cu oxidation at temperatures above 250 °C. Based on that, the first exothermic peak at 250 °C indicates the initial oxidation as expressed in Eq.(1). With continuously increasing in the temperature, the oxidation was accelerated, attributing severer oxidation of Cu (Eq.(2)) and further oxidation of Cu_2O (Eq. (4)) occurs at

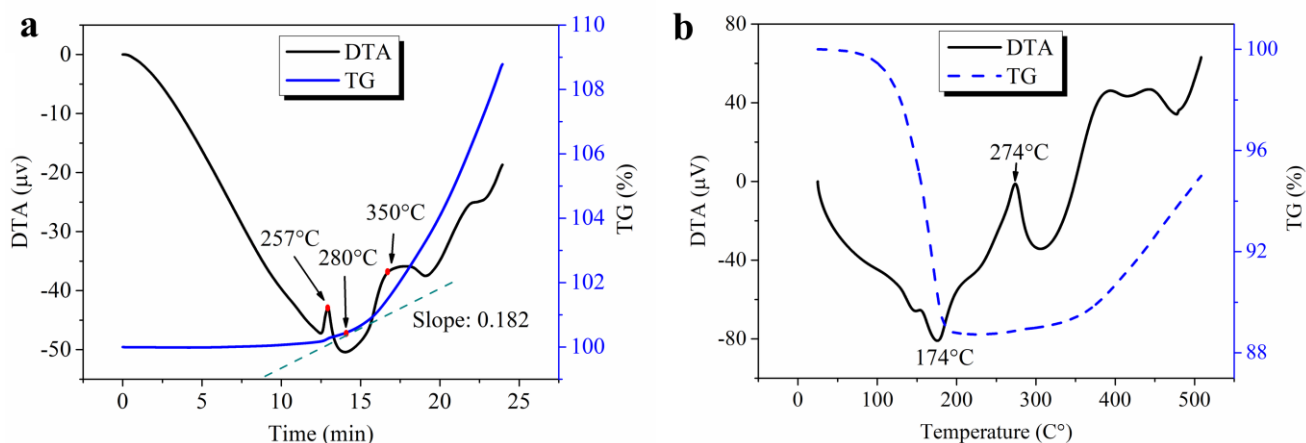


Figure 2.5 TG and DTA curves of the (a) Cu microparticles and (b) as-fabricated paste mixed preoxidized Cu microparticles with 15 wt.% terpeneol.

350 °C, hence the second exothermic peak. To generate uniform Cu₂O as quickly as possible and avoid the formation of unstable CuO, we set the preoxidation temperature at 280 °C. At this temperature, the slope of the TG curve is 0.182 %/min, calculated by the software OriginPro 9.1 based on **Figure 2.5 a**. Assuming that the main product of the preoxidation process is CuO_n, its generation rate R can be simply calculated by $R = \frac{km}{nM_o}$, where n is the number of oxide atoms per metal molecule, M_o is the molecular mass of oxygen, k is the slope of the TG curve at a certain temperature, m is the original mass of the metal in the test. In this study, m was measured to be 13.76 g, n and M_o is considered to be 0.5 and 16 g/mol, respectively; the initial generation rate of Cu₂O at 280 °C is calculated as 3.1×10^{-3} mol/min.

As mentioned, the preoxidized Cu microparticles were mechanical ground with terpineol to fabricate the paste, and the thermal property of the paste is also worth investigation. The Cu microparticles that have been preoxidized at 280 °C for 30 min were made into a paste, which was chosen to be a thermal test specimen. The DTA and TG curves of the as-fabricated paste are shown in **Figure 2.2 b**. An endothermic peak appeared with an obvious weight loss until the weight decreased to 88%. After that, an exothermic peak appeared at ~274 °C with an increase in the weight, and the weight increased back to ~95% when the test ended at 500 °C. The first endothermic peak suggested the evaporation of the terpineol solvent. After its complete evaporation, the preoxidized microparticles started to be further oxidized under high temperatures. Due to the protection of the terpineol, the reoxidation temperature of the paste is slightly higher than the oxidation temperature of dry Cu microparticles.

The surface microstructures of Cu microparticles subjected to preoxidation for different duration at 300 °C are shown in **Figure 2.6**. Cu microparticles without any treatment exhibit a smooth surface as shown in **Figure 2.6 a** and **b**. After preoxidation for 10 min, a rough surface with a corrugation morphology formed, as shown in **Figure 2.6 c** and **d**. After preoxidation for 20 min, the corrugation morphology converted into scallop-like morphologies, which were mainly composed of nanoparticles with an average diameter of ~100 nm, as shown in **Figure 2.6 e** and **f**. After 30 min, whiskers could be observed on the surface, and the nanoparticles were retained, as shown in **Figure 2.6 g** and **h**. With further preoxidation to 40 min, the nanoparticle feature finally coalesced into a layer, as shown in **Figure 2.6 i** and **j**.

The transformation was contributed to the formation of Cu oxide, as suggested by the XRD results shown in **Figure 2.7**. Although both Cu₂O and CuO are believed to form at 280 °C, it is difficult to

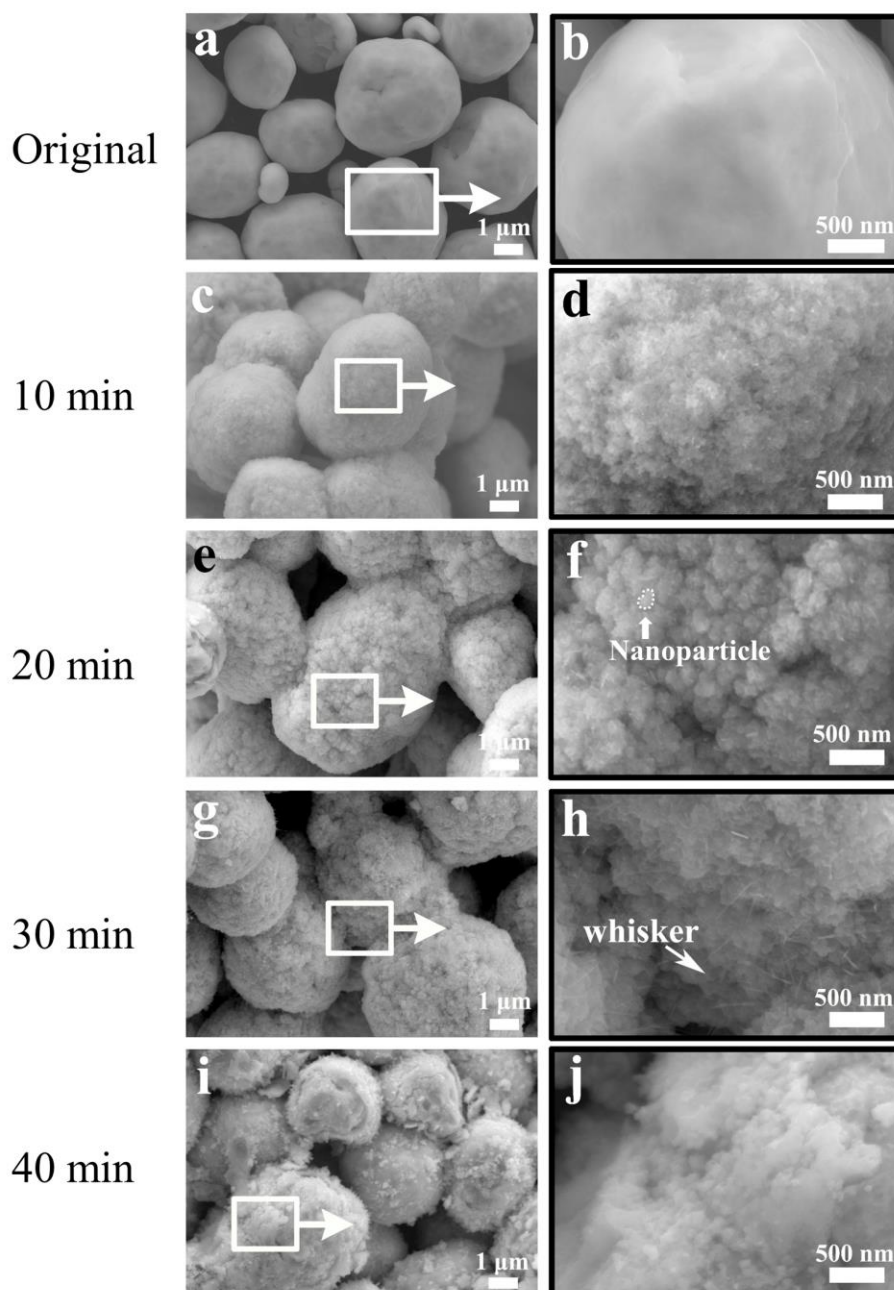


Figure 2.6 Microstructural changes in Cu microparticles preoxidized at 280 °C for : (a, b) 0 min, (c, d) 10 min, (e, f) 20 min, (g, h) 30 min, and (i, j) 40 min.

conclude when CuO formed by only observing the XRD pattern, because (111), (200) and (220) peak of CuO are very close to the diffraction peaks of Cu₂O due to their highly similar crystal structures. For ease of expression, Cu₂O was chosen as the representative oxide in this study, because CuO is a metastable state of Cu oxide and the presence of stable Cu₂O was certain according to its unique peaks in (110) and (200) appearing in the XRD results. The Cu₂O in (111) and (220) direction first formed after preoxidation for 10 min, then the Cu₂O in (200) and (110) direction formed with increasing intensity of oxide after preoxidation for 20 and 40 min, respectively. That is, during the preoxidation, the Cu oxide nucleus in different orientations continuously formed, hence the nanoparticle morphologies. With further

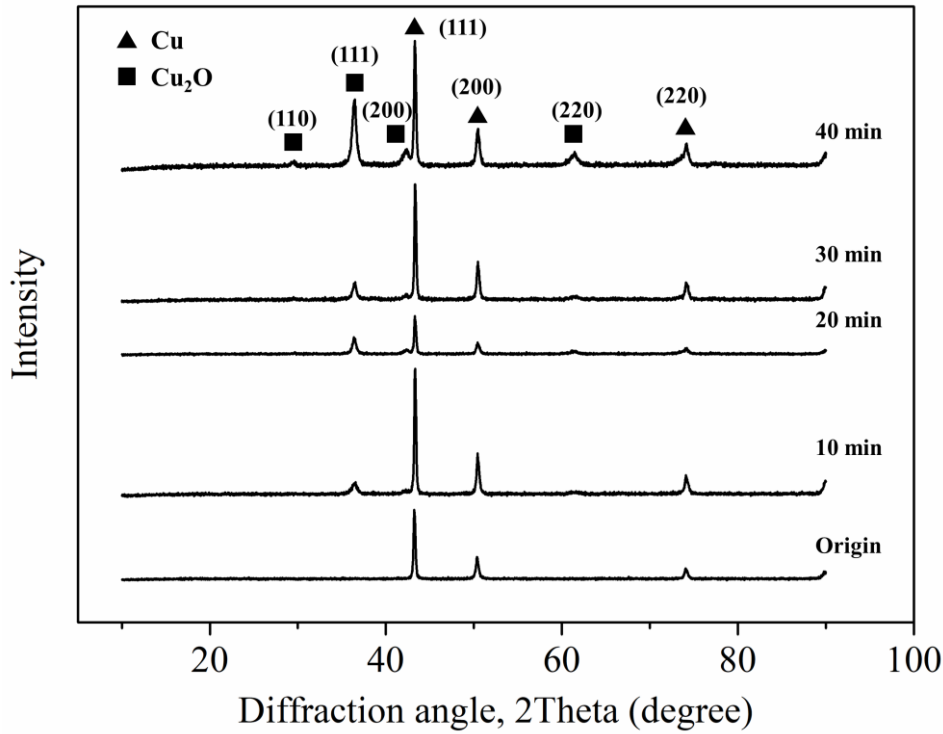


Figure 2.7 XRD pattern of Cu microparticles preoxidized at 280 °C for different periods.

preoxidation, the growth of the formed nuclear coalesced into the oxide layer without nanoscale features.

To investigate the growth of the oxide, the thickness of oxide layers covered on Cu microparticles was measured from cross-section SEM images by the commercial software Image-Pro Plus. Each average thickness was determined by fifteen measurements from five microparticles. The relationship between the average thickness of the oxide layer and the preoxidation time is shown in **Figure 2.8**. Oxide layers with an average thickness of $\sim 0.34 \mu\text{m}$ formed on Cu microparticles after preoxidation for 10 min. Oxide layers thickened only slightly when the preoxidation time was increased, reaching $\sim 0.46 \mu\text{m}$ after 40 min. Worth noting is that, as shown in the cross-sectional SEM images of oxidized microparticles, the morphologies of the microparticles did not vary significantly even when the preoxidation time increased. The thickening can be explained using the Pilling-Bedworth ratio (P-B ratio, R_{PB}) which is defined as the ratio of the volume of metal oxide to that of the corresponding metal; it can also be used to estimate whether a metal can generate a protective oxide barrier [12]. R_{PB} for an alloy can be calculated as follows [13]:

$$R_{PB} = \frac{M_{oxide} \rho_{metal}}{n M_{metal} \rho_{oxide}} \quad (9)$$

where M represents molecular mass, n is the number of metal atoms per oxide molecule, and ρ represents density. It is generally accepted that an oxide coating is passivating and can prevent the metal

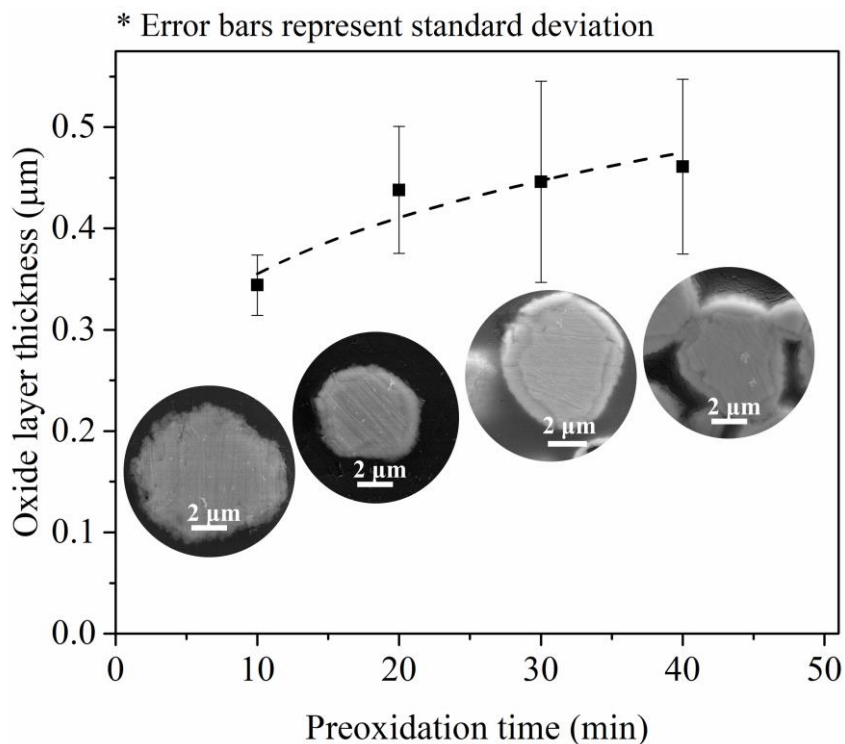


Figure 2.8 The average thickness of oxide layers on Cu microparticles preoxidized at 280°C for different time.

from further oxidation when $1 < R_{PB} < 2$. In the current system, the R_{PB} of CuO and Cu₂O were calculated to be 1.80 and 1.68, respectively. Additionally, the oxidation rate of Cu at 300 °C follows a generalized power law, as shown in Eq. (14) [14]:

$$x^n = kt \quad (10)$$

Where x is the thickness of the oxide layer, t indicates oxidation time, k and n are constants depending on materials and temperatures. It suggests that increasing the preoxidation time affects the surface morphology of the oxide but result in a minimal thickening in the oxide layer after a certain value.

On the basis of this discussion, the transformation of the Cu microparticles during preoxidation at 280 °C can be theorized according to the following reaction mechanism, as shown in **Figure 2.9**. Initially, the Cu microparticles were exposed to the ambient condition, and hence, numerous Cu₂O nucleate appeared on their surfaces as precursor oxide; this formation was dominated by fast reaction-controlled diffusion. Later, these Cu₂O islands gradually coated the Cu microparticle, and the diffusion pattern

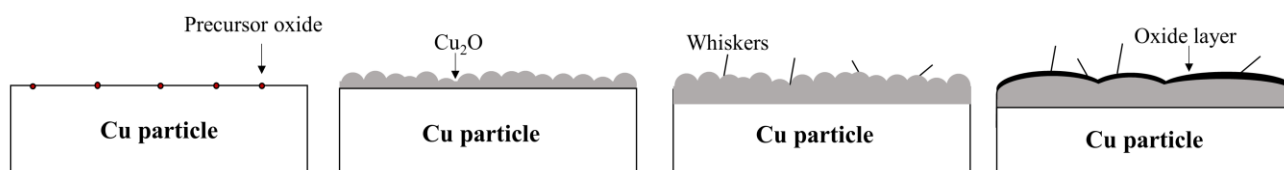
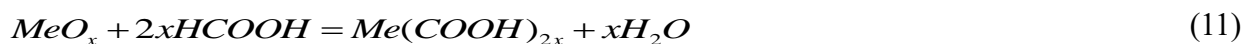


Figure 2.9 Schematic diagram of transformation on Cu microparticle surfaces.

converted to boundary-diffusion. Because Cu expands during oxidation (P-B ratios > 1), a strain concentration occurred in the oxide and at the Cu/Cu oxide interface. Consequently, the oxide built up to form a scallop-like morphology due to mutual extrusion. Later, the strain concentration at the interface promoted the diffusion of inner Cu atoms, resulting in the growth of Cu oxide whiskers [15]. As preoxidation continued, the oxide nanoparticles coarsened and coalesced until the nanoscale features disappeared. As a result, oxide layers coated the microparticle, preventing further internal oxidation.

2.3.2 Transformation of the preoxidized Cu microparticles in formic acid atmosphere

Because preoxidized Cu microparticles were fabricated into pastes and reduced by formic acid in our experimental protocol, their behavior during the reduction reaction is worth investigating. It has been reported that formic acid adsorbs on the surface of Cu oxide and dissociates into a formate anion and H⁺ at temperatures higher than 177 °C [6]. The formate anion undergoes further reaction with Cu oxide [3, 16, 17]; the reaction between metal oxide and formic acid at 300 °C can be expressed as follows [3]:



where *Me* represents metal. Additionally, formic acid is reported to adsorb on Cu surfaces to produce formate by deprotonation and evolution of H₂ [18]. Based on this discussion, the transformation of preoxidized Cu microparticles by formic-acid reduction can be described in **Figure 2.10**. Formic acid first adsorbs on the Cu oxide surfaces and then dissociates into a formate anion and H⁺. They react with Cu oxide to form a continuous Cu formate layer, which later decomposes to Cu. Because the P-B ratios of Cu₂O are greater than 1, volume shrinkage occurs when Cu oxide transforms to Cu, leaving loose outer structures. Therefore, formic acid is capable for penetrating the inner oxide and gradually reducing the entire Cu oxide to Cu. As mentioned, when the Cu oxide was generated, high shear stress existed at oxide/metal interfaces due to the volume expansion occurring during Cu oxidation; Therefore, the volume shrink during CuO reduction induced opposite shear stress. Consequently, the loose outer structures readily separated from the solid parent microparticles and eventually become reduced films covering the outside (**Figure 2.10 d**, color-filled by green).

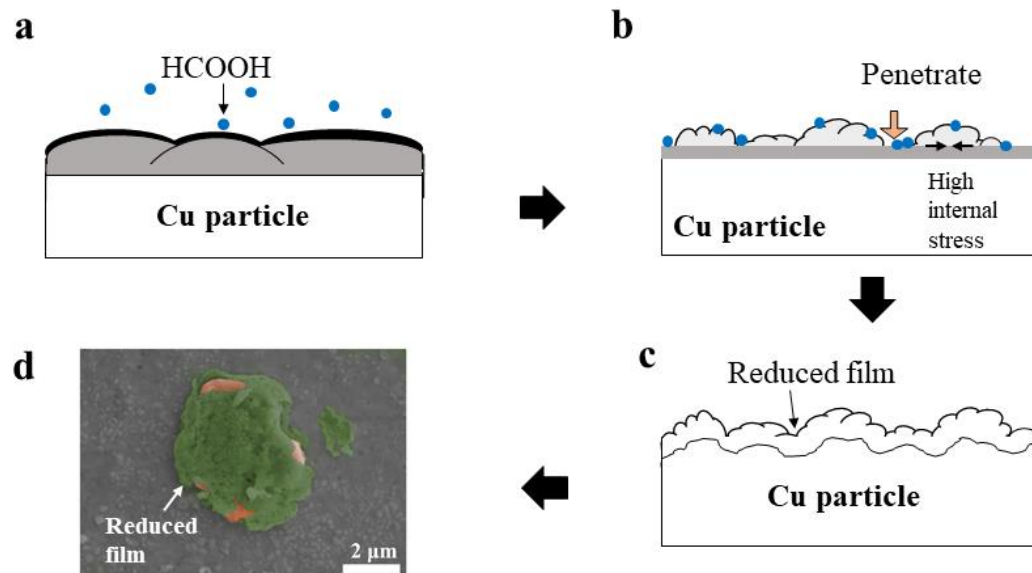


Figure 2.10 Transformation of the preoxidized Cu microparticles by formic acid atmosphere: (a-c) schematic diagram, and (d) a SEM image of the Cu microparticles preoxidized for 30 min and reduced for 30 min.

2.3.3 Cu/Cu joints assembled with preoxidized Cu microparticles and the bonding mechanism

Based on the above analysis, Cu microparticles were preoxidized first and then ground with terpeneol to make a paste, which served as a bonding material and was reduced after formic-acid reductive sintering to assemble joints. Effects of preoxidation time and sintering time on shear strength of the Cu/Cu joints were investigated. **Figure 2.11 a** shows the shear strengths of the Cu/Cu joint specimens with respect to preoxidation time; in this case, sintering time was fixed to 30 min. Without preoxidation, reductive sintering of the Cu microparticles obtained joints with an average shear strength of merely 8 MPa. The maximum average shear strength (~28 MPa) was obtained at a preoxidation time of 30 min, and this value decreased to ~17 MPa when the preoxidation time increased to 40 min. **Figure 2.11 b** illustrates the changes occurring in the bonding strength of Cu microparticles subjected to reduction with formic acid for different time periods. In this case, the preoxidation time was fixed at 30 min. The shear strength of the bonded specimens increased significantly with increasing sintering time. The average shear strength of the joints was only ~12 MPa when the sintering time was 10 min, while it reached ~33 MPa when the sintering time increased to 40 min. It is noted that specimens heated in N_2 instead of formic acid atmosphere for 40 min failed to achieve bonding; therefore, heating time is unlikely the exclusive factor affecting shear strength. These findings suggest that a preoxidation time less than 40 min, and a sintering time greater than 20 min should be adopted.

The joints obtained with 30-min preoxidation and 30-min sintering were chosen as a research subject to study the bonding mechanism. The XRD pattern of the sintered matrix is shown in **Figure 2.12 a**,

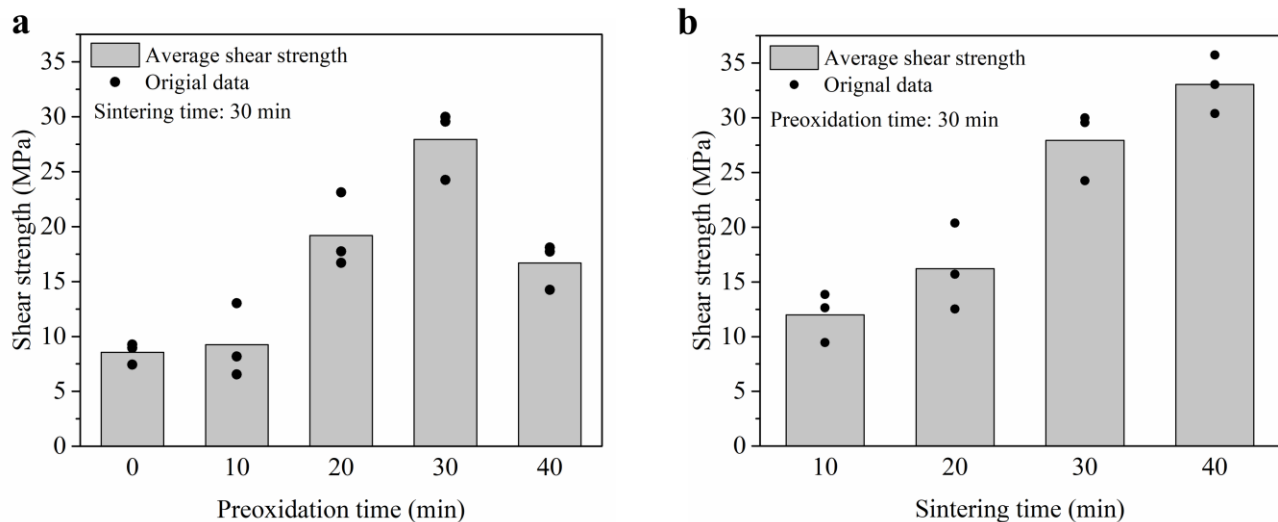


Figure 2.11 Shear strength of bonded Cu/Cu joints assembled at 300 °C under different conditions: (a) 0, 10, 20, 30, and 40 min of preoxidation + 30 min of reductive sintering and (b) 30 min of preoxidation + 10, 20, 30, and 40 min of reductive sintering.

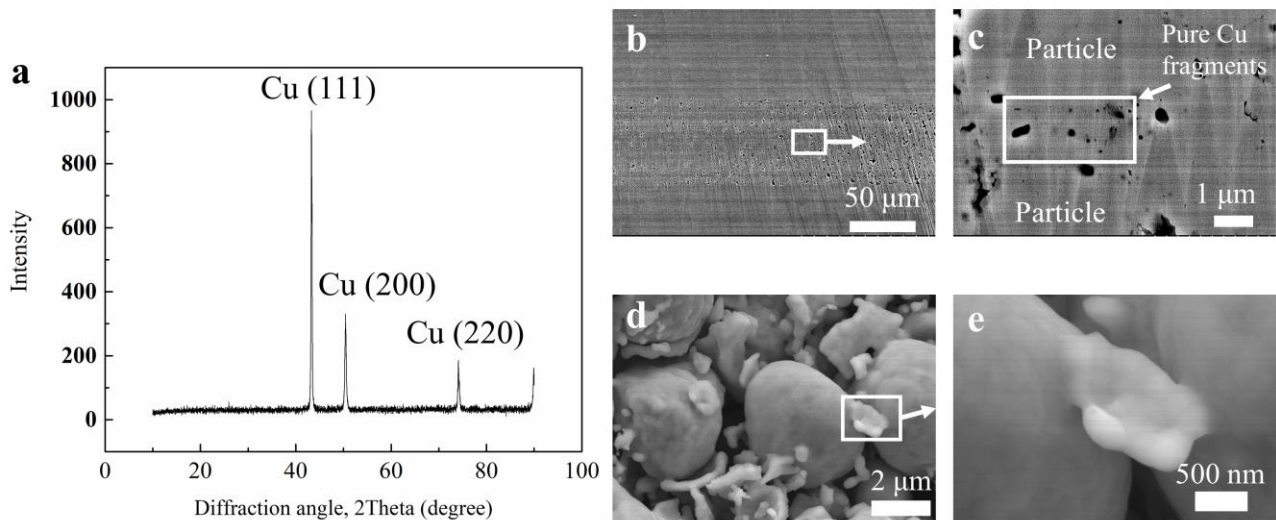


Figure 2.12 The Cu/Cu joints assembled by reductively sintering 30-min preoxidized Cu microparticles at 300 °C for 30 min: (a) XRD pattern of the sintered matrix, (b, c) cross-sectional SEM images of the joints, and (d, e) fracture surface of the joints showing linkages between microparticles.

which suggests that all the Cu oxide was completely reduced to Cu. The cross-sectional SEM images are shown in **Figure 2.12 b**, which show a denser sintered matrix comparing with the joints assembled by directly sintering Cu microparticles [19]; this is because that the Cu oxide fragments became fillers for the gaps between Cu microparticles and were eventually transformed into pure Cu in the formic acid atmosphere, as shown in **Figure 2.12 c**. The parent Cu microparticles and the fragments are also observed in the fracture surface of the joint, as shown in **Figure 2.12 d**. Just like the cross-sectional images, pure Cu fragments concentrated in the gaps between parent Cu microparticles, which acted as linkages between microparticles, bonding them together, as shown in **Figure 2.12 e**.

From these observations, the bonding mechanism can be illustrated in **Figure 2.13** and described as

follows. With the precisely controlled preoxidation process, a homogeneous oxide layer with oxide nanoparticles on the surfaces covered the Cu microparticles. During mechanical grinding, the oxide layers cracked into smaller flake fragments, and the nanoparticles detached. Therefore, the paste consisted of the parent Cu microparticles, the Cu oxide fragments, and the Cu oxide nanoparticles. Cu oxide fragments intercalated between Cu microparticles and reacted with formic acid to generate Cu formate. Meanwhile, the surface of the Cu microparticles also reacts with formic acid, generating the same product. These two Cu formate surfaces merge and replace high-energy free surfaces with low-energy grain boundaries, which are eventually eliminated by grain growth with sufficient process time. Thus, the linkages formed when the oxide fragments transformed into Cu formate. Subsequently, Cu formate decomposes to pure Cu, and the Cu/Cu joints eventually are assembled by the reductive sintering of preoxidized Cu microparticles.

Since the oxide formed during the preoxidation and their transformation in the following reduction are highly related to bonding quality, the influences of preoxidation time and sintering time on joint shear strength (**Figure 2.11**) are easy to explain. The shear strength continuously increased with increasing sintering time, because of the enhanced reduction of Cu oxide by formic acid and grain growth at linkage interfaces due to long process times. However, the strengthening of preoxidation on joints highly relies on the surface morphology of the Cu microparticles; therefore, the relationship between preoxidation time and shear strength presents a different pattern. Shear strength reached the maximum at a preoxidation of 30 min because the oxide layers were covered by oxide nanoparticles and whiskers (**Figure 2.6 g and h**).

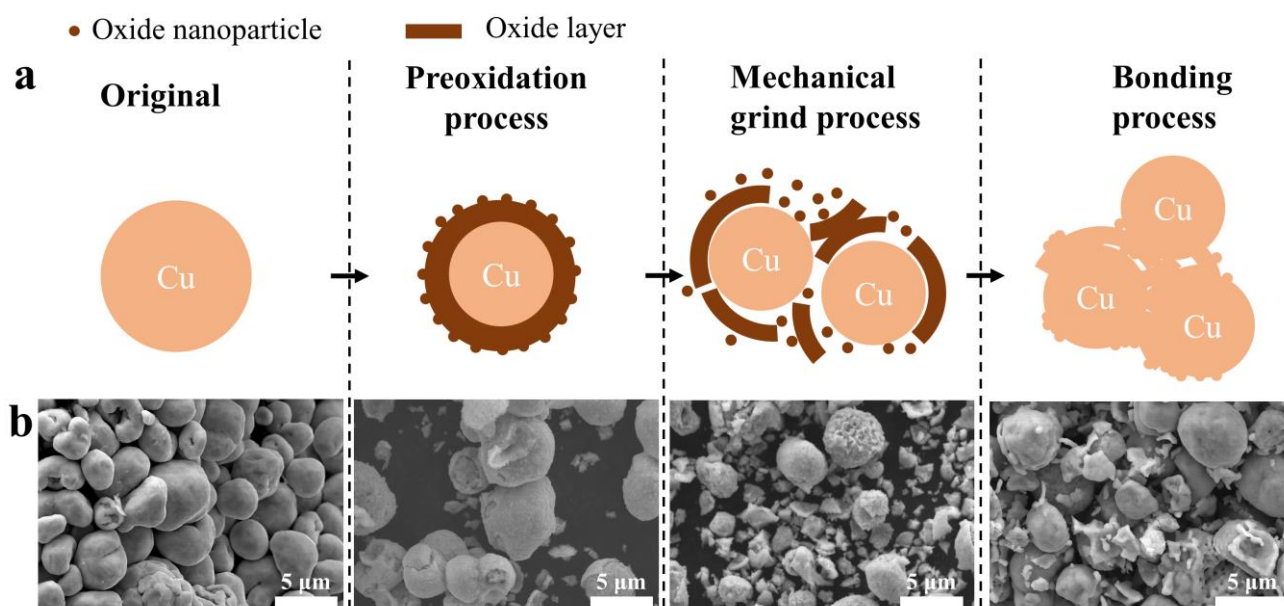


Figure 2.13 The transformation of the Cu microparticles after different process: (a) schematic diagram, and (b) corresponding SEM images.

It has been reported that the structures with high interfacial energy such as nanoparticles are attributed to large amounts of micro defects, which provide many short path diffusion channels that accelerate interdiffusion [20]. Because the process developed in this study relies heavily on interdiffusion between the reactants, high-energy structures are critical for good bonding quality because they promote sintering and diffusion. However, after 40 min of preoxidation, Cu oxide nanoparticles started to coalesce to form a matured oxide layer with lower surface energy (**Figure 2.6 j**), and the oxide layer was barely thickened; therefore, the interdiffusion that drove the elimination of free surfaces was slowed down, hence the lower shear strength.

2.4 Conclusion

With a reductive sintering process, preoxidized Cu microparticles were bonded at 300 °C in the formic acid atmosphere, and reliable Cu/Cu joints with a maximum average shear strength of ~33 MPa were successfully obtained in 40 min. The transformation of the Cu microparticles during preoxidation and following reduction were investigated, and the bonding mechanism was studied. The main conclusions are addressed as follow:

1. During the preoxidation, Cu_2O is the main product. With the peroxidation process extending, Cu oxide nanoparticles and oxide whiskers successively form on the surfaces; when they coarsen into matured oxide layers, the thickness of the oxide layer and the morphologies of the surfaces barely change further.
2. Formic acid penetrates the compact oxide layer covering on the Cu microparticle surfaces due to volume shrinkage induced by the reductive reaction and is able to completely reduce oxide to pure Cu.
3. During the bonding process, the oxide is separated and crack into entities intercalating between the Cu microparticles as fillers, reacting with formic acid to merge into continuous Cu formate linkages, bonding parent Cu microparticle together. The formate linkages later decompose to Cu, and thus Cu/Cu joints could be assembled.

Reference

1. He, S. and H. Nishikawa, Effect of substrate metallization on the impact strength of Sn-Ag-Cu solder bumps fabricated in a formic acid atmosphere, 2017 International Conference on Electronics Packaging (ICEP), (2017) 381-385.
2. He, S., R. Gao, J. Li, Y.-A. Shen, and H. Nishikawa, In-situ observation of fluxless soldering of Sn-3.0Ag-0.5Cu/Cu under a formic acid atmosphere. *Materials Chemistry and Physics*, (2019) 122309.
3. Lin, W. and Y. Lee, Study of fluxless soldering using formic acid vapor. *IEEE transactions on Advanced Packaging*, **22** (1999) 592-601.
4. He, S., R. Gao, Y.-A. Shen, J. Li, and H. Nishikawa, Wettability, interfacial reactions, and impact strength of Sn–3.0Ag–0.5Cu solder/ENIG substrate used for fluxless soldering under formic acid atmosphere. *Journal of Materials Science*, **55** (2020), 3107–3117.
5. Liu, J., H. Chen, H. Ji, and M. Li, Highly conductive Cu–Cu joint formation by low-temperature sintering of formic acid-treated Cu nanoparticles. *ACS applied materials & interfaces*, **8** (2016) 33289-33298.
6. Bowker, M., E. Rowbotham, F. Leibsle, and S. Haq, The adsorption and decomposition of formic acid on Cu {110}. *Surface science*, **349** (1996) 97-110.
7. Fujino, M., M. Akaike, N. Matsuoka, and T. Suga, Reduction reaction analysis of nanoparticle copper oxide for copper direct bonding using formic acid. *Japanese Journal of Applied Physics*, **56** (2017) 04CC01.
8. He, L., J. Li, X. Wu, F. Mu, Y. Wang, Y. Lu, and T. Suga, Robust Ag-Cu Sintering Bonding at 160° C via Combining Ag₂O Microparticle Paste and Pt-Catalyzed Formic Acid Vapor. *Metals*, **10** (2020) 315.
9. Liu, X. and H. Nishikawa, Improved Joint Strength with Sintering Bonding Using Microscale Cu Particles by an Oxidation-Reduction Process, Electronic Components and Technology Conference (ECTC), 2016 IEEE 66th, 2016, 455-460.
10. Cocke, D.L., R. Schennach, M. Hossain, D. Mencer, H. McWhinney, J. Parga, M. Kesmez, J. Gomes, and M. Mollah, The low-temperature thermal oxidation of copper, Cu₃O₂, and its influence on past and future studies. *Vacuum*, **79** (2005) 71-83.
11. Lenglet, M., K. Kartouni, J. Machefert, J. Claude, P. Steinmetz, E. Beauprez, J. Heinrich, and N. Celati, Low temperature oxidation of copper: The formation of CuO. *Materials research bulletin*,

- 30** (1995) 393-403.
12. Pilling, N., The oxidation of metals at high temperature. *J. Inst. Met.*, **29** (1923) 529-582.
 13. Xu, C. and W. Gao, Pilling-Bedworth ratio for oxidation of alloys. *Material Research Innovations*, **3** (2000) 231-235.
 14. Joliff, Y., J. Absi, M. Huger, and J.C. Glandus, Microcracks with unexpected characteristics induced by CTE mismatch in two-phase model materials. *Journal of materials science*, **43** (2008) 330-337.
 15. Xu, C.H., C.H. Woo, and S.Q. Shi, Formation of CuO nanowires on Cu foil. *Chemical Physics Letters*, **399** (2004) 62-66.
 16. Singh, A.K., S. Singh, and A. Kumar, Hydrogen energy future with formic acid: a renewable chemical hydrogen storage system. *Catalysis Science & Technology*, **6** (2016) 12-40.
 17. Conti, F., A. Hanss, C. Fischer, and G. Elger, Thermogravimetric investigation on the interaction of formic acid with solder joint materials. *New Journal of Chemistry*, **40** (2016) 10482-10487.
 18. Hayden, B., K. Prince, D. Woodruff, and A. Bradshaw, An IRAS study of formic acid and surface formate adsorbed on Cu (110). *Surface science*, **133** (1983) 589-604.
 19. Liu, X. and H. Nishikawa, Low-pressure Cu-Cu bonding using in-situ surface-modified microscale Cu particles for power device packaging. *Scripta Materialia*, **120** (2016) 80-84.
 20. Li, J., X. Li, L. Wang, Y.-H. Mei, and G.-Q. Lu, A novel multiscale silver paste for die bonding on bare copper by low-temperature pressure-free sintering in air. *Materials & Design*, **140** (2018) 64-72.

Chapter 3

Rapid ultrasonic-assisted bonding process using Ag microparticles under ambient atmosphere

3.1 Introduction

Although reliable Cu/Cu joints have been assembled by a reductive bonding process in *Chapter 2*, the process is hardly satisfying because it requires a long process time, and formic acid vapor is a pollutant. We propose to develop a bonding process with better manufacturability, short process time, and no involved hazardous substances. Introducing assisting energy to improve the sinterability of microparticles is a feasible approach to assemble die-attach bonding at low temperatures, and ultrasonic vibration exhibits great potential. Because there have been few attempts, before applying the ultrasonic vibration in bonding process using Cu microparticles, the possible effects on low-temperature sintering of metallic microparticles and corresponding mechanisms should be evaluated. Because Cu readily introduces

difficulties and interference variables (e.g. oxidation) in analysis due to its active chemical property, silver (Ag), as a common bonding material that is widely used in die attaching and possesses excellent oxidation resistance, is suitable for preliminary analysis before developing an ultrasonic-assisted bonding process for Cu microparticles.

In this study, chestnut-burr-like Ag microscale particles (hereinafter in this chapter referred to as Ag microparticles) were used as filler materials, because this kind of Ag microparticles have been reported to be capable of assembling joints at a temperature of 300 °C and under bonding pressure of 10 MPa [1]. The effect of ultrasonic vibration on the transformation of the microparticles and mechanical property of the joints were studied by observing fracture surfaces, cross-sections, and bonding interfaces of the joints. Based on the results of our observations, the feasibility of ultrasonic assist in the bonding process was discussed, and process parameters and corresponding effects were investigated.

3.2 Experimental

3.2.1 Materials and sample fabrication

Chestnut-burr-like Ag microparticles (TK Ag particle, KAKEN TECS Co., Ltd), which are covered by needles, were used in this study, as shown in **Figure 3.1 a**; the average diameter of the microparticles was 3 μm . The microparticles were mixed with 20 wt.% glycol ether-based solvent to fabricate the Ag paste. Electroless nickel immersion gold-finished Cu cylindrical disks (hereinafter referred to as the ENIG disks) were used to fabricate the joint specimens to prevent oxidation. Two different kinds of Cu disks were used as upper disks and bottom disks. To prepare a joint specimen, the Ag paste was first printed to the surfaces of bottom disks with a thickness of 150 μm , then the upper disks were placed on the printed paste; the dimensions of the joint specimen were illustrated in **Figure 3.1 b**.

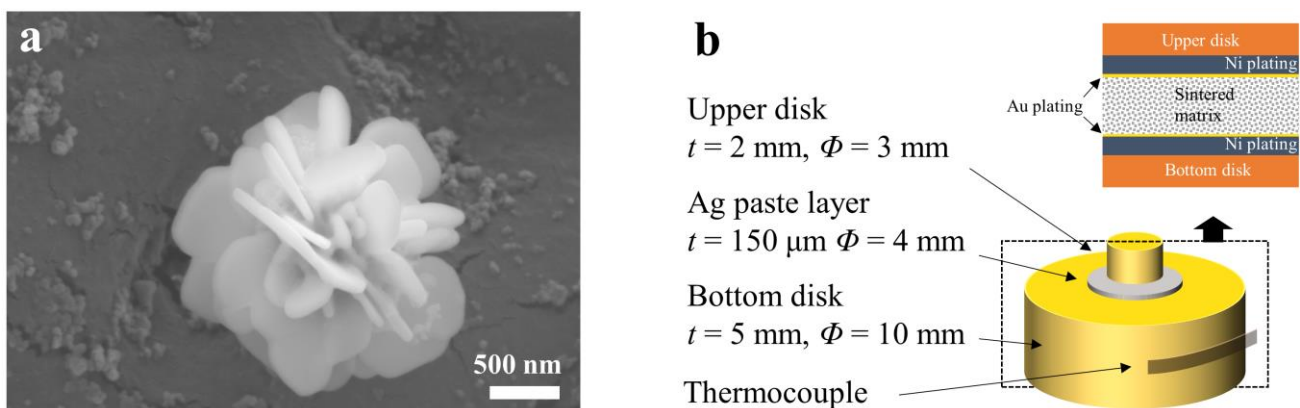


Figure 3.1 Materials used in this study: (a) the chestnut-burr-like Ag microparticles, and (b) a schematic of the joint specimen.

The thermal property of the Ag paste was tested by a simultaneous thermogravimetric analyzer (STA7200, Hitachi) to determine process parameters. DTA and TG curves of the Ag paste used in this study at rising temperatures from 20 - 500 °C with a rate of 0.5 °C/min, and results are shown in **Figure 3.2 a**. The TG curve declined when the temperature reached 90 °C, indicating the evaporation of the solvent started at this point. A peak appeared in the DTA curve without changes in the TG curve, revealing that the Ag microparticles are able to sinter at 264 °C. TG curves of the Ag paste at constant temperatures were illustrated to study the evaporation and decomposition behaviors of the paste solvents, because it has been reported that residues of organic solvents would hinder sintering and diffusion [2]. Since the purpose of this study is to develop a low-temperature bonding process, two relatively low temperatures (90 °C and 230 °C) and one high temperature (300 °C) were chosen for the investigation, and the results are shown in **Figure 3.2 b**. Obviously, when the temperature was 90 °C, the solvent in the paste still could not be consumed completely even after 10 min of duration, while it was exhausted at 230 °C in ~3 min and at 300 °C in ~2 min. It is noted that at 300 °C, the mass loss of the paste heating at 300 °C is less than that of the paste heating at 230 °C. According to the TG curve of the Ag paste heating at 300 °C in N₂, which shows a similar mass loss with that obtained at 230 °C, the increase in residue mass could be explained by oxidation of Ag microparticles. Since oxide not only hinder sintering but also degrade conductivity and mechanical performance of bonded joints, the temperatures of specimens during the bonding process (actual temperatures) should reach 240 °C to avoid oxidation and evaporate solvent completely. In this study, as the processes were conducted in ambient air instead of in an air-tight chamber, and the only heating source is the bottom heating unit while the ultrasonic head was a cold end, the actual temperatures of the specimens during the processes were lower than the temperature setting of the heating

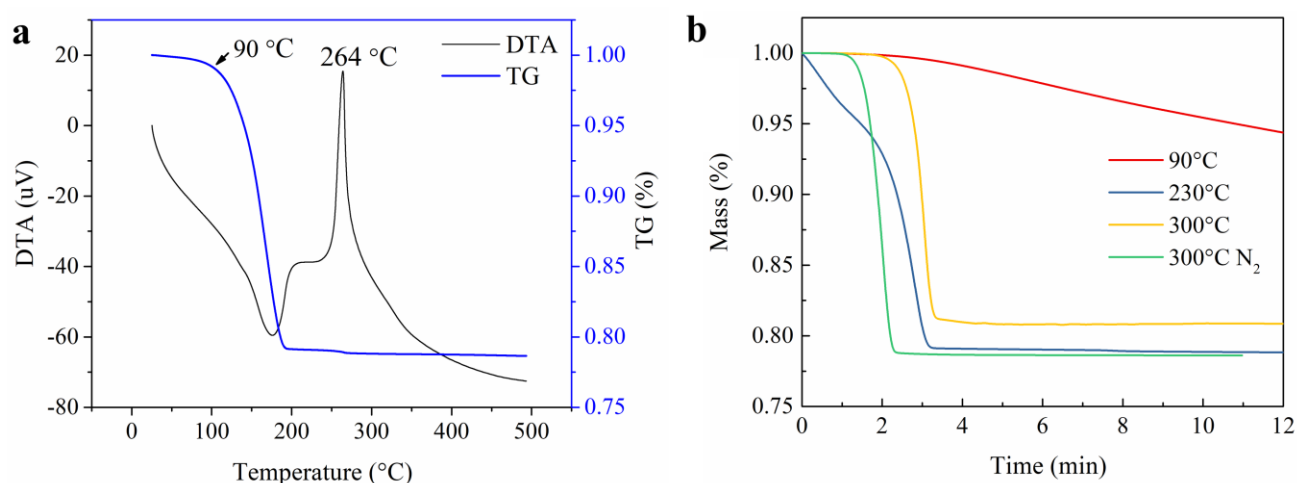


Figure 3.2 Thermal properties of (a) the Ag paste with temperature rising from 20 – 500 °C, and (b) the Ag paste at different constant temperatures and atmosphere.

unit. After tests, it is known that for the actual temperature of the joint specimen reach 240 °C, the bottom heating unit needs to be set at 300 °C.

3.2.2 Method and processing

A thermal pressure bonding machine (HTB - MM, Alpha Design Co., Ltd) was modified by attaching an ultrasonic head (horn) and an ultrasonic generator; a schematic of the modified bonding facility is illustrated in **Figure 3.3 a**. The bottom heating unit was the only heat source for temperature control. The pressure, applied to guarantee good contact between specimens and the ultrasonic head, was set to 50 N (approximately 7 MPa) for each specimen. The frequency of ultrasonic vibration was set to 50 kHz. The ultrasonic power was controlled through the ultrasonic vibration amplitude, which was set between 2 to 5 μm to maintain a low ultrasonic power in case of chip damage. The relationship between the vibration amplitude and ultrasonic output power of the bonding device is shown in **Table 3.1**. For ease of expression, the ultrasonic output power ranges corresponding to different ultrasonic amplitudes are represented as the “representative power” in this chapter. The preheating temperature was set at 130 °C for 50 s first, then the setting temperature was increased to 300 °C and held for 250 s with the ultrasonic vibration being applied to the specimens, as shown in **Figure 3.3 b**. Both the process with the ultrasonic vibration (ultrasonic process) and the process without the ultrasonic vibration (non-ultrasonic process) were conducted with the same heating profile in the ambient air. During the processes, a thermocouple was

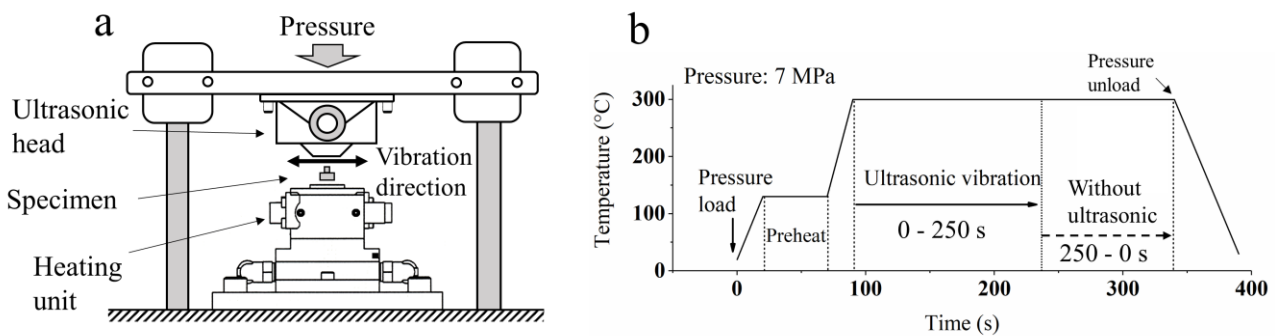


Figure 3.3 Joint specimen fabrication: (a) schematic diagram of the modified ultrasonic-assisted bonding machine, and (b) the heating profile of the process.

Table 3.1 Relationship between ultrasonic amplitude and output power of the bonding device.

Amplitudes (μm)	2	2.5	3.5	4	5
Output power (W)	1	2	3-4	6-8	8-12
Representative Power (W)	1	2	3	6	8

attached to the side of the bottom disks (**Figure 3.1b**) to measure the temperature of the specimens in real-time.

3.2.3 Characterization methods

The thermal property of the Ag paste was tested by a simultaneous thermogravimetric analyzer (STA7200, Hitachi) to determine process parameters. After that, the specimens were bonded using optimized parameters then sheared using a shear tester (STR-1000, Rhesca) to evaluate their shear strength. The average shear strength of the joints obtained under different conditions was determined using 3 specimens; standard deviations were represented by error bars. After the shear tests, the fracture surfaces were observed using a field scanning electron microscope (FESEM; SU-70, Hitachi). The cross-section samples were polished using a cross-section polisher (SM-09010, JEOL) with ion milling to prevent the microparticles from smearing into the pores during grinding and polishing. The grain sizes and grain orientations of the bonding layers were examined using electron backscatter diffraction (EBSD, TSL OIM) equipped with an SEM (JSM-7100F, JEOL). A transmission electron microscope (TEM; JEM-2100, JEOL) and an electron probe microanalyzer (EPMA; JXA-8530F, JEOL) were used to analyze the microstructures and elemental distributions in the bonded specimens, respectively.

3.3 Results and discussions

3.3.1 Effects of ultrasonic vibration on bonding process and sintered joints

The effect of the ultrasonic vibration on actual temperatures of the joint during the bonding processes was investigated, and the real-time temperature curves of the joint specimens during a non-ultrasonic process and an ultrasonic process with ultrasonic power of 8 W are shown in **Figure 3.4**. As mentioned, the actual peak temperature of the specimens was approximately 240 °C when the bottom heating unit was set at 300 °C. The ultrasonic vibration was applied when the setting temperature reached 300 °C, and the actual temperature was increased almost immediately, which was stabilized quickly within 20 s. After stabilization, the actual temperatures of specimens in the non-ultrasonic process (230 °C) were lower than those with the ultrasonic process (243 °C), and both temperature curves are parallel. Both temperatures rose gradually until the rise of ~10 °C at the end of the processes, which is due to continuous heating. The average difference between the actual temperatures of the specimens with and without the ultrasonic process was approximately 9 °C.

The duration of ultrasonic vibration (ultrasonic time) and output power of ultrasonic vibration (ultrasonic power) are critical parameters for the ultrasonic-assisted bonding method. The influences of

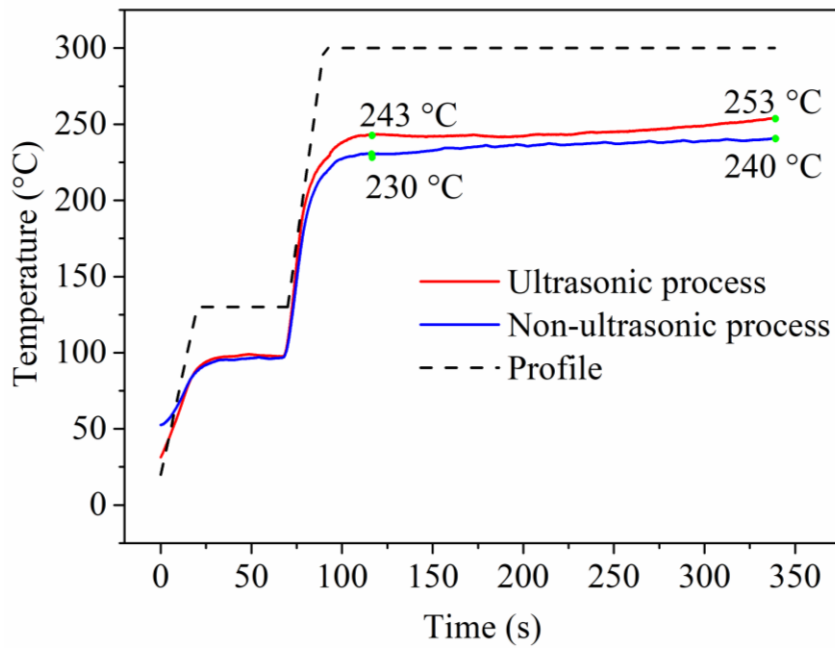


Figure 3.4 Real-time actual temperatures when the specimens were assembling at 300 °C by the non-ultrasonic process and the ultrasonic process with an ultrasonic power of 8 W.

ultrasonic time on mechanical performance was first investigated by shearing the joints assembled with different ultrasonic times (0 – 250 s) and a fixed ultrasonic power of 8 W, and shear strength are shown in **Figure 3.5 a**. Overall, the average shear strength increased greatly with increasing ultrasonic time until ultrasonic time exceeding 100 s. The average shear strength of the joints assembled without the ultrasonic vibration was 16.6 MPa. Conversely, the average shear strength greatly increased to 36.2 MPa by applying the ultrasonic vibration for 100 s. With further extending of ultrasonic time, the average shear strength barely increased, reaching 37.3 MPa when ultrasonic time was 250 s.

The influence of ultrasonic power on mechanical performance was investigated by shearing the joints assembled with different ultrasonic power (0 – 8 W) and a fixed ultrasonic time of 250 s, and shear strength are shown in **Figure 3.5 b**. When the ultrasonic vibration was applied with power of 1 W, the average shear strength decreased to 9.9 MPa. With power increasing to 2 W, the shear strength increased to 16.7 MPa, which is approximately the same value as that obtained by the non-ultrasonic process. With the increase in ultrasonic power to 3 W, the shear strength dramatically increased to 32.5 MPa. After that, only a slight increase in the shear strength was caused by increasing ultrasonic power, and the maximum shear strength was 37.3 MPa with an ultrasonic power of 8 W.

3.3.2 Evolution of sintered microparticles under ultrasonic vibration

Figure 3.6 shows the fracture surfaces and cross-sectional microstructures of the Ag-sintered joints assembled with an ultrasonic power of 8 W but different ultrasonic time. In general, the morphologies of

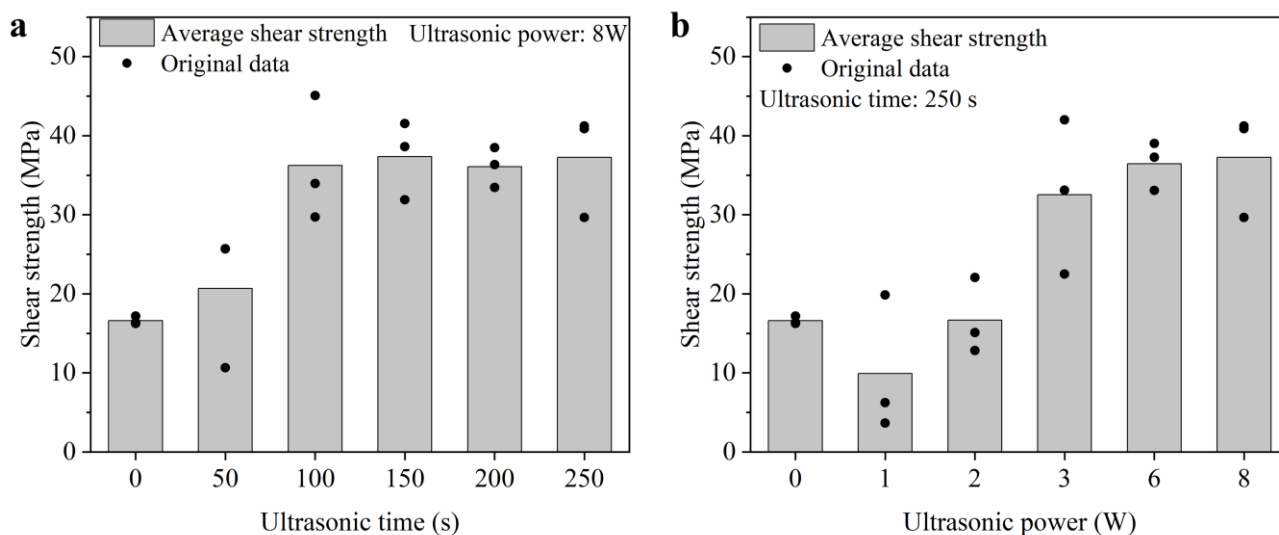


Figure 3.5 Shear strength of the joints assembled at setting temperature of 300 °C for 250 s with (a) an ultrasonic power of 8 W and various ultrasonic time, and (b) an ultrasonic time of 250 s and various ultrasonic power.

the microparticles changed with extending ultrasonic time, and needles were found to transform into micro bridges bonding the microparticles. The “micro bridges” refers to sintering necks transformed from the needles during processes. After the non-ultrasonic process (0 s), the morphology of the microparticles barely changed, although some micro bridges formed between the microparticles by the needles, as shown in both the fracture surface and the cross-section (**Figure 3.6 a** and **f**). In the joints obtained with ultrasonic time of 50 s (**Fig. 3.6 b** and **g**), slight deformation of the microparticles and more micro bridges can be observed from the fracture surface. The deformation became large when ultrasonic time extends to 100 s, (**Fig. 3.6 c** and **h**), making it difficult to distinguish independent microparticles, revealing a complete sintered structure. Additionally, a large number of dimples appeared on the fracture surface, which is usually considered as the morphology of ductile fracture. With the ultrasonic time extended to 150 s and 300 s, there was no significant microstructural change from their fracture surfaces and cross-sectional microstructures (**Figure 3.6 d, e, i, and j**). That is to say, 100 s has been enough for the ultrasonic bonding completed with the ultrasonic power of 8 W.

Figure 3.7 depicts the fracture surfaces and cross-sectional microstructures of the joints assembled with an ultrasonic time of 250 s and different ultrasonic power. After the ultrasonic process of 1 W, some micro bridges were observed to pull apart in the fracture surface, while the morphology of the microparticles maintains unchanged, as shown in **Figure 3.7 a** and **e**. When ultrasonic power increases to 2 W, the fracture surface and cross-sectional microstructures (**Figure 3.7 b** and **f**) were similar to the samples obtained with the non-ultrasonic process (**Fig. 3.6 a** and **f**): the needles represent little deformation to form some micro bridges, and independent microparticles were readily recognized. After

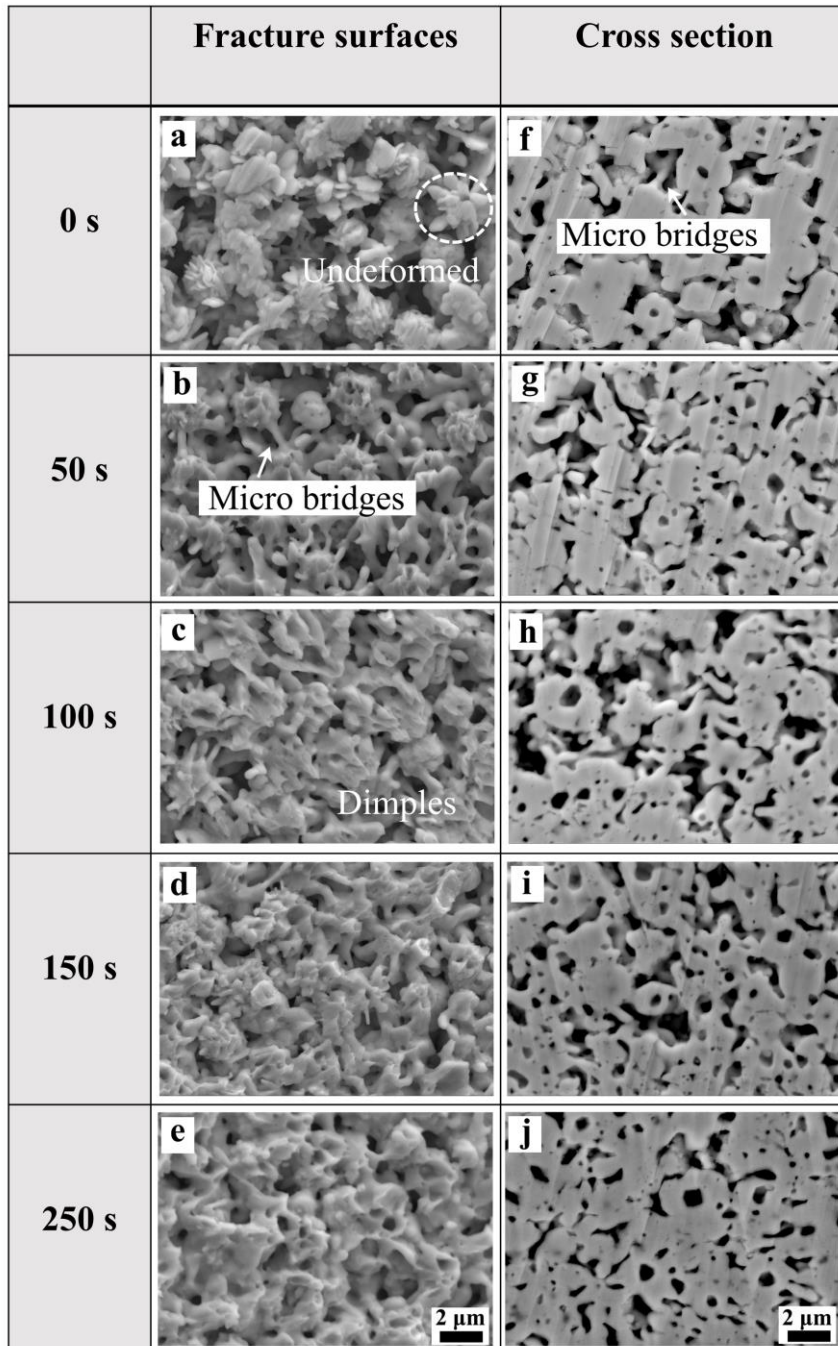


Figure 3.6 Fracture surfaces and cross sections of the joints assembled at a setting temperature of 300 °C with a fixed ultrasonic power of 8 W and ultrasonic time of (a, f) 0 s, (b, g) 50 s, (c, h) 100 s, (d, i) 150 s, and (e, j) 250 s.

the ultrasonic process of 3 W, the microparticles were greatly deformed and tightly bonded (**Figure 3.7 c** and **g**); meanwhile, considerable dimples appeared after the shear test (**Figure 3.7 c**). After the ultrasonic process of 6 W and 8 W, the fracture surfaces and cross-sectional microstructures of Ag-sintered joints (**Figure 3.7 d, h** and **Figure 3.6 e, j**) were both similar to that assembled with the power of 3 W. It is noted that pores were found in all cross-sectional microstructures, which resulted from the gaps between the needles and the microparticles; however, based on the observation on cross-sectional microstructures, the density of the sintered matrix barely varied with increasing ultrasonic power.

The microstructural evolution of the Ag microparticles in the ultrasonic process was observed. The

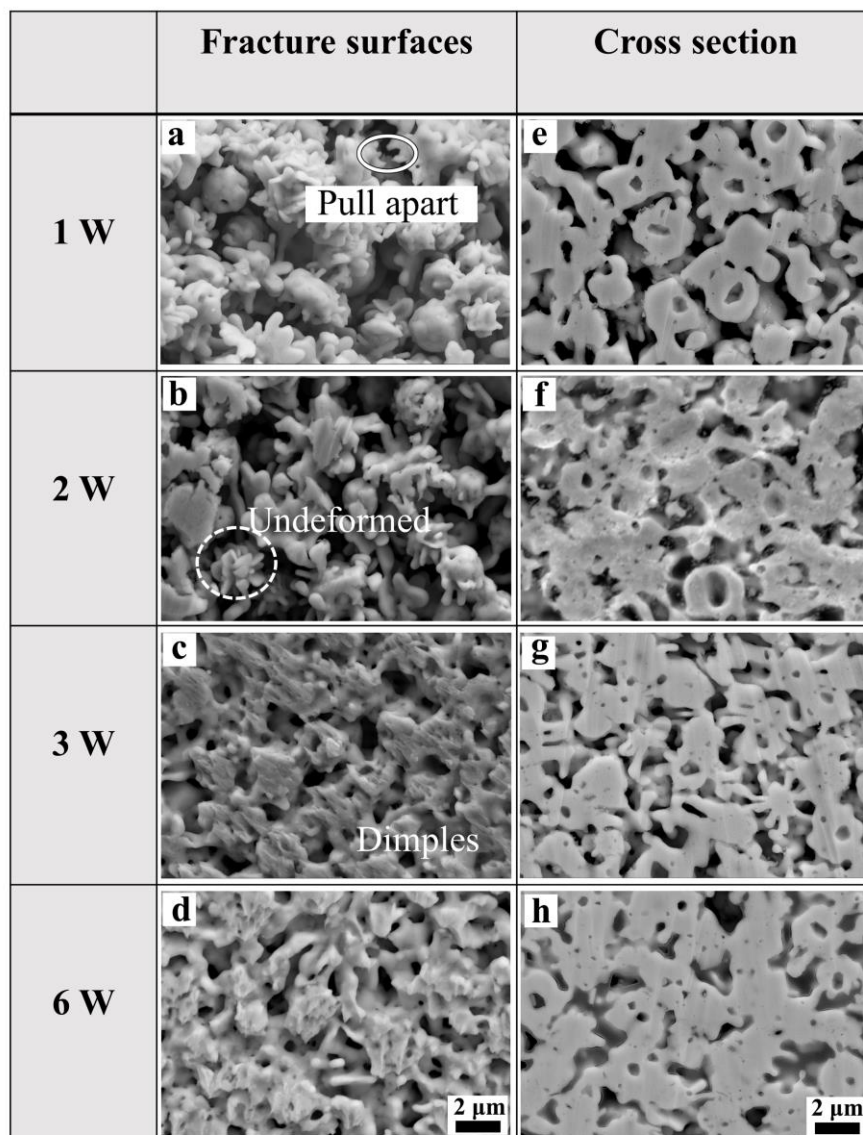


Figure 3.7 Fracture surfaces and cross sections of the joints assembled at a setting temperature of 300 °C with a fixed ultrasonic time of 250 s and ultrasonic power of (a, g) 1 W, (b, h) 2 W, (c, i) 3 W, (d, j) 6 W. (see 0 W and 8 W in Figure 3.6 (a, f) and Figure 3.6 (e, j), respectively)

joint specimens in different stages of the process were taken out and made as samples to observe fracture surfaces and cross-sections, as shown in **Figure 3.8 a**. To maximize the effect of the ultrasonic vibration for better observation, the ultrasonic time and the ultrasonic power were set to 250 s and 8 W, respectively. After the first 50 s of the process, as shown in **Figure 3.8 b** and **c**, the microparticles barely deformed and were bonded; however, some needles bonded to form micro bridges. After 100 s, the microparticles remain their morphologies while needles became rounded, and more micro bridges were observed (**Figure 3.8 d** and **e**). After 150 s of the process, as shown in **Figure 3.8 f** and **g**, a large number of dimples were observed on the fracture surface, and individual microparticles were no longer identified because they greatly deformed, bonding tightly with the surrounding particles. With the ultrasonic process

continuing, the microparticles eventually became completely sintered, as shown in **Figure 3.8 h, i, j, and k**, while only slight changes occurred to the morphology of the bonding layers after 150 s.

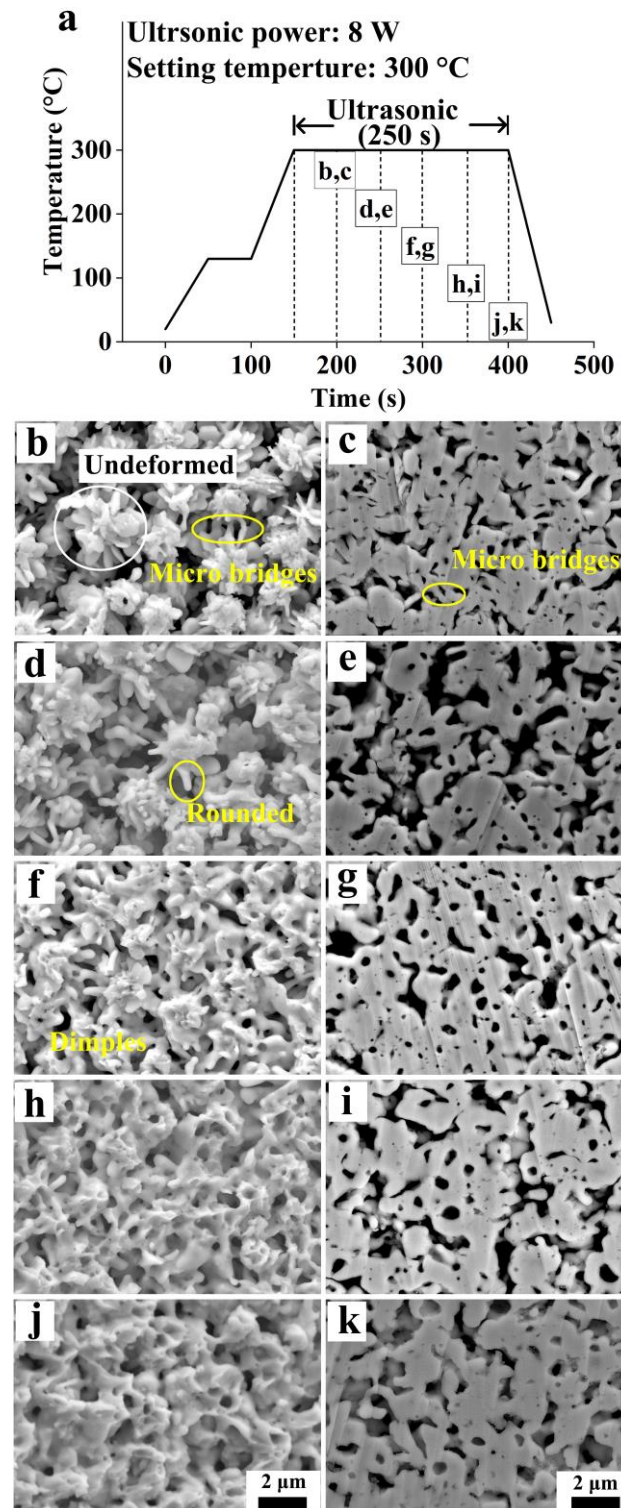


Figure 3.8 Microstructural evolution of the Ag microparticles in the ultrasonic process (250 s, 8 W): (a) stages presented in (b - k), and fracture surface (left column) and cross-section (right column) SEM images of the joints after (b, c) 50 s, (c, d) 100 s, (e, f) 150 s, (g, h) 200 s and (i, j) 250 s of the process.

Although SEM images showed the different microstructures between Ag-sintered joints assemble by ultrasonic and non-ultrasonic processes, their details, such as the grain sizes and orientations, have to be analyzed by EBSD. Assembled at 300 °C for 250s, joints obtained by a non-ultrasonic process and an ultrasonic process (250 s, 8 W) were compared; SEM images, corresponding orientation maps (OIMs), and grain size distribution of their sintered matrix are shown in **Figure 3.9**. As seen in the OIMs (**Figure 3.9 b and e**), no unidirectional growth of grains was observed in both cases; therefore, the ultrasonic vibration was considered to barely affect grain orientation in solid-state sintering. From the distribution of grain sizes (**Figure 3.9 c and f**), it is noted that the average Ag grain size (0.63 μm) after the ultrasonic

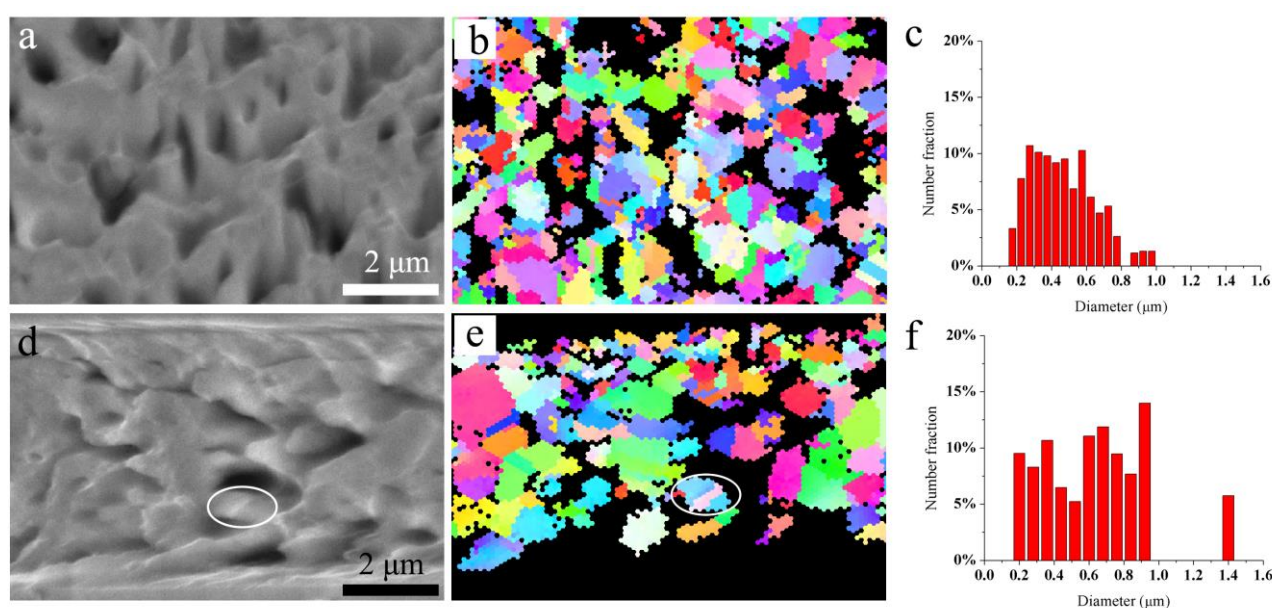


Figure 3.9 Cross-sectional SEM images, EBSD OIMs, and distributions of grain size of the joints assembled at 300° C for 250 s by (a, b, c) the non-ultrasonic process and (d, e, f) the ultrasonic process (250 s, 8 W).

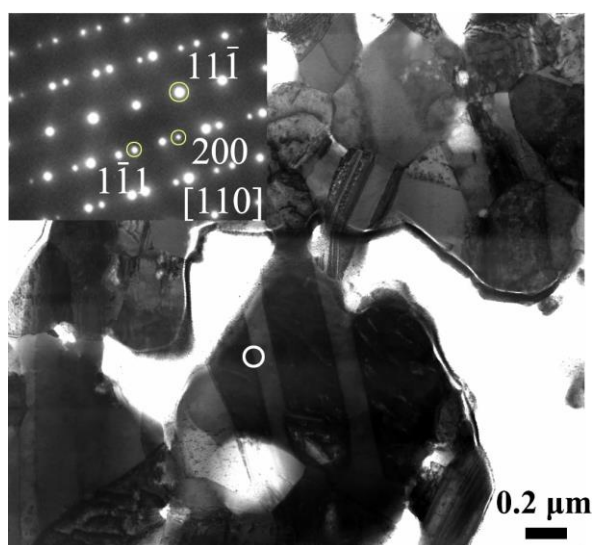


Figure 3.10 STEM image showing the micro bridges formed with the ultrasonic process (250 s, 8 W). Ag twins were identified by $[110]$ diffraction pattern at the white circle.

process was larger than that (0.47 μm) formed after the non-ultrasonic process; additionally, coarser grains, with diameters of approximately 1.4 μm , appeared under the ultrasonic vibration. Twins seem to be observed in micro bridges between two different microparticles, marked in a white circle in **Figure 3.9 d** and **e**. It is not an exceptional phenomenon, because some micro bridges containing twins is confirmed by TEM in **Figure 3.10** after its sample preparation by FIB. Its Ag-sintered joint was fabricated with the ultrasonic power of 8W and the ultrasonic time of 250 s. The diffraction pattern with a classic $\Sigma 3$ coherent boundary in the face-centered cubic structure was captured by selected area diffraction, marked in the white circle in a STEM image.

3.3.3 Effects of the ultrasonic vibration on the joint interfaces

In addition to microstructures of the sintered matrix, microstructures at interfaces also affect the bonding quality. **Figure 3.11** shows the joint interfaces after ultrasonic powers of 0 W, 3 W, and 8 W. Unlike the interfaces obtained by the non-ultrasonic process (**Figure 3.11 a, d, and g**), continuous void-free dense layers are observed at both the upper interface and bottom interface after an ultrasonic process of 3 W and 8 W (**Figure 3.11 b, h, c, and i**), and such dense layer thickened with increasing power. The

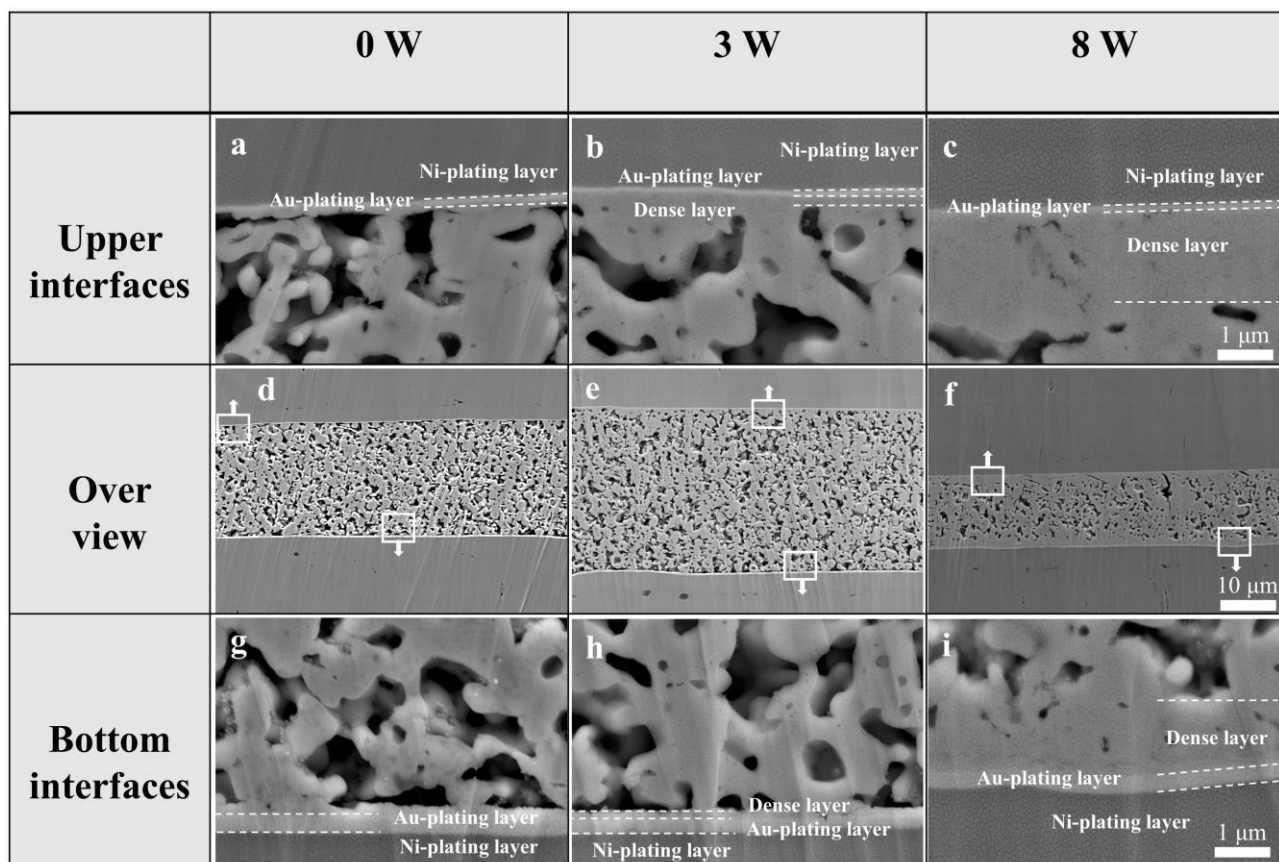


Figure 3.11 Cross-section images of the joints assembled at 300 °C for 250 s by (a, d, g) the non-ultrasonic process and the ultrasonic process with an ultrasonic time of 250 s and an ultrasonic power of (b, c, h) 3 W, and (c, f, i) 8 W.

average thickness of the dense layers was evaluated by taking cross-sectional SEM images of three different areas in each bonding sample, and those SEM images were taken at both the upper and bottom interfaces in each area. Namely, the average thickness of the dense layers was determined by nine SEM images in different regions; they were measured by the commercial software Image-pro Plus. Based on the measurements, when the ultrasonic power was 3 W, the thickness of the upper and bottom layers was 0.65 μm and 0.24 μm , and they increased to 1.33 and 1.32 μm when the ultrasonic power reached 8 W. **Figure 3.12** shows the EPMA mapping revealing elemental distributions at the interfaces of the sintered joint assembled with the ultrasonic process (250 s, 8 W). It is indicated that the dense layers composed only Ag; therefore, they are most likely generated from the consolidation of the Ag microparticles. The ultrasonic vibration barely affected on diffusion behaviors of the Ag microparticles in solid sintering, thus the upper and bottom interfaces exhibit similar element distribution: both Ag and Ni diffused into the Au-plating layer, transforming it to Ag-Au-Ni solid solution.

The microstructures of the dense layers were observed in detail by scanning transmission electron microscopy (STEM). **Figure 3.13** shows the STEM images of a bonded joint assembled with the ultrasonic process (250 s, 8 W). Consistent with the SEM images in **Figure 3.11 c** and **i**, the dense layers appeared at both the upper and bottom interfaces. Interestingly, there were some twin boundaries in the dense layer at the upper interface (**Figure 3.13 a**), indicating that the formation of the deformation twins.

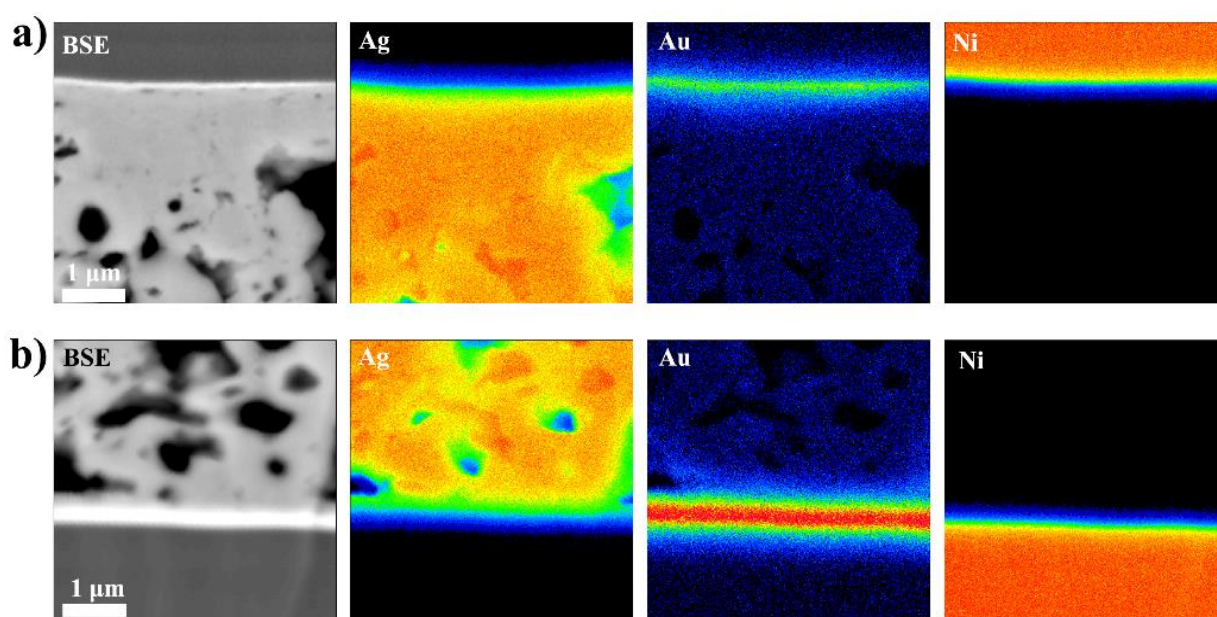


Figure 3.12 Elements distribution of the interfaces obtained at 300 $^{\circ}\text{C}$ with an ultrasonic power of 8 W and an ultrasonic time of 250 s at (a) the upper interface and (b) the bottom interface.

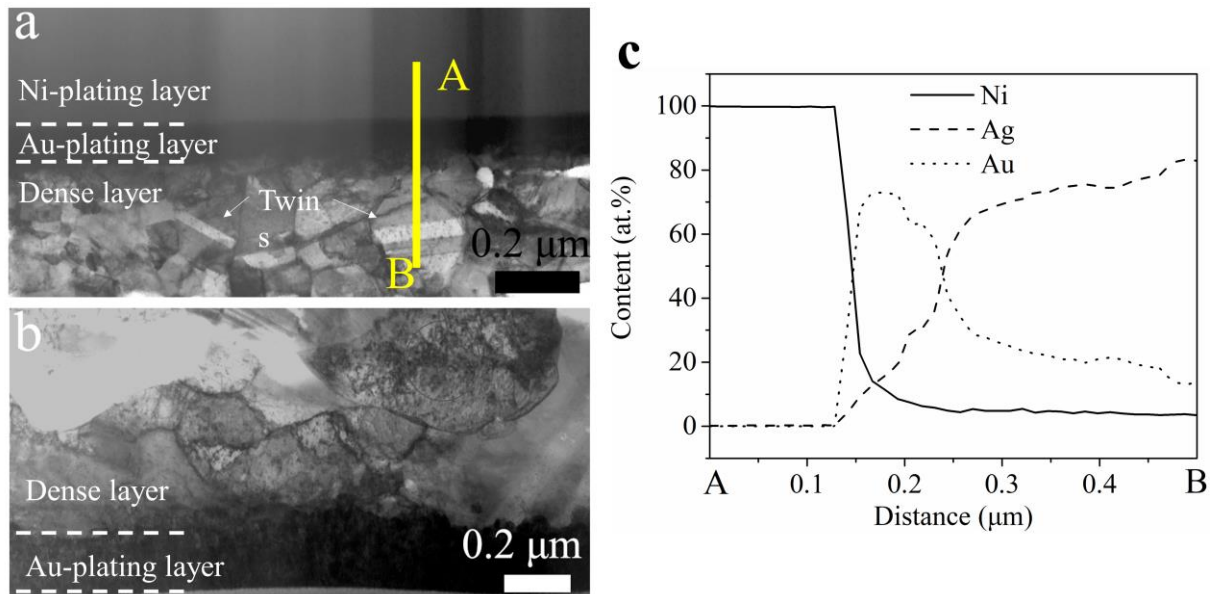


Figure 3.13 Cross-section STEM images showing interfaces of the joint assembled at 300 °C with an ultrasonic power of 8 W and an ultrasonic time of 250 s: (a) the upper interface and (b) the bottom interface, and (c) EDS line scanning in (a).

The grain morphology at the upper interface was equiaxed and was different from that at bottom interfaces (**Figure 3.13 b**). It has been reported that grains under strain affected by ultrasonic vibration can become equiaxed, which is quite different from grain shape without ultrasonic vibration [3].

Of note is that the dense layers affected the fracture portions and behaviors. Joints with the non-ultrasonic process tended to be brittlely debonded at the sintered matrix/substrate interfaces due to their dense layer absence, as shown in **Figure 3.14 a** and **b**. The fractography shows a smooth surface of the bottom disk while that on the upper side shows the sintered matrix. After the ultrasonic process, bonding layers were composed of dense layers and the sintered matrix. In that case, fractures occurred at the dense layer/sintered matrix interfaces. As shown in **Figure 3.14 c, d, e, and f**, fractures on the upper and bottom sides all contained the areas with the sintered matrix attaching and the areas without that. With the part of the sintered matrix attaching to one side, the corresponding area on the other side shows dense layer residues, which exhibit a film morphology and barely contain the microparticles. Considerable dimples are observed on the dense layer residues, revealing a ductile fracture at the sintered matrix/substrate interfaces.

3.3.4 Enhancing Mechanism of ultrasonic vibration on microparticle bonding

The above results show that low-power ultrasonic vibration can enhance bonding of the Ag microparticles at a temperature as low as ~ 240 °C in 120 s. Via a moderate pressure in the normal direction of the bonding surface, the improvement to the bonding reliability is considerable. In the other study using the same Ag microparticles, high bonding temperatures, high pressures, and long processing time were required for fabricating joints with a shear strength above 30 MPa by the thermal compression [1]. The ultrasonic vibration greatly affected the sintered microstructures such as the deformation of the Ag microparticles, numerous formations of the micro bridges and dense layers, thus obviously enhanced the bonding strength of Ag-sintered joints.

Deformation of the Ag microparticles is critical for densification, which mainly relies on the deformation of needles covering the microparticles, according to morphologies shown in **Figure 3.6** and **Figure 3.7**. The stress is mainly concentrated at the flake-shape needles when pressure is loaded, resulting in larger deformation compared with the sphere bulk part in the center, hence the initial densification and

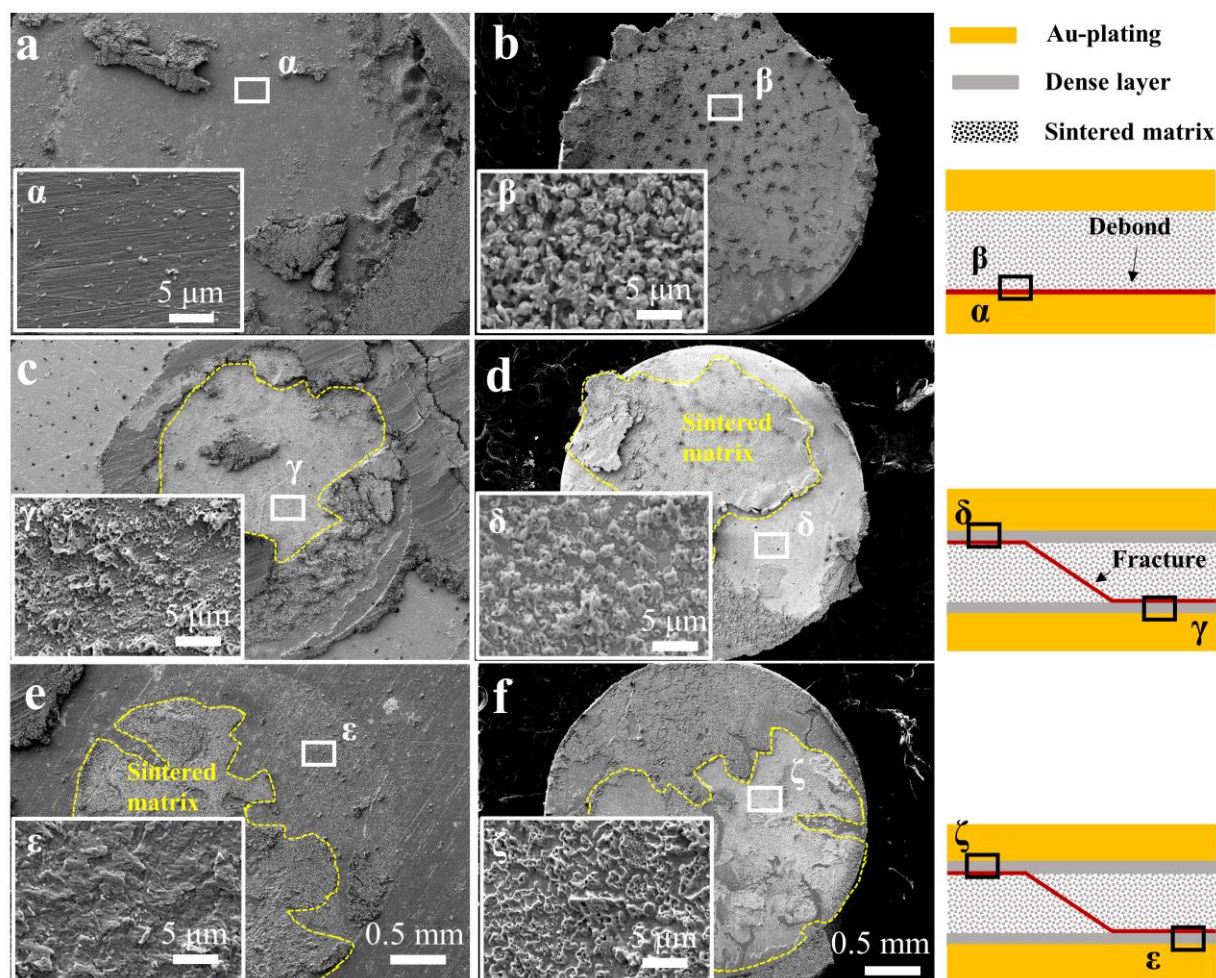


Figure 3.14 SEM images showing fracture positions of the joints assembled at 300 °C by (a, b) the non-ultrasonic process and the ultrasonic process with an ultrasonic power of (c, d) 3 W and (e, f) 8 W.

consolidation. The increases in ultrasonic time and power within a certain range enhances sintered joints via promoting such plastic deformation. Additionally, ultrasonic vibration also brings two effects: localized high temperature and acoustic softening.

The high localized temperature has been reported to occur between particles affected by ultrasonic vibration. The high-frequency forced vibration of particles causes interfacial sliding, generating high localized temperature which affects strain and yield strength of particles [4, 5]; namely, the localized high temperature conduce to thermal softening, promoting deformation of the Ag microparticles. Due to the high conductivity of the ENIG disk, the heat generated by interfacial sliding could spread quickly to the entire specimen to raise its overall temperature. This explains the higher actual temperature of the specimen during the ultrasonic processes (**Figure 3.4**). Moreover, acoustic softening effect, which affects both bulk and powder materials, promotes the migration and multiplication of the dislocation motion, consequently lead a stress reduction during deformation [6-8]. When the ultrasonic vibration is applied to the Ag microparticles, the internal atoms are activated, thus generated more relative motion; as a result, the overall dynamic deformation resistance is reduced [9]. In summary, localized high temperature and acoustic softening decrease yield strength of the Ag microparticles, and thus induce radical plastic deformation. Both effects positively relate to vibration frequency and amplitude [4].

According to the above discussion, the formation of the micro bridges and dense layers could be readily explained. We considered the bonding process as a consecutive annealing process of the microparticles. Owing to the bonding temperatures being higher than the recrystallization temperature of Ag (200 °C), the occurrence of recrystallization is reasonable. During recrystallization, new nuclei, such as deformation twin and interfacial grain boundary, are frequently formed at the regions with high strain energy. The surface of each Ag microparticle can be regarded as the grain boundary of each micro-grain. When these micro-grains are tightly contacted and severely deformed, the recrystallization across their interfaces is readily driven by the diffusion and deformation. Because most stress and strain concentrate on the needle interfaces, the needles quickly transform into the micro bridges. With the ultrasonic assistant, the acoustic softening effect accelerated the recrystallization process to form better bonding morphologies (numerous micro bridges and grain growth). Consequently, although the non-ultrasonic process is a feasible way to assemble joints because the pressure of 7 MPa has caused some needles to slightly deform and recrystallize. but the limited number of micro bridges results in compromised strength (**Figure 3.6 a, f**). On the other hand, the ultrasonic vibration with sufficient power significantly promoted the generation of plenty of micro bridges and larger grain sizes than that without the ultrasonic assistant, thus

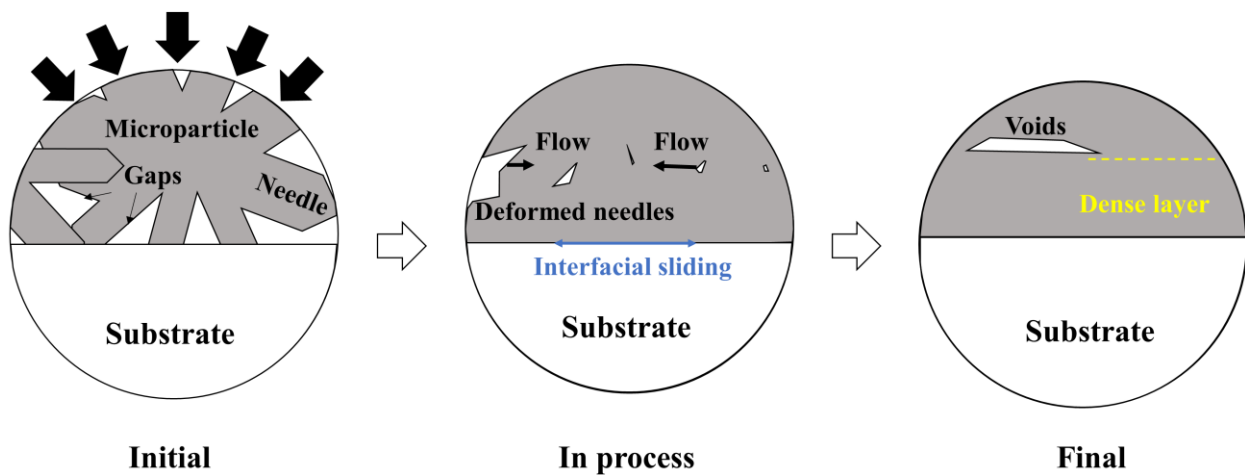


Figure 3.15 Schematic diagram illustrating the formation of dense layers in the ultrasonic process.

strengthening the Ag-sintered joints. With limited power (e.g. 1 W), however, the ultrasonic vibration fails effectively induce extra deformation but rather break the micro bridges (**Figure 3.7 a**); thus, the bonding shear strength decreased.

The formation of the dense layer is caused by deformation and consolidation of the Ag microparticles, as shown in **Figure 3.15**. At first, gaps exist between needles and cause partial contact of the microparticles on the substrate. With applying pressure, the needles bear increasing plastic deformation past the yield strength leading to higher densification due to relatively high shear stress concentrating at bonding interfaces. The densification of the microstructures causes separation and shrinkage of gaps, transforming them into voids. Due to acoustic softening effect and localized high temperature induced by the ultrasonic vibration, the mass flow and deformation are promoted, forcing tiny voids to flow and aggregate to form large voids, resulting in the formation of consolidated microstructures at the interfaces. Then the consolidated deformed microstructures recrystallize to generate a dense layer composite of equiaxed grains. Therefore, the thickness of the dense layer increases with increasing ultrasonic time and power. Since both the micro bridges and dense layers form because of recrystallization induced by deformation, it is reasonable that deformation twins exist in those parts that underwent radical deformation and strong stress [10].

However, more micro bridges did not consistently increase the shear strength of the joints because the bonding interface was normally the weakest part. According to **Figure 3.14**, the joints failed mainly at interfaces rather than within the sintered matrix; therefore, the enhancement of the micro bridges in the bond strength of the Ag-sintered joint was limited. Conversely, the formation of the dense layer at the interfaces changed fracture mode from a brittle fracture, at sintered matrix/substrate interfaces, to a ductile fracture, at dense layer/sintered matrix interfaces. The strengthening enhancement by the dense layer

formation was more significant than that by more and more micro bridge formations.

Wang et al. reported that similar dense layers appeared after sintering Ag nanoparticles at 275 °C for 30 min [11]. They found voids and delamination occurred at the dense layer/ENIG interfaces because excessive Ag atoms diffused into Au-plating layers. In this study, although the diffusion of Ag into the plating layer was observed in EPMA, no such degradation occurred; this is presumably because the dense layers formed with plastic deformation that fill possible vacancies, and the rapid process of 300 s leaves little time for atom diffusion. Whether such degradation will occur in thermal aging will be investigated in *Chapter 5*. The findings demonstrate the ultrasonic vibration is a suitable assisting energy to assemble a thermal bonding at low temperatures, and its enhancing mechanism and optimization are revealed for not only Ag microparticles but also Cu microparticles.

3.4 Conclusions

With low-power ultrasonic vibration, Ag-sintered joints were fabricated on ENIG disks. It proves the feasibility of application in thermal-compression bonding methods. Robust Ag-joints with an average shear strength of 36.2 MPa was obtained in 300 s at a pressure of 7 MPa and an ultrasonic power of 8 W; this was twice as high as joints obtained through the non-ultrasonic process. The influences of the ultrasonic time and ultrasonic power on the quality of joints and the sintered microstructures were investigated. Based on that, the bonding and strengthening mechanisms of ultrasonic vibration were revealed. The main conclusions are addressed as follow:

1. Ultrasonic vibration can induce localized high temperatures and acoustic softening effect. Both effects soften materials, thereby promote plastic deformation and densification of the Ag microparticles.
2. The micro bridges are transformed from the needles due to recrystallization driven by severe plastic deformation. Only with the ultrasonic vibration do the dense layers form at the bonding interfaces.
3. The micro bridges provide good bonding between Ag microparticles, and the dense layer strengthens the Ag-sintered joints via eliminating brittle interfacial debonding. The ultrasonic-assisted bonding method is able to assemble reliable Ag-sintered joints with rich micro bridges and dense layers at bonding interfaces.

Reference

1. Nishikawa, H., X. Liu, X. Wang, A. Fujita, N. Kamada, and M. Saito, Microscale Ag particle paste for sintered joints in high-power devices. *Materials Letters*, **161** (2015) 231-233.
2. Luechinger, N.A., E.K. Athanassiou, and W.J. Stark, Graphene-stabilized copper nanoparticles as an air-stable substitute for silver and gold in low-cost ink-jet printable electronics. *Nanotechnology*, **19** (2008) 445201.
3. Hu, J., T. Shimizu, T. Yoshino, T. Shiratori, and M. Yang, Evolution of acoustic softening effect on ultrasonic-assisted micro/meso-compression behavior and microstructure. *Ultrasonics*, (2020) 106107.
4. James, S. and P. Rajanna, Molecular dynamics simulation study of ultrasonic powder consolidation process, ASME 2018 13th International Manufacturing Science and Engineering Conference, (2018) V004T03A026.
5. Bhavsar, S. and S. James, Thermo-mechanical finite element analysis of ultrasonic powder consolidation process. *Additive Manufacturing*, **21** (2018) 705-712.
6. Chen, K., Y. Zhang, and H. Wang, Effect of acoustic softening on the thermal-mechanical process of ultrasonic welding. *Ultrasonics*, **75** (2017) 9-21.
7. Zhao, X., S. Zhao, and Q. Han, Effects of vibration direction on the mechanical behavior and microstructure of a metal sheet undergoing vibration-assisted uniaxial tension. *Materials Science and Engineering: A*, **743** (2019) 472-481.
8. Yao, Z., G.-Y. Kim, L. Faidley, Q. Zou, D. Mei, and Z. Chen, Micro pin extrusion of metallic materials assisted by ultrasonic vibration, International Manufacturing Science and Engineering Conference, (2010) 647-651.
9. Wang, C., Y. Liu, B. Guo, D. Shan, and B. Zhang, Acoustic softening and stress superposition in ultrasonic vibration assisted uniaxial tension of copper foil: experiments and modeling. *Materials & Design*, **112** (2016) 246-253.
10. Gutkin, M.Y., *Elastic and plastic deformation in nanocrystalline metals*, in *Nanostructured Metals and Alloys*, Elsevier (2011) 329-374.
11. Wang, X., Y. Mei, X. Li, M. Wang, Z. Cui, and G.-Q. Lu, Pressureless sintering of nanosilver paste as die attachment on substrates with ENIG finish for semiconductor applications. *Journal of Alloys and Compounds*, **777** (2019) 578-585.

Chapter 4

Ultrasonic-assisted bonding process using organic-protected Cu microparticles

4.1 Introduction

In *Chapter 2*, the feasibility and efficiency of the bonding process that sinters preoxidized Cu microparticles in a formic acid atmosphere have been proven. In *Chapter 3*, we successfully develop a rapid low-power ultrasonic-assisted bonding method for the Ag chestnuts-burr-like microparticles, and revealed the effects of ultrasonic vibration on the transformation of metallic microparticles and sintering. In this chapter, based on the study in chapter 2 and 3, an attempt was made to integrate the reduction reactive reaction with ultrasonic assistance for promoting the sintering of Cu microparticles at low temperature in air to assemble Cu/Cu joints in the air. On the one hand, the Cu microparticles are expected to be protected from oxidation during bonding process by the reductive agents, thus hindering oxides formation. Besides, the ultrasonic vibration is supposed to promote sintering, achieving joints with relatively lower temperatures. Main parameters used in the procedure with respect to the result of effects

were firstly analyzed in this study. Subsequently, joints assembled with optimized parameters under different pressure were examined to explore the effects of ultrasonic vibration on the evolution of sintered microstructures. Based on the above results, the bonding and reinforcing mechanisms were researched.

4.2 Experimental

4.2.1 Sample fabrication

Spherical Cu microparticles (hereinafter referred to as the microparticles in this chapter) with an average diameter of $4.2\ \mu\text{m}$ (1400Y, Mitsui Mining & Smelting Co., Ltd.) were used as filler materials, as shown in **Figure 4.1 a**. Different organic solvents and reductive agents, which protect Cu from oxidation during the processes, were compared. The organic solvents and reducing agents were mixed and stirred at $50\ ^\circ\text{C}$, and the supernatant was taken after the solution cool down. The mixed solution then was mixed with the microparticles in the 85/15 wt.%/wt.% ratio to fabricate paste. A schematic diagram of paste fabrication is illustrated in **Figure 4.1 a**. The same oxygen-free Cu cylindrical disks (upper and bottom disks) used in *Chapter 2* and *Chapter 3* were used to assemble joint specimens: They were cleaned ultrasonically in dilute hydrochloric acid (4%) and rinsed with ethanol, then the paste was stencil-printed on the surface of the bottom disk layer with a thickness of $150\ \mu\text{m}$. and the upper disk was mounted on the as-printed paste. The modified thermal pressure bonding machine (HTB - MM, Alpha Design Co.,

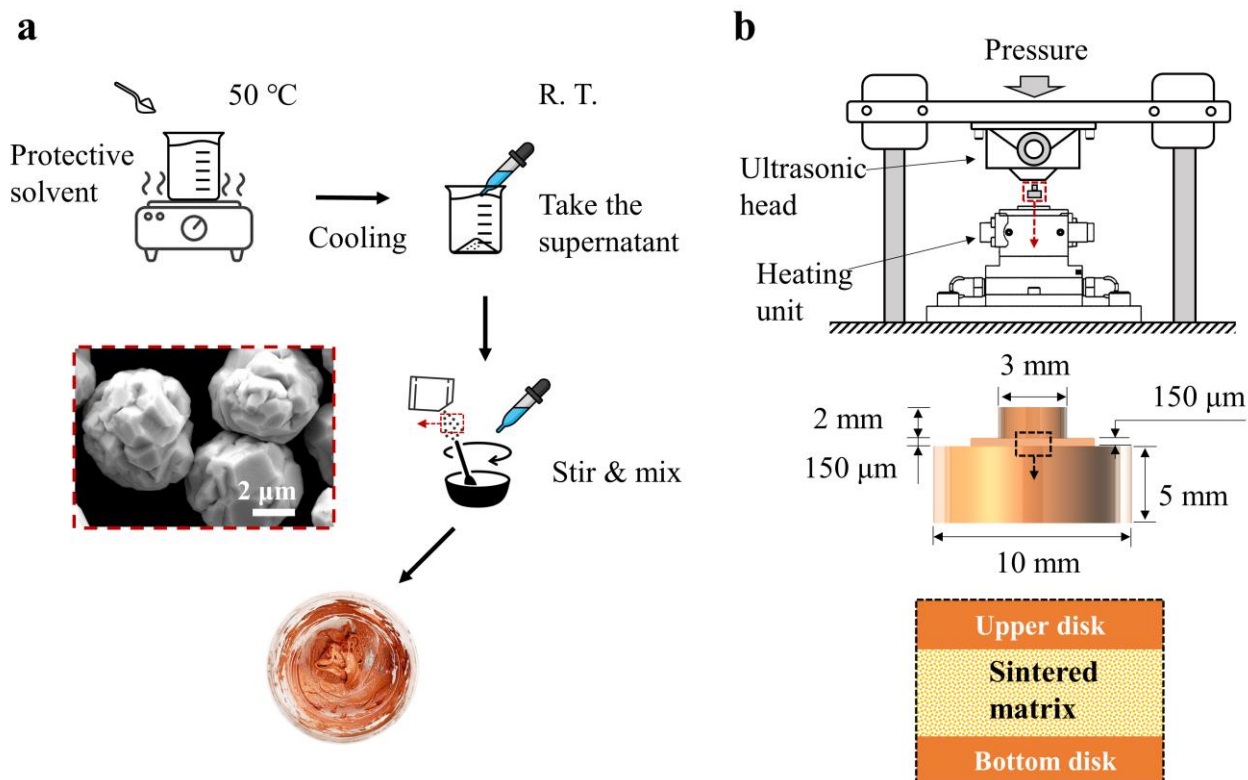


Figure 4.1 Schematic diagram of (a) the paste fabrication and (b) the joint specimen. (R. T.: room temperature).

Ltd) attaching an ultrasonic head (horn) and an ultrasonic generator was used to assemble bonding with ultrasonic assistance, and details of the bonding device are illustrated in *Chapter 2*. The pressures were applied by the ultrasonic head and were determined to be 7 MPa (50 N) and 14 MPa (100N) for each joint specimen. The frequency of ultrasonic vibration was fixed to 50 kHz, and the ultrasonic vibration amplitude was fixed to 5 μm to maintain a low ultrasonic power; consequently, when the applied pressure is 7 MPa and 14 MPa, the representative ultrasonic power is 8 W and 16 W, respectively. A schematic diagram of joint fabrication is illustrated in **Figure 4.1 b**. A thermocouple was attached to the side of the bottom disk, the same position in *Chapter 2*, to measure the real-time temperature of specimens during heating. The heating unit and the ultrasonic head that applies pressure and ultrasonic vibration are independent modules; the heating unit was increased directly to bonding temperature at a rate of 12 $^{\circ}\text{C}/\text{s}$ without preheating, then held at that temperature until the end of the process. The pressure was applied at beginning of the process, and the ultrasonic vibration was applied when the heater reached the bonding temperature. As the bonding condition including protective solvents, setting temperature, total process time, and ultrasonic time, yet their effects on sintering of the Cu microparticles are still unclear. Therefore, these parameters will be tested and discussed separately, and an optimized profile will be given later.

4.2.2 Testing and characterization

The pastes with different protective solvents were tested by a simultaneous thermogravimetric analyzer (STA7200, Hitachi) to investigate their thermal properties and phase transformation at different temperatures. The bonded joint specimens were tested by a shear tester (STR-1000, Rhesca) to evaluate their bonding strength. The average shear strength of the joints assembled under different conditions was determined by 3 specimens; all original shear strength of the joints was plotted. After the shear tests, upper disks and bottom disks were used to observe their fracture surfaces. Additionally, the cross-section samples were polished using a cross-section polisher (SM-09010, JEOL) with ion milling to prevent the microparticles from deformation and smearing into the pores by mechanical grinding and polishing, which makes it difficult to evaluate the quality of sintered microstructures. Both the fracture surfaces and cross-sectional samples were characterized by a field emission scanning electron microscopy (FESEM; SU-70, Hitachi). A focused ion beam (FIB; JIB-4500, JEOL) equipped SEM was used to observe sintered microstructures and prepare samples for the transmission electron microscope (TEM; JEM-2100, JEOL).

Table 4.1 Solvents and reductive agents used for the bonding process using Cu in the air atmosphere [1-8].

Bonding material	Solvent	Reduce agent	Bonding temp.	Reference
Cu nanoparticles	Glycol	-	280-400°C	[1]
Cu nanoparticles	Ethylene glycol	Isopropanol (l)	250-275°C	[2]
Cu nanoparticles	Ethylene glycol	L-ascorbic & PVP (s)	250-350°C	[3]
Cu nanoparticles	Glycerol	Glycerol (l)	220°C	[4]
Cu ₂ O nanoparticles	-	Formic acid (g)	200-800°C	[6]
CuO microparticles	PEG1000	PEG1000 (l)	320°C	[5]
Cu microparticles	α -Terpineol	Formic acid (g)	300°C	[7]
Cu-Ag nanoparticles	α -Terpineol	-	350°C	[8]
Cu microparticles	Glycerol	L-ascorbic acid (s)	240°C	This study

4.3 Results and discussion

4.3.1 Protective solvent and bonding parameters

During the bonding procedure, the formed oxides are barriers to the metallic atom's diffusion and will prevent the formation of sintering necks. Furthermore, the fragile oxides intercalate between particles after sintering, consequently yielding joints with inferior conductivity and reliability. Hence, bonding processes based on the sintering of Cu microscale and nanoscale particles require measures for preventing particles from oxidation. The bonding processes operated in the air normally utilize certain organic reductive solvents for suppressing oxide formation. **Table 4.1** lists certain protective solvents and reducing agents utilized for bonding processes using Cu materials in the air.

In this study, our process was operated in a non-confined chamber with air atmosphere; therefore, the protective solvent and reducing agent should meet the following three conditions:

1. It is not harmful to relationship between living things and their environments; it does not produce any toxic effect in the body of human beings.
2. It is capable of hindering Cu from oxidation at room temperature and at the bonding temperatures it reduces the formation of oxides.
3. In order to avoid residues that affect bonding quality, it is capable of being decomposed at the bonding temperatures

In accordance with the above discussion, L-ascorbic acid was chosen as the reducing agent. L-ascorbic

acid exhibits sufficient reducibility for converting Cu(II) into Cu(0) because the electrons in the double bond, hydroxyl group lone pair, and the lactone ring carbonyl double bond form a conjugated system; the redox equation of the L-ascorbic [9]. Moreover, its decomposition products are gaseous (H_2O , CO_2 , CO , HCOOH , and CH_4) that could easily escape from the sintered matrix [10]. Glycerol was selected as the protective solvent, due to the relatively high solubility for L-ascorbic acid (10g/L) [11], as well as the reducibility to copper oxides [9]. Therefore, glycerol not only coats microparticles to protect paste from oxidation at room temperatures but likewise assists reduction during the bonding processes prior to completion of evaporation and decomposition.

Figure 4.2 shows the shear strength of joints assembled at 240 °C (setting temperature) for 5 min, under a pressure of 7 MPa, with various protective solvent systems. α -Terpineol, as a high boil point organic solvent that does not react with other ingredients, was applied as a comparison in this experiment. Using terpineol, joints assembled from the non-ultrasonic process give an average shear strength of ~15 MPa, whereas ultrasonic vibration causes a decline in the average shear strength to ~4 MPa. However, L-ascorbic acid addition in terpineol (1g/L, saturated) gives the average shear strength yield from the non-ultrasonic process decline to just 5 MPa, whereas ultrasonic vibration does improve shear strength to 12 MPa. When glycerol was used as the protective solvent without other ingredients, shear strength got through the ultrasonic process (14 MPa) is far higher than that obtained by the non-ultrasonic process (6 MPa). When L-ascorbic acid (10g/L, saturated) is a component of glycerol, the average shear strength of joints assembled with the non-ultrasonic process and the ultrasonic process increased to 7 MPa and 15 MPa, respectively.

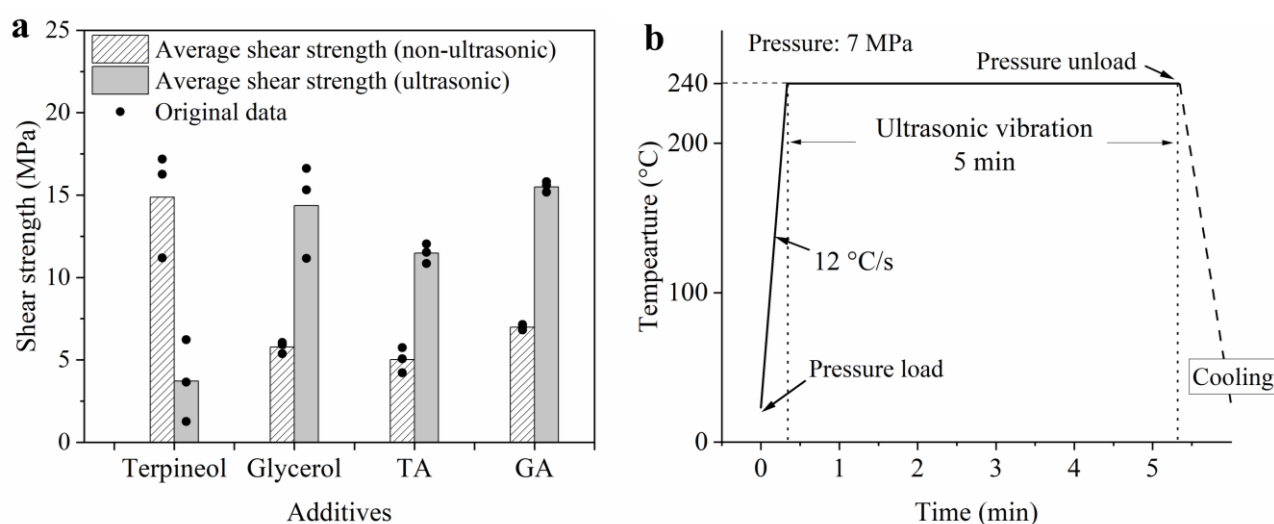


Figure 4.2 Influence of protective solvents on shear strength of joints: (a) shear strength of joints assembled using different protective solvents, and (b) heating profile used to prepare joints for this solvent test. (TA: α -Terpineol + L-ascorbic acid; GA: glycerol + L-ascorbic acid).

When terpineol was exclusively used, the microparticles underwent rapid oxidation after completion of solvent evaporation; thus, the formed Cu oxide between the microparticles bonded them together to provide a shear strength of ~ 15 MPa, which is not significantly affected by bonding temperature and process time [12]. The bonding assembled by oxide is brittle and is readily broken; therefore, the shear strength was reduced upon the application of the ultrasonic vibration. Contrarily, with the inclusion of reductive organic reagents, such as L-ascorbic acid and glycerol, which suppressed the formation of the oxide, the microparticles failed to bond by the oxide, hence the inferior shear strength obtained through the non-ultrasonic process. Less formation of oxide, subsequently, enables direct contact of metals, thus the ultrasonic vibration could impact and promote metallic sintering. As a result, there is a significant increase in the shear strength achieved through the ultrasonic process. Despite the similarity in reducibility shown through the glycerol to Cu oxides as L-ascorbic acid behaves, using additive L-ascorbic acid as a vital ingredient that is capable of impeding oxidation in a continuous order following the evaporation of the glycerol as a result of the decomposition temperature of precipitated solid L-ascorbic acid at about $300\text{ }^{\circ}\text{C}$ [13]). Thus, L-ascorbic acid in glycerol (10 g/L) was chosen as a protective solvent to mix with the Cu microparticles in the 85/15 wt.%/wt.% ratio to prepare the filling paste.

Figure 4.3 depicts the DSC and TG curves of the as-fabricated paste with the temperature increasing from 20 to $500\text{ }^{\circ}\text{C}$ at a rate of $20\text{ }^{\circ}\text{C}/\text{min}$ in the air. It is observed that the weight started reducing at $110\text{ }^{\circ}\text{C}$

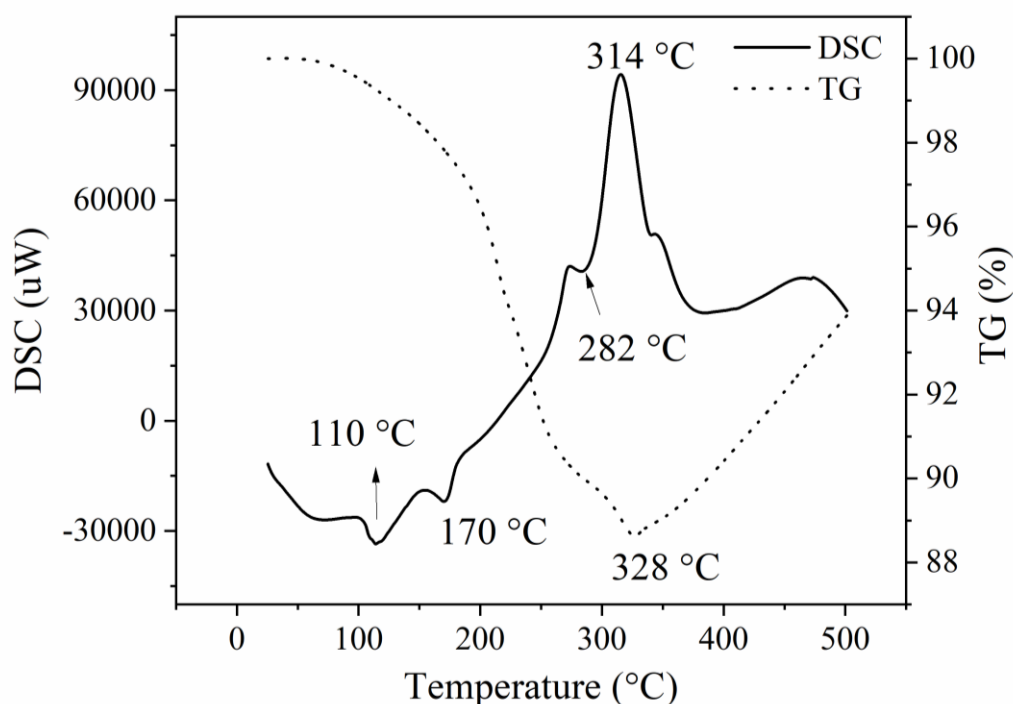


Figure 4.3 DSC and TG curves of the as-fabricated paste with temperature rising from $20 - 500\text{ }^{\circ}\text{C}$ at a rate of $20\text{ }^{\circ}\text{C}/\text{min}$ in the air.

with an endothermic peak, which obviously resulted from the evaporation of the glycerol. When the temperature attained 170 °C, the weight loss became considerable, and a second endothermic peak appeared; this was due to the decomposition of L-ascorbic acid [13]. When the temperature reached 282 °C, which is closed to the boiling point of the glycerol (290 °C [14]), the third endothermic peak appeared with the TG curve steadily declining. When the temperature rose to 328 °C, an exothermic peak appeared with the TG curves turning to arise, revealing severe oxidation of the microparticles that occurred after completing the decomposition of the L-ascorbic acid. Based on the above results, the bonding temperature was determined to be 200 °C, at which the oxidation of the Cu microparticles was still impeded, meanwhile the glycerol and L-ascorbic acid capable of evaporating and decomposing efficiently to reduce residues.

DSC tests were conducted in the air or N₂ at a fixed temperature of 200 °C, and the results of the pastes with or without L-ascorbic acid are revealed in **Figure 4.4**. In N₂ atmosphere, the pastes with **(Figure 4.4 a)** and without **(Figure 4.4 b)** the L-ascorbic acid depict a similar thermal behavior: after the first endothermic peak denoting complete evaporation of the glycerol in 3 min, no obvious

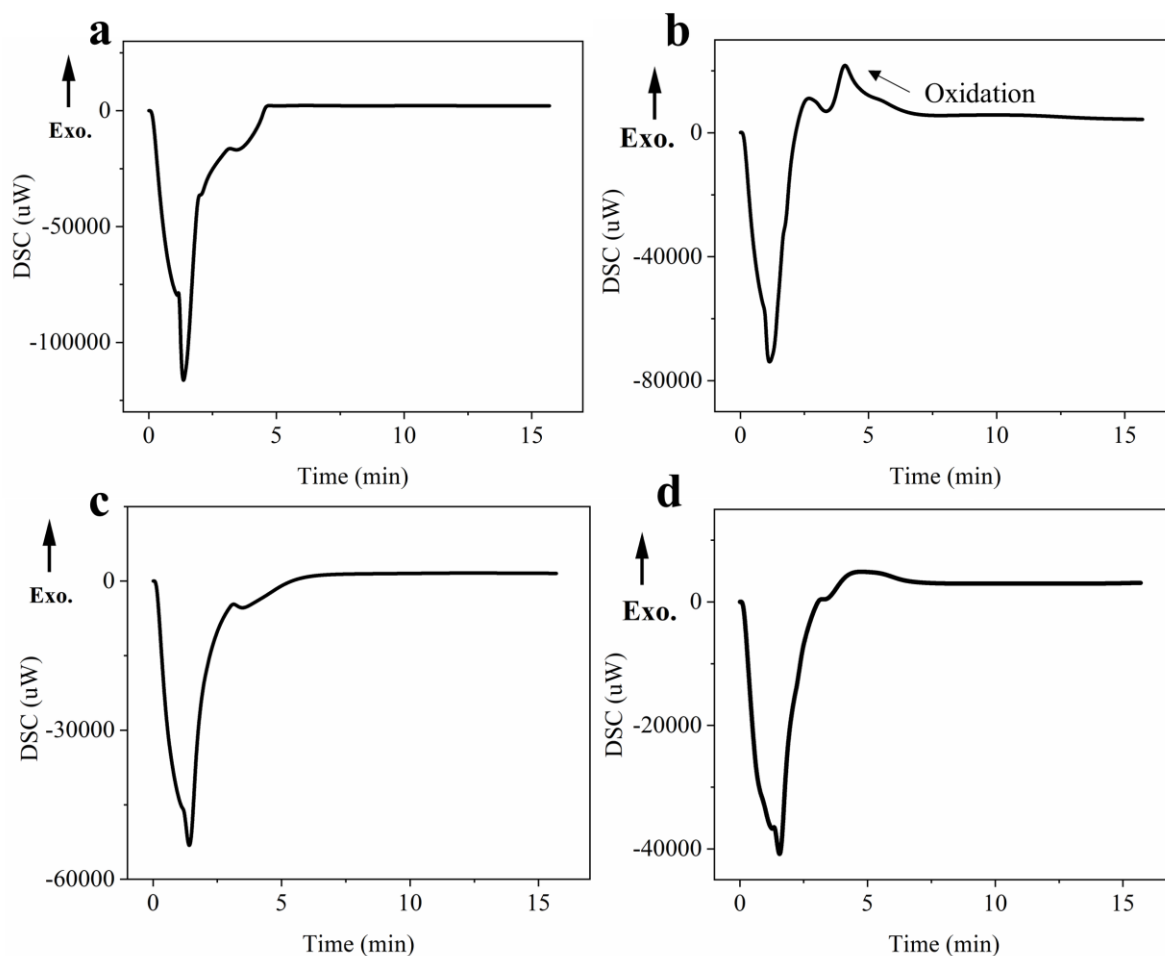


Figure 4.4 DSC curves of the pastes with different protective solvents in the air or N₂ atmosphere at a fixed temperature of 200 °C: (a) glycerol + N₂, (b) glycerol + air, (c) L-ascorbic acid and glycerol + N₂, and (d) L-ascorbic acid and glycerol + air.

thermodynamic changes was noted. Nevertheless, a different pattern is observed on the DSC curve from the paste including or excluding L-ascorbic acid in the air. In 4 min, lateral appears an exothermic peak (**Figure 4.4 b**) which shows oxidation of the Cu microparticles, proving that the oxidation of Cu is effectively prevented by additive L-ascorbic acid.

On the account of the determined protective solvent and bonding temperature, the total process time, which represents the total heating time at bonding temperature, was then optimized. The joint specimens were assembled by sintering the Cu microparticles at a setting temperature of 240 °C and a pressure of 14 MPa for various time intervals (5 min, 10 min, 15 min, and 20 min), ultrasonic vibration spread across the whole bonding process. Shear strength of the joints assembled for different time is shown in **Figure 4.5 a**. The non-ultrasonic process, which achieves bonding through interdiffusion driven by thermocompression, assembled joints with shear strength below 22 MPa, and the shear strength slightly increased first then decreased with extension of the process. With a long sufficient process time (10 min

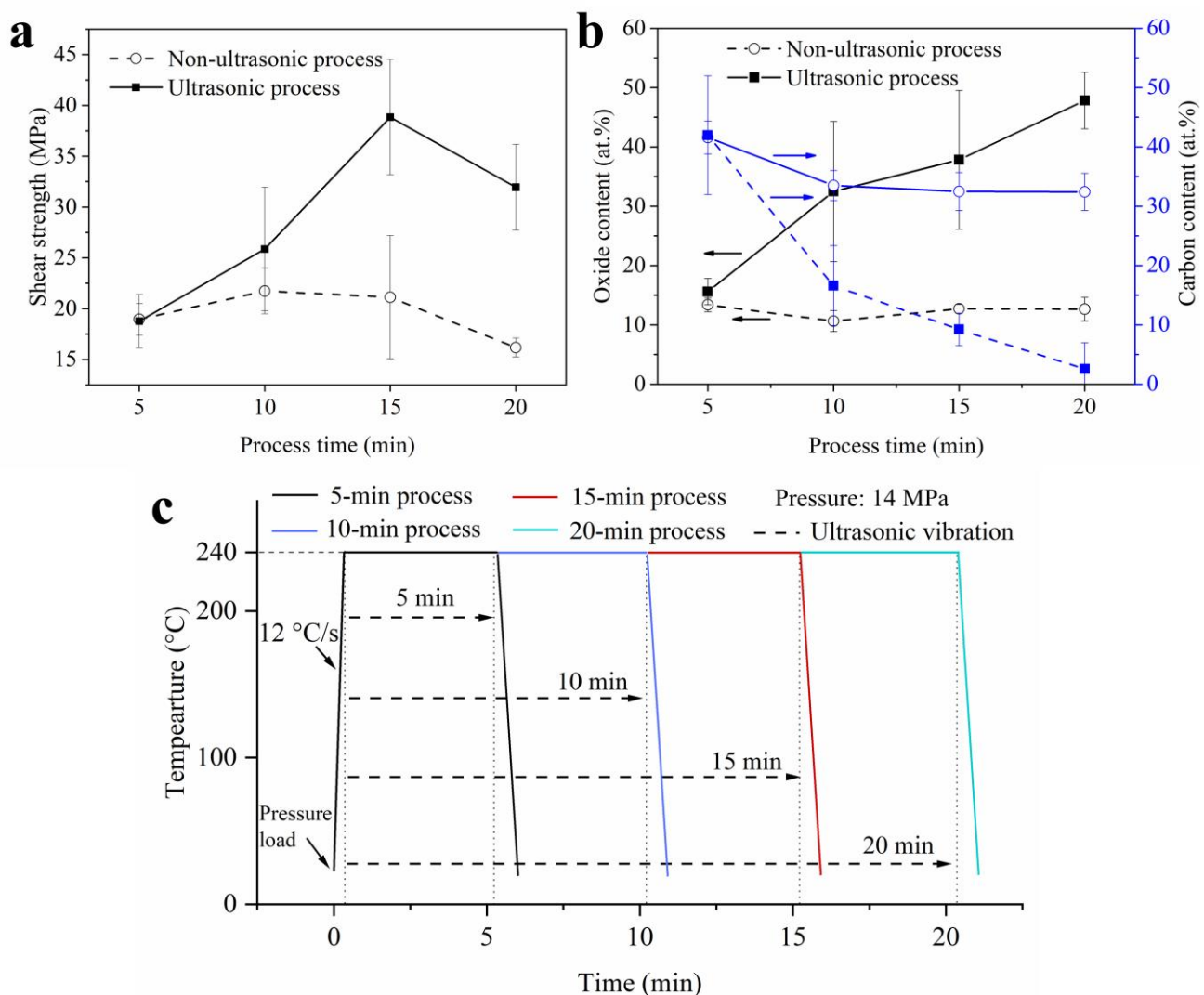


Figure 4.5 Influence of total process time on (a) shear strength and (b) oxide and carbon content of the joints, and (c) profile used to prepare joints for this trial.

and above), ultrasonic vibration significantly increased the shear strength; when the process time was 10 and 15 min, the shear strength attained 25 and 39 MPa, respectively. Notwithstanding, when the process time further extended to 20 min, joint shear strength decreased to 31 MPa.

To investigate such behavior in joint shear strength that was affected by the total process time, we examined each specimen's fracture surface after shear test by EDS, and the average oxygen and carbon contents are determined by three samples, as revealed in **Figure 4.5 b**. The oxidation degree of the sintered matrix was estimated by oxygen content, and the organic residues, particularly L-ascorbic acid residues, were assessed by carbon content. It should be pointed out that the fractures occurred through debonding between the microparticles, and the EDS mainly detected the particle surface, where the oxides and residual organics are mainly enriched. Therefore, the EDS results obtained from fracture surfaces should be solely utilized for comparative evaluation and would be much different from the actual contents. Evidently, both the oxygen content (~15 at.%), and the carbon content (30 at.%) hardly changed in joints obtained through the extension of the non-ultrasonic process. Nevertheless, with the application of ultrasonic vibration, there is a continuous increase in the oxygen content and reached ~50 at.% when the process extended to 20 min; contrastingly, after 20 min, carbon content continuously reduced and was nearly totally consumed.

The stable oxygen and carbon contents irrespective of process time in fracture surfaces of joints assembled with the non-ultrasonic process have proven the continuous anti-oxidation effect of the L-ascorbic acid on the microparticles. On the other hand, the rising oxygen content and the declining carbon content during the ultrasonic process were results of the localized high temperature caused through interfacial slip (as discussed in *Chapter 3*), which promotes the decomposition of the L-ascorbic acid and oxidation of the microparticles. Therefore, the total process time was optimized to 15 min for better reliability, fewer oxides, as well as fewer organic residues.

The ultrasonic time means application time of ultrasonic vibration in the course of heating the specimens, and its maximum value does not exceed the total process time. As could be seen from *Chapter 3*, ultrasonic vibration possess a specific threshold to enhance the joint shear strength; it is necessary to optimize the ultrasonic time from view of efficiency and joint reliability. Therefore, through the use of the protective solvent, the process time, and the bonding temperature which are the parameters stated above, and by application of different pressures of 7 MPa and 14 MPa, the relationship between ultrasonic time and joint shear strength is illustrated in **Figure 4.6**. It is readily observed that regardless of the applied pressure, the joint's shear strength rose with increasing ultrasonic time when the ultrasonic time

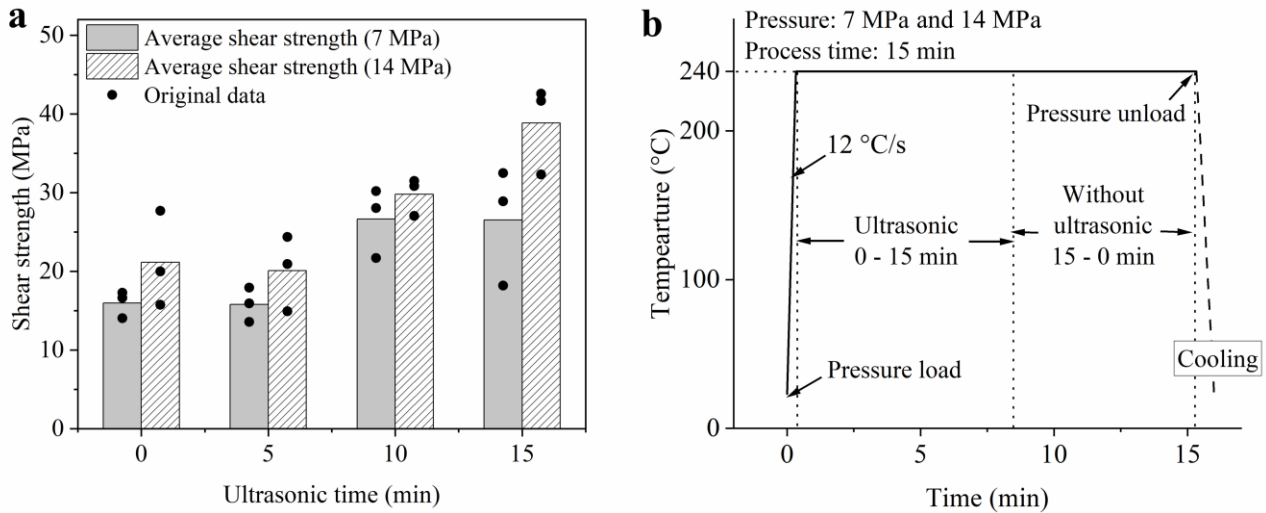


Figure 4.6 Influence of ultrasonic time and pressure on the joints: (a) Shear strength of the joints assembled with different ultrasonic time and pressure, and (b) heating profile used to prepare joints for this test.

exceeded 5 min. Under the pressure of 7 MPa, the shear strength reached the maximum value of 27 MPa when the ultrasonic time was 10 min and stopped rising. When the pressure increased to 14 MPa, the joint shear strength obtained with an ultrasonic time of 10 min increased to 30 MPa, which is higher than that achieved under 7 MPa. Furthermore, the maximum shear strength increased to 39 MPa, which was obtained when the ultrasonic time was 15 min. Summarily, the increasing pressure not only increased the shear strength of joints assembled under similar conditions but likewise enhanced the threshold of ultrasonic strengthening on the joint. The ultrasonic time for joints assembled under the pressures of 7 MPa and 14 MPa was determined to be 10 min and 15 min, respectively.

Summarily, the protective solvent chosen is glycerol containing L-ascorbic acid (10 g/L, saturated), which was mixed with the microparticles to prepare the filling paste. The joint specimens were heated at

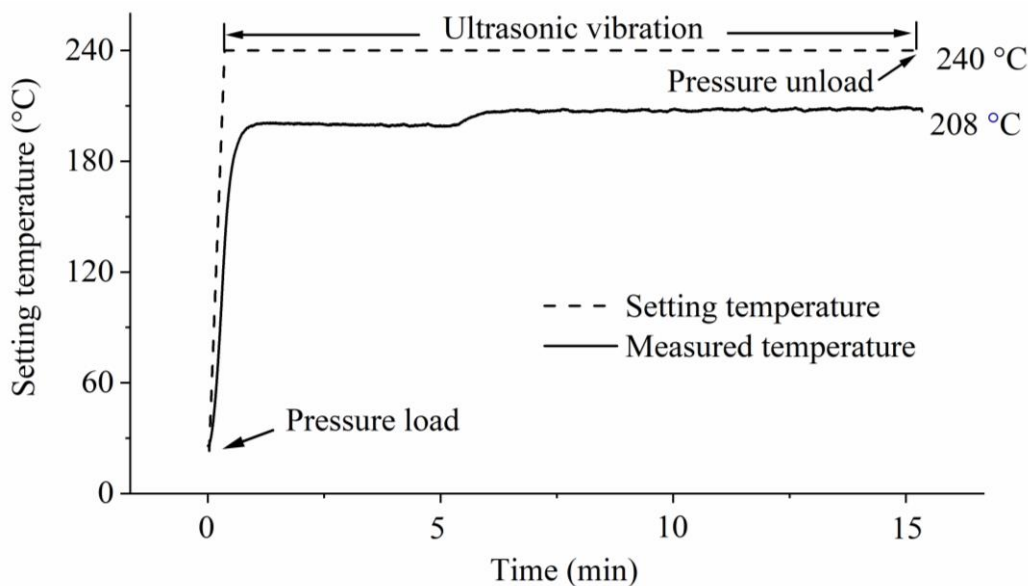


Figure 4.7 Optimized profile of the process and the measured actual temperature of the joint specimen during heating without ultrasonic vibration.

240 °C for 15 min, during which pressures and ultrasonic vibration were applied to assemble Cu/Cu joints rapidly at low temperature (the optimized profile in this study is shown in **Figure 4.7**).

4.3.2 Microstructures of joints assembled with ultrasonic-assisted bonding

Fracture surfaces of joints assembled under pressures of 7 MPa and 14 MPa by the non-ultrasonic and the ultrasonic processes are depicted in **Figure 4.8**. Following the non-ultrasonic process, regardless of the applied pressure, the microparticles barely deformed due to their high yield strength (33 MPa [15]). On the Basis of the observation in fracture surfaces (**Figure 4.8 a and c**), it is adjudged that there is no formation of firm bond between the sintered matrix and the Cu substrates, since the attachment of the sintered matrix is mainly to one side, and a bare surface is exhibited by the corresponding area of another side. Thus, the failure mode of the joints obtained by the non-ultrasonic process is brittle interfacial detachment, owing to the weak bond between the sintered matrix and substrates. Contrastingly, fractography significantly changed when the ultrasonic vibration was applied, as depicted in **Figure 4.8**

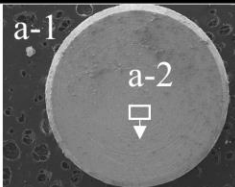
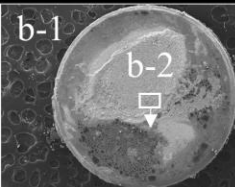
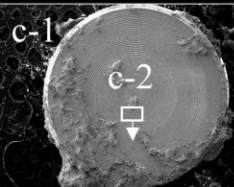
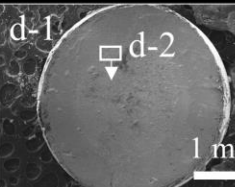
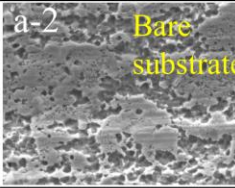
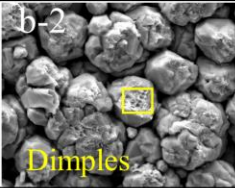
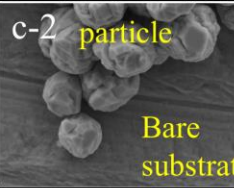
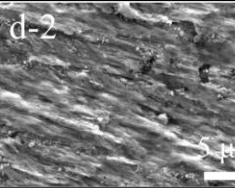
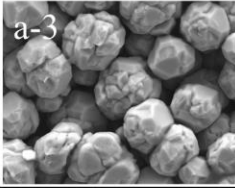
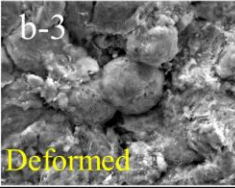
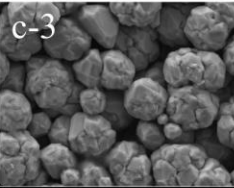
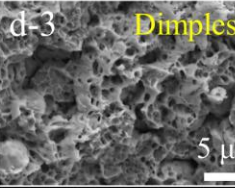
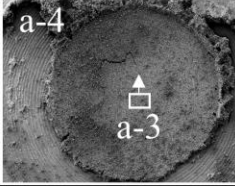
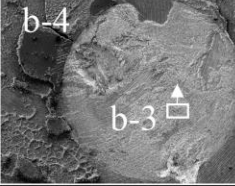
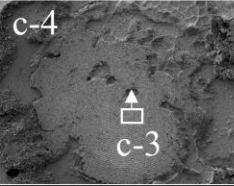
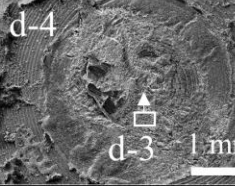
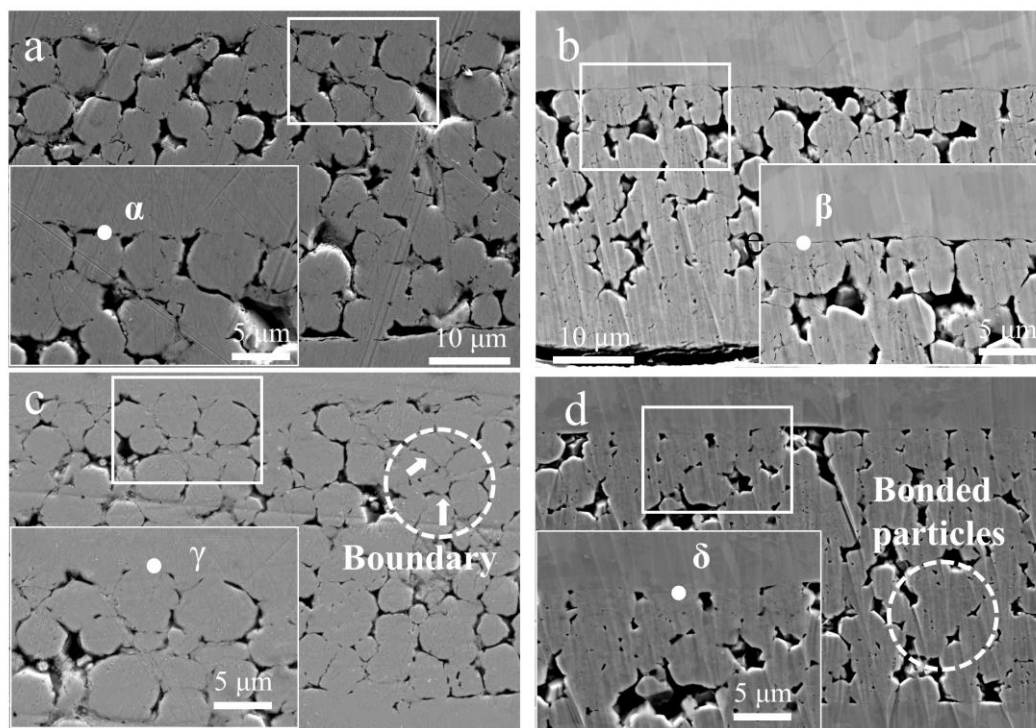
	7 MPa Non-US	7 MPa US	14 MPa Non-US	14 MPa US
Upper side	a-1 	b-1 	c-1 	d-1 
Upper side	a-2  Bare substrate	b-2  Dimples	c-2  particle Bare substrate	d-2  5 μm
Bottom side	a-3 	b-3  Deformed	c-3 	d-3  Dimples 5 μm
Bottom side	a-4 	b-4 	c-4 	d-4  1 mm
Shear strength	16.62 MPa	30.17 MPa	15.73 MPa	42.55 MPa

Figure 4.8 Fracture surfaces of joints assembled under a pressure of 7 MPa by (a) non-ultrasonic process and (b) by ultrasonic process, and under a pressure of 14 MPa by (c) non-ultrasonic process and (d) by ultrasonic process. (US: ultrasonic vibration).

b and **d**. Firstly, the microparticles significantly deformed, revealing the densification of the bonding matrix. Furthermore, following the shearing, there is an attachment of the sintered matrix to both sides, and observation of a significant proportion of dimples was recorded. That implies that the fracture mode changed to ductile failure and occurred within the sintered matrix. The behavior in failure mode is similar to cases in *Chapter 2*.

Figure 4.9 depicts the cross-sectional images of joints assembled at 7 MPa and 11 MPa pressures respectively through the non-ultrasonic and ultrasonic process, along with the corresponding EDS results. In accordance to **Figure 4.9 a** and **c**, regardless of increasing pressure applied without ultrasonic vibration, the microparticles deformation is not glaring, and boundary lines at particle interfaces were still visible, which indicates a weak bonding between the microparticles. Additionally, the microparticles at the interfaces are embedded into the substrates; this is adjudged to adversely impact the reliability as it may cause stress concentration or crack initiation in plating metals under dies. However, with the ultrasonic



e	Image a	Image b	Image c	Image d	Point α	Point β	Point γ	Point δ
Cu (at.%)	75.39	78.93	60.87	72.84	62.29	100	71.16	91.72
O (at.%)	3.49	6.72	4.12	0	31.72	0	0	0
C (at.%)	21.12	14.3	35.01	27.16	59.8	0	28.84	8.28

Figure 4.9 Cross-sectional SEM images of joints assembled under a pressure of 7 MPa by (a) non-ultrasonic process and (b) by ultrasonic process, and under a pressure of 14 MPa by (c) non-ultrasonic process and (d) by ultrasonic process, and (e) EDS results of different regions marked in the images.

vibration applying (**Figure 4.9 b and d**), the deformation of microparticles was significantly promoted, and the microparticles bonded solidly with the absence of boundary lines at interfaces. In addition, the insertion of the microparticles into the substrates was prevented. According to the EDS results presented in **Figure 4.9 e**, the protective solvents indicate a significant effect, since oxide content detected on cross-sectional samples obtained under divers conditions was significantly low (<5 at.%). Contrastingly, carbon content, which presents the main indicator for estimating organic residues, was relatively high, revealing that the protective solvent adhering to microparticles surfaces were not totally decomposed. Overall, carbon content increased with increasing pressure; however, it decreased by ultrasonic vibration. Following the non-ultrasonic process with a pressure of 7 MPa, oxides were detected at the sintered matrix/substrate interface (**Point α**), which were speculated to be Cu_2O in accordance to its atomic ratio.

The ultrasonic vibration and the pressure synergistically affect the sintered microstructure and its components, and the two factors are not independent. The increasing pressure significantly promote deformation of the microparticles only through ultrasonic vibration, otherwise will not be able to perform such feat. Thus it means that the ultrasonic vibration remains a source of inducement of microparticle deformation, and increasing pressure promoted its efficiency, thereby given to way to larger deformation. Under the same condition, increasing pressure led to more carbon residues, since larger plastic deformation of the microparticles decreased the porosity of the sintered matrix, blocking the paths that allow organic vapor and decomposition products to escape. Additionally, the application of static pressure resulted in high stress at the contact point between the microparticles and the substrates, leading to a high-temperature creep of the substrate since the hardness of the microparticles is higher due to strain hardening; therefore the microparticles were embedded into the substrates. However, the ultrasonic vibration not only reduced carbon residues but equally prevented the insertion phenomena. The former was because interfacial slip caused by vibration resulted in the localized high temperature, which accelerated evaporation and decomposition of organic components (details have been discussed in *Chapter 2*). Additionally, flows of the microparticles and voids and creating pathways for the gas escaping as a result of the ultrasonic process forcing the microparticles to vibrate. The latter was because the forced motion of the microparticles distributed the stress evenly over the surfaces, leading to reduction of the compressive stress on the fixed point.

4.3.3 Mechanism of microparticle bonding and its reinforcement

When the microparticles were bonded tightly, voidless interfaces formed from two adjacent free surfaces without visible particle boundary (**Figure 4.9 d**). These voidless interfaces were referred to as particle bonding interfaces (PBIs) in this study. The PBIs were observed by STEM in FIB prepared cross-sectional sample obtained with the ultrasonic process under a pressure of 14 MPa. **Figure 4.10 a** shows three PBIs (marked by the white square boxes), all in various states, and their enlarged views are shown in **Figure 4.10 b-e**. At the PBI shown in **Figure 4.10 b**, an obvious film sandwiched between the two microparticles, which were considered as an oxide film since EDS line scanning (**Figure 4.10 f**) indicates an oxygen enrichment in this film. The oxide film formed during the process was reported to impede the

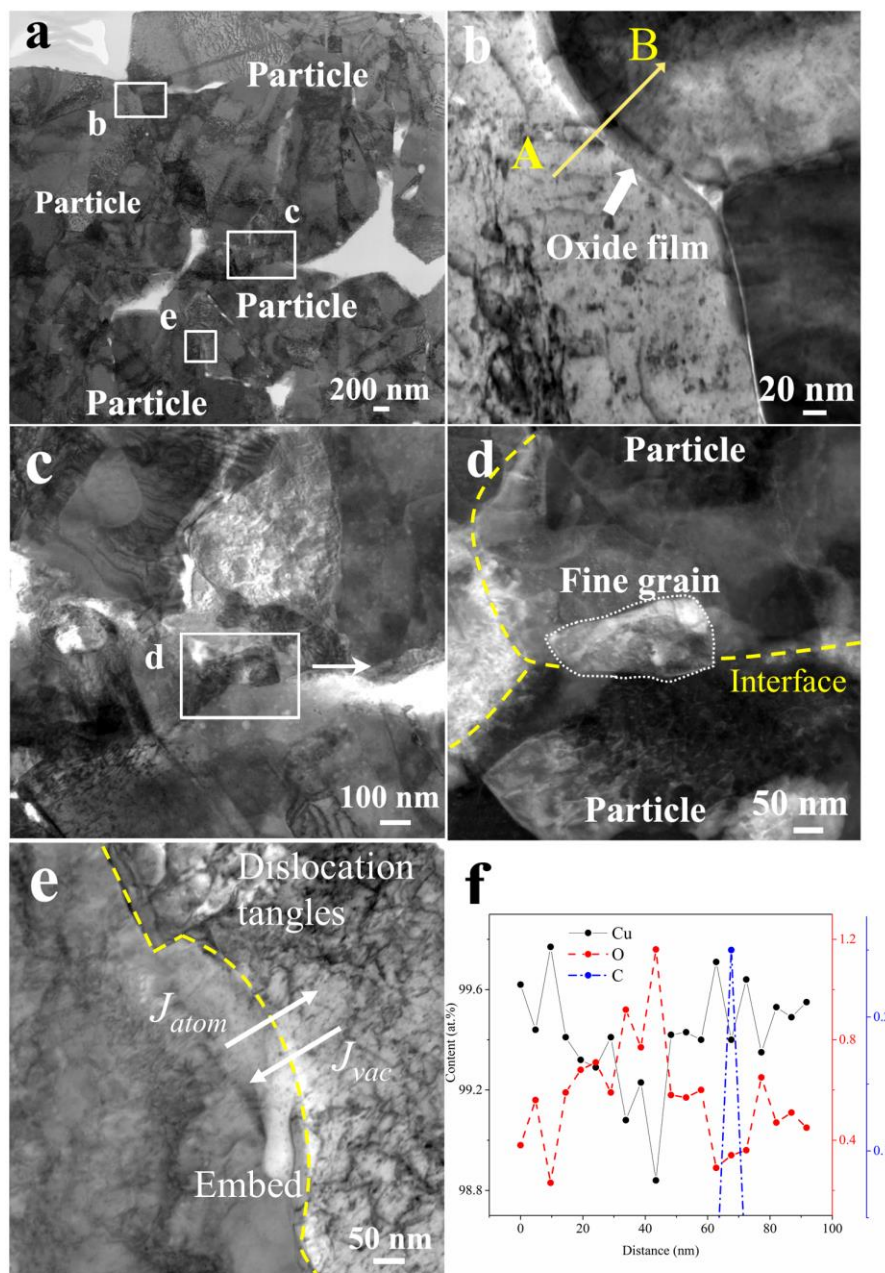


Figure 4.10 STEM images show (a) the bonding interfaces between the Cu microparticles, (b, c, and e) enlarged view of the marked area in the image (a), and (f) EDS line scanning result of the marked area in image (b).

diffusion of metallic atoms [16]. Although bonding could be achieved by this common oxide film that provides low shear strength for sintered joint (~ 15 MPa, see **Figure 4.3**), the oxide film is unreliable for its brittle nature. In another PBI (**Figure 4.10 e**), however, a micro-region deformation occurred at the interface, showing one microparticle embedded into the another; dislocation tangles were shown by the embedded one near the interface. It is considered as an effective bonding, since the PBI did not show brittle oxide, and common grain boundary are shared by the two surfaces. Furthermore, a fine grain across both interfaces was observed as revealed in **Figure 4.10 c and d**, which is believed to achieve solid bonding between two particles.

The above three PBIs present three stages of bonding formation. As illustrated in **Figure 4.11 a**, the first stage is majorly manifested in macro transformations at microparticle interfaces: under the ultrasonic vibration, interfacial oxide film cracked, and the acoustic softening effect and localized temperature together promoted deformation of microparticles, leading to the densification of the sintered matrix and tight contact between rough surfaces. With continuous influence of the ultrasonic vibration, a series of transformation occurred at the PBIs. As shown in **Figure 4.11 b**, driven by the spontaneous reduction of Gibbs free energy, the tight contacted surfaces gradually fuse through diffusion and are replaced by a common interfacial grain boundary (IGB) with lower surface energy. Meanwhile, with the high-frequency friction, the microparticle surfaces are softened; thus, the micro-region deformed as a result of acoustic softening. The micro-region deformation caused dislocation tangles at interfaces and drove dynamic

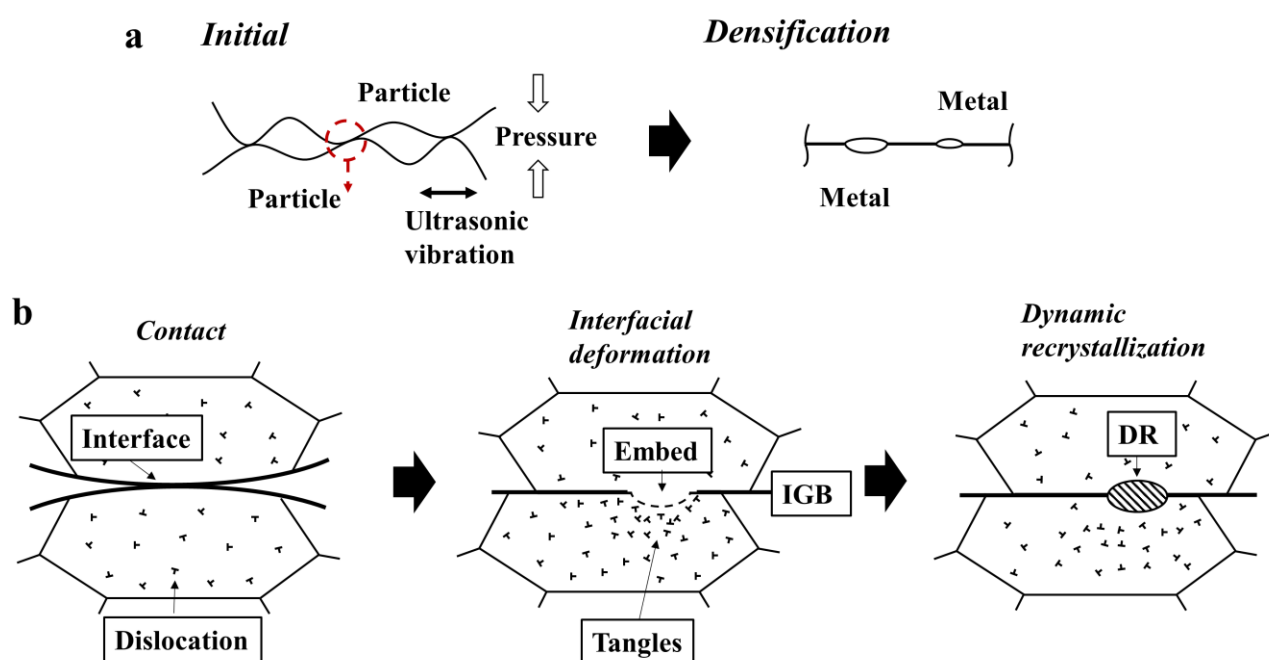


Figure 4.11 Schematic diagram illustrating (a) densification in a macroscopic view, and (b) dynamic recrystallization occurred at deformed micro region in a microscopic view. (IGB: interfacial grain boundary, DR: Dynamic recrystallization)

recrystallization (DR) because the rearrangement of the dislocations reduced system energy [17].

The dislocation tangles induced a difference in vacancy concentration, driving atoms and vacancies to diffuse across the interfaces; diffusion is the most significant factor during the dynamic recrystallization and sintering. Assuming that the formation and annihilation of vacancies occur freely, and the vacancy concentration in any region is in local equilibrium, then the atom flux (J_{atom}) and vacancy flux (J_{vac}) can be expressed as follows [18, 19]:

$$J_{atom} = -\frac{D_a}{RT} \nabla \sigma \quad (1)$$

$$J_{vac} = -\frac{D_v C_{v,\infty} V'_m \nabla \sigma}{RT} \quad (2)$$

Where D_a and D_v represent the atom and vacancy diffusion coefficient, respectively; σ is pressure; R is the Boltzmann constant; T is temperature in Kelvin degree; $C_{v,\infty}$ is the equilibrium vacancy concentration; V'_m is molar volume of vacancies. The plastic micro-region deformation released internal stress, causing a larger stress gradient between two microparticles and higher vacancy concentration. Based on the above formula, stress gradient increased atom and vacancy diffusion flux. Additionally, diffusion coefficient has been reported to be concentration-dependent, which increases with increasing concentration [20]. Therefore, diffusion and dynamic recrystallization were promoted at the deformed region where dislocation tangled.

4.4 Conclusion

This study proved the feasibility of ultrasonic process assembling and strengthening Cu/Cu joints. Optimization of protective solvent and parameters (bonding temperature, process time, and pressure) were presented. With the optimized ultrasonic processes, the Cu sintered joints with an average shear strength of 27 MPa and 39 MPa were assembled under the respective pressure of 7 MPa and 14 MPa. The ultrasonic vibration significantly promotes sintering of the spherical Cu microparticles, assisting to assemble a sintered joint rapidly at low temperatures. Based on test results and characterization, the bonding and strengthening mechanisms were discussed, and the main conclusions are addressed as follows.

1. Due to the ultrasonic vibration, the microparticles can be bonded at a low temperature and in a short time; thereby, the oxidation of the sintered matrix during the process is considerably averted. In the meantime, force vibration caused flows of the microparticles and voids which consequently

minimized the carbon residues, which would hinder interdiffusion of atoms.

2. Acoustic softening effects and localized high temperatures synergistically promoted micro-region deformation and dislocation tangles; the two high-energy features consequently drove dynamic recrystallization to generate IGBs and fine grains across IGBs. Thus, Cu microparticles were bonded firmly.

This study not only provides a process for assembling sintered joints with the Cu microparticles in the air, however, equally demonstrated how the Cu microparticles evolved, as well as its interfacial transformation under the ultrasonic vibration.

Reference

1. Nishikawa, H., T. Hirano, T. Takemoto, and N. Terada, Effects of joining conditions on joint strength of Cu/Cu joint using Cu nanoparticle paste. *The Open Surface Science Journal*, **3** (2011) 60-64.
2. Mou, Y., H. Cheng, Y. Peng, and M. Chen, Fabrication of reliable Cu-Cu joints by low temperature bonding isopropanol stabilized Cu nanoparticles in the air. *Materials Letters*, **229** (2018) 353-356.
3. Li, J., C. Cheng, T. Shi, J. Fan, X. Yu, S. Cheng, G. Liao, and Z. Tang, Surface effect induced Cu-Cu bonding by Cu nanosolder paste. *Materials Letters*, **184** (2016) 193-196.
4. Zuo, Y., S. Carter-Searjeant, M. Green, L. Mills, and S.H. Mannan, High bond strength Cu joints fabricated by rapid and pressureless in situ reduction-sintering of Cu nanoparticles. *Materials Letters*, (2020) 128260.
5. Fujimoto, T., T. Ogura, T. Sano, and A. Hirose, Joining of pure copper using Cu nanoparticles derived from CuO paste, Pan Pacific Microelectronics Symposium (Pan Pacific), (2016) 1-6.
6. Fujino, M., M. Akaike, N. Matsuoka, and T. Suga, Reduction reaction analysis of nanoparticle copper oxide for copper direct bonding using formic acid. *Japanese Journal of Applied Physics*, **56** (2017) 04CC01.
7. Liu, X. and H. Nishikawa, Low-pressure Cu-Cu bonding using in-situ surface-modified microscale Cu particles for power device packaging. *Scripta Materialia*, **120** (2016) 80-84.
8. Morisada, Y., T. Nagaoka, M. Fukusumi, Y. Kashiwagi, M. Yamamoto, and M. Nakamoto, A low-temperature bonding process using mixed Cu–Ag nanoparticles. *Journal of electronic materials*, **39** (2010) 1283-1288.
9. Xiong, J., Y. Wang, Q. Xue, and X. Wu, Synthesis of highly stable dispersions of nanosized copper particles using L-ascorbic acid. *Green Chemistry*, **13** (2011) 900-904.
10. Jingyan, S., L. Yuwen, W. Zhiyong, and W. Cunxin, Investigation of thermal decomposition of ascorbic acid by TG-FTIR and thermal kinetics analysis. *Journal of pharmaceutical and biomedical analysis*, **77** (2013) 116-119.
11. Kirk-Othmer, *Encyclopedia of Chemical Technology*, John Wiley & Sons, (2007), DOI:10.1002/0471238961.0119031511210512.a01.pub2.
12. Xiangdong, L., Novel bonding process using surface-modified microscale Cu particles for high-temperature electronic packaging. (2017), 120.
13. Vernin, G., S. Chakib, S.M. Rogacheva, T.D. Obretenov, and C. Párkányi, Thermal decomposition

- of ascorbic acid. *Carbohydrate research*, **305** (1997) 1-15.
14. Christoph, R., B. Schmidt, U. Steinberner, W. Dilla, and R. Karinen, Glycerol. *Ullmann's encyclopedia of industrial chemistry*, (2000), DOI: 10.1002/14356007.a12_477.pub2.
 15. Ross, R.B., *Metallic materials specification handbook*, Springer Science & Business Media, 2013, 94-170.
 16. Magdassi, S., M. Grouchko, and A. Kamyshny, Copper nanoparticles for printed electronics: routes towards achieving oxidation stability. *Materials*, **3** (2010) 4626-4638.
 17. Rios, P.R., F. Siciliano Jr, H.R.Z. Sandim, R.L. Plaut, and A.F. Padilha, Nucleation and growth during recrystallization. *Materials Research*, **8** (2005) 225-238.
 18. Berrin, L. and D.L. Johnson, Precise Diffusion Sintering Models for Initial Shrinkage and Neck Growth. (1967) 92-369.
 19. Kang, S.-J.L., *Sintering: densification, grain growth and microstructure*, Elsevier, (2004) 43-104.
 20. Nestle, N. and R. Kimmich, Concentration-dependent diffusion coefficients and sorption isotherms. Application to ion exchange processes as an example. *The Journal of Physical Chemistry*, **100** (1996) 12569-12573.

Chapter 5

Long-term reliability and failure mechanism of the joints assembled with metallic microparticles

5.1 Introduction

Reliability and lifetime are critical issues for die-attach bonding, which rely on the materials used and processes adopted. Especially, the semiconductors of power devices serve at a high-temperature and high current conditions; the bonding requires a stable metallization structure for long-term reliability at high temperatures. In *Chapter 2 – 4*, three bonding processes using Ag and Cu microparticles have been investigated, but the proof on their long-term reliability and behaviors at high-temperature operation has not been proven.

In this chapter, joint specimens using the processes presented in *Chapter 2 – 4* were prepared with optimized parameters; then high-temperature aging was conducted in the air to simulate the situation

where the packaging hermetic encapsulant fail and oxygen infiltrate. Following aging for various time intervals, the mechanical and microstructural behaviors of the joints were examined. Through the comparison between aged joints obtained under varying conditions, factors that impact the long-term reliability of the joints assembled by metallic microparticles were studied.

5.2 Experimental

5.2.1 Preparation of aged joint specimens

The three die-attach methods investigated in Chapters 2 – 4 were adopted to assemble sintered joints with their optimized parameters. For ease of expression, the joints fabricated under different conditions with different materials were named as #1 - #4 joints. The materials used and corresponding parameters are listed in **Table 5.1**. The #1 and the #2 joints were prepared using the method and optimal parameters studied in Chapter 2, namely, reductive sintering of Cu microparticles at formic acid atmosphere at 300 °C for 30 min after preoxidation for 20 min; the #1 joints assembled with Cu substrates while the #2 joints assembled with ENIG (electroless nickel immersion gold-finished Cu cylindrical disks) substrates. The #3 joints were prepared by sintering the Ag chestnuts-burr-like microparticles (*Chapter 3*) with the ultrasonic-assisted bonding process for 5 min; the ultrasonic amplitude, the pressure, and the setting temperature were 5 μ m, 7MPa (50 N), and 300 °C (actual temperature: 240 °C), respectively. The #4 joints were prepared by sintering organic-protected spherical Cu microparticles for 15 min with the same ultrasonic vibration as the #3 joints (see details in *Chapter 4*); the ultrasonic amplitude, the pressure, and the setting temperature were 5 μ m, 7MPa (50 N), and 240 °C (actual temperature: 200 °C), respectively. The joint specimens are sandwich structures consisting of an upper disk, a sintered matrix, and a bottom disk, and their dimensions are illustrated in **Figure 3.1** and **Figure 4.1**. Since all joints were bonded by metallic microparticles paste, the fabrication of joint specimens can be summarized as follows. Both upper and bottom disks were first cleaned ultrasonically in dilute hydrochloric acid (4%) and rinsed with ethanol.

Table 5.1 Different process and conditions used in this study to obtain bonding joints.

	Methods	Materials	Substrate	Condition (actual temperature, process time)
#1	Chapter 2	Cu 1400YM	Cu	Reductive process (300 °C, 30 min)
#2	Chapter 2	Cu 1400YM	ENIG	Reductive process (300 °C, 30 min)
#3	Chapter 3	Ag microparticles	ENIG	Ultrasonic process (50 N, 240 °C, 5 min)
#4	Chapter 4	Cu 1400Y	Cu	Ultrasonic process (100 N, 200 °C, 15 min)



Figure 5.1 Joint samples prepared with different conditions after ageing for various time intervals.

Then, 150 μm -thick paste layers were stencil-printed on the surfaces of the bottom disks. Finally, the upper disks were mounted on the as-printed paste, and the whole specimens were then processed in corresponding devices to fabricate joints. The #1 and #2 joints were fabricated in a large-area bonding machine (RB-100D, Ayumi Industry Co., Ltd), while the #3 and #4 joints were fabricated in a thermal pressure bonding device (HTB - MM, Alpha Design Co., Ltd).

The as-fabricated joint specimens were put in an oven (FH-360, Toyo Seisakusho Kasha, Ltd.) to be thermally aged at a constant temperature of 200 $^{\circ}\text{C}$ in the air for 168 h (1 week), 504 h (3 weeks), and 1008 h (6 weeks). The joint specimens after aging for varying time intervals were shown in **Figure 5.1**. It is noted that the #1 and #2 joints failed naturally after aging for 1008 h, and the sandwich structure disintegrated; as the consequence, no cross-sectional samples can be prepared for #1 and #2 joints after aging of 1008 h.

5.2.2 Characterization methods

The mechanical performance of aged specimens was estimated by average shear strength, which was determined by three specimens and tested by a shear tester (STR-1000, Rhesca) with a head speed of 1 mm/min; the fly height was set at 200 μm from the surface of the bottom Cu disk. After the shear test, fracture surfaces were observed by a field emission scanning electron microscope (FESEM; SU-70,

Hitachi). Other unsheared joints were molded in a cured epoxy then cut from the middle to prepare cross-sectional samples, which were then polished using a cross-section polisher (SM-09010, JEOL) with ion milling to prevent the microparticles from smearing into the pores during grinding and polishing. After that, the cross-sectional samples were observed by the SEM, an electron probe microanalyzer (EPMA; JXA-8530F, JEOL), and a transmission electron microscope (TEM; JEM-2100, JEOL) after preparation of a focused ion beam (FIB; JIB-4500, JEOL). Based on cross-sectional SEM images, the porosity can be calculated by the equation: $p = \Sigma A_i / A$, where A_i is the area of each void, and A is the area of the whole bonding layer. Areas and normalized diameter of voids were measured based on the cross-sectional SEM images and calculated by the software Image-pro (Ver. 6.0).

5.3 Results and discussion

5.3.1 Shear strength of the joints assembled with different materials and processes

Changes in shear strength of joints obtained under diverse conditions with increasing aging time are shown in **Figure 5.2**. Overall, the #1 and #2 joints (namely, assembled through sintering of preoxidized Cu microparticles in the formic acid atmosphere) exhibit similar shear strength (~32 MPa) and both decreased with the extending aging time. The deterioration behavior of two kinds of joints in the subsequent aging are also similar: after aging of 168 h, average shear strength reduced to half (15 MPa);

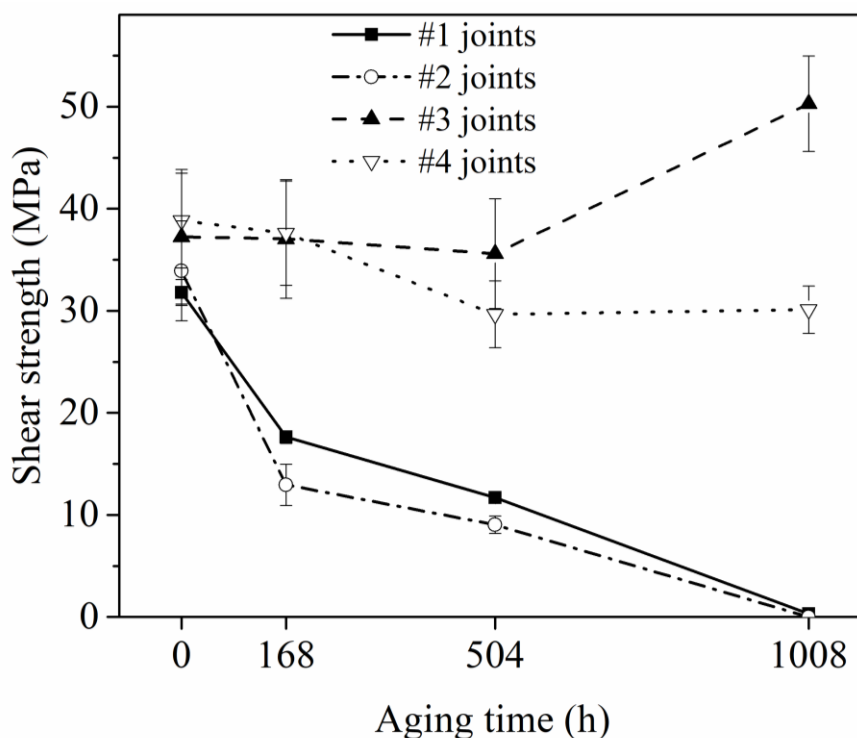


Figure 5.2 Shear strength of the #1 - 4 joints after the aging for different time intervals.

after aging of 1008 h, the joints debonded naturally, and the sintered matrix detached from upper and bottom disk, as shown in **Figure 5.1**. In contrast, the #3 and #4 joints (namely, assembled by the ultrasonic process in the air) exhibited the resistance to thermal aging in the air, and they sustained high shear strength (above 30 MPa) even after aging of 1008 h regardless of the particle materials used. It should be noted that the shear strength of the joints obtained with Cu microparticles (condition #4) decreased with increasing aging time, and attained 30 MPa after aging of 504 h. Subsequently, the shear strength became stable and barely decrease even when aging time was extended to 1008 h. However, the joints obtained with the Ag microparticles were barely influenced by the aging that was less than 504 h, and there was even an increase in the average shear strength to 50 MPa after the aging for 1008h. Summarily, as regards the average shear strength, the long-term reliability of the sintered joints is least significantly impacted by substrates, followed by particle materials having a moderate impact, and bonding processes have the most significant impact among them. Since the mechanical behavior of one joint highly is related to the corresponding microstructure, it is crucial to explore the microstructural evolution of the sintered joints during thermal aging.

5.3.2 Microstructure transformation of the Cu/Cu joints obtained by reductive sintering of preoxidized Cu microparticles

The thermal aging equally influenced failure modes of the #1 joints, which were assembled by reductive sintering of preoxidized Cu microparticles at formic acid atmosphere. **Figure 5.3** depicts the fracture surfaces of joints following thermal aging for 0, 168, and 504 h. It is obvious that cohesive failure occurred mainly within the bonding layer during the shear test in the original joints because microparticles were attached to both the top and bottom sides of the fracture surfaces. In contrast, the joints after aging (both 168 and 504 h) detached at the bonding layer/bottom disk interfaces, due to the fact that the sintered matrix was attached majorly on one side, and the bare substrate can be observed on another side. On the account of the attachment of the sintered matrix, the part of the parent microparticles wrapped in the oxide was revealed by the flat destruction surfaces of the oxide. As a result, brittle fracture of oxide at the interfaces is predicted to be an aftermath of failure of aged joints. The joints with sandwich structure were observed to naturally debond after aging for 1008 h, and the sintered matrix detached from both the upper and bottom disks, as shown in **Figure 5.4 a**. The fracture surfaces on the upper and bottom disks exposed bare substrate with no sintered residues, as shown in **Figure 5.4 b** and **e**. Additionally, flat and smooth films are observed on fracture surfaces of the peeled off sintered matrix at both upper and bottom sides,

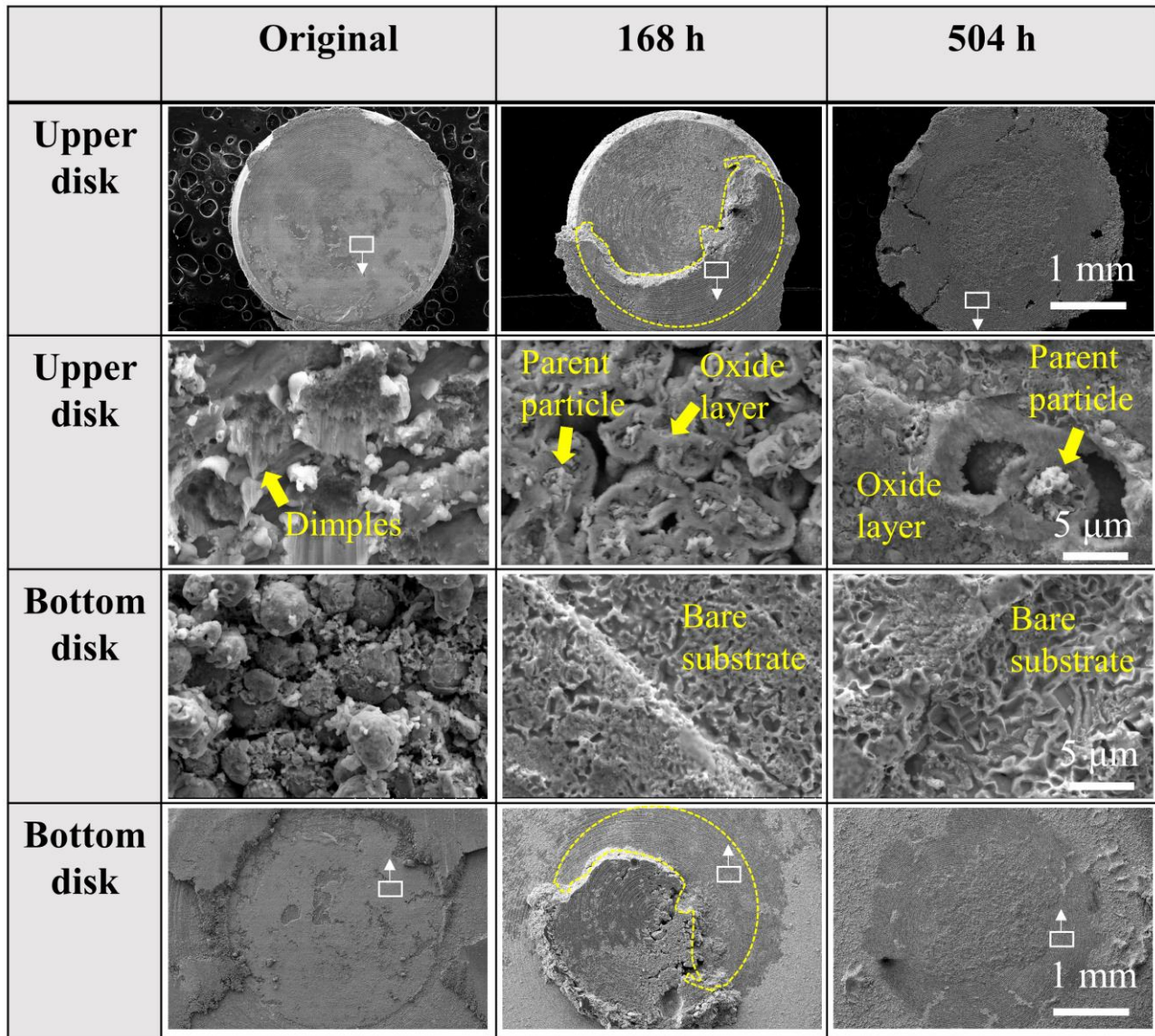


Figure 5.3 Fracture surfaces of the #1 joints after aging for different time intervals.

which were considered as Cu oxide film. It is suggested that the sintered matrix peeling off is due to the interfacial debonding.

The cross-sectional microstructures at bonding interfaces of the #1 joints after aging of varying time intervals were observed, as shown in **Figure 5.5**. Overall, a sintered matrix with high density was obtained in the original joint, and the sintered matrix was transformed into a mixture of oxide and parent microparticles after aging. The EDS results indicate that the main oxide was Cu_2O while parent microparticles remained Cu. With an increase in aging time from 168 to 504 h, a large number of tiny voids formed in the parent microparticles as the amount of oxide barely changed. Additionally, a continuous oxide layer formed at the substrate/sintered matrix interfaces after aging for 168 h.

It is reasonable to theorize the microstructural transformation of the sintered matrix as follows: the bonding layer gradually oxidized in the air under the condition of increasing temperature. Since gaps

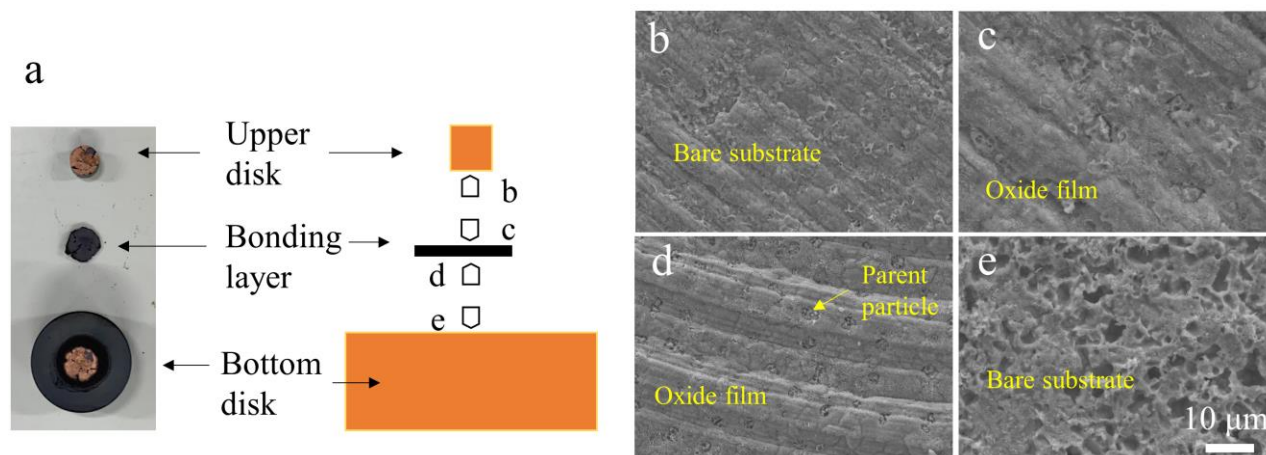


Figure 5.4 Debonding of the sintered matrix of #1 joints after aging for 1008 h: (a) schematic diagram, and (b) SEM images of the detached surfaces on (b) the upper disk, (c) upper area of the sintered matrix, (d) bottom area of the sintered matrix, and (e) the bottom disk.

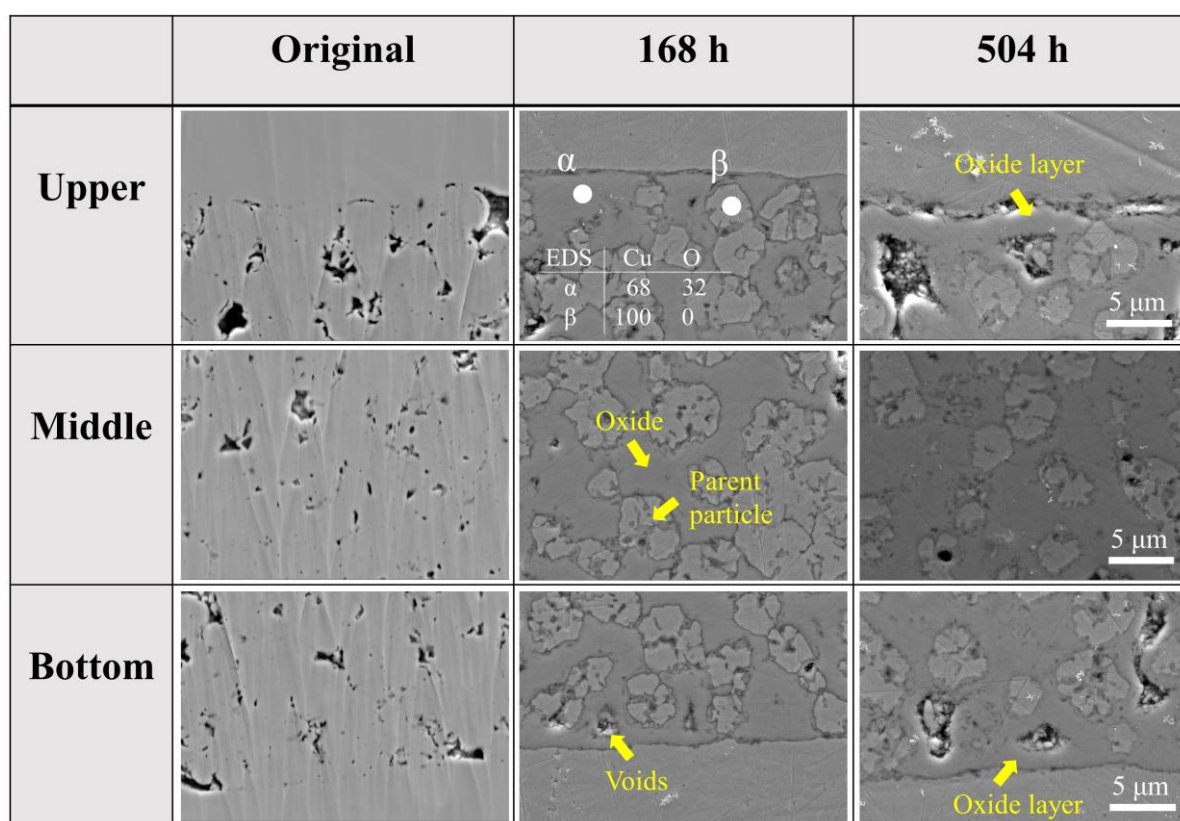


Figure 5.5 Cross-sectional SEM images of the #1 joints after aging for different time.

between the microparticles exist in the as-sintered joints, the oxidation is always initiated at the periphery of the gaps and subsequently proceed inward. When the oxide layer reached a critical thickness, as described in *Chapter 2*, the oxidation rate is drastically reduced by the barrier of the oxide layer and consequently, the amount of oxide increased negligibly with further thermal aging. At this stage, Cu atoms diffuse toward the Cu_2O layer from parent Cu microparticles, and the vacancies diffusing into parent Cu microparticles induced the formation of a large number of tiny voids. These voids cluster and segregate upon further oxidation, leaving circular pores inside the parent microparticles. The common byproduct of

oxidation of both the substrate and the Cu microparticles are the oxide layers at the bonding interface, as it has been reported that similar oxide layers could form in Ag-sintered joints assembled with Cu substrate during thermal aging [1]. As discussed in *Chapter 2*, the P-B ratio of Cu_2O is 1.65, which indicates the volume expansion when Cu is oxidized. Therefore, the expanded oxide fills the voids in the original sintered matrix, and the oxide layer at the bonding interfaces formed owing to the accumulation of oxide generated through oxidation of both the substrates and interfacial microparticles. It has been reported that shear strength of the aged joints assembled with Cu substrates was significantly reduced by the oxide layer formed at interfaces [3]; therefore, it is necessary to investigate the bonding interfaces between the oxide layers and substrates.

Figure 5.6 a shows a STEM image of the bonding layer at bonding interfaces after aging for 504 h, and **Figure 5.6 b** depicts the interfaces between the oxide and the substrate in an enlarged view of the marked area. The oxide is identified by diffraction (point α , containing a subgrain) as Cu_2O , and the oxide grains near the interface are equiaxial; the substrate on the other side, as identified by diffraction in point β , is pure Cu. Tiny voids were also observed at the oxide/substrate interfaces, which resulted from the interdiffusion between Cu atoms and vacancies when the interfacial oxide layer formed.

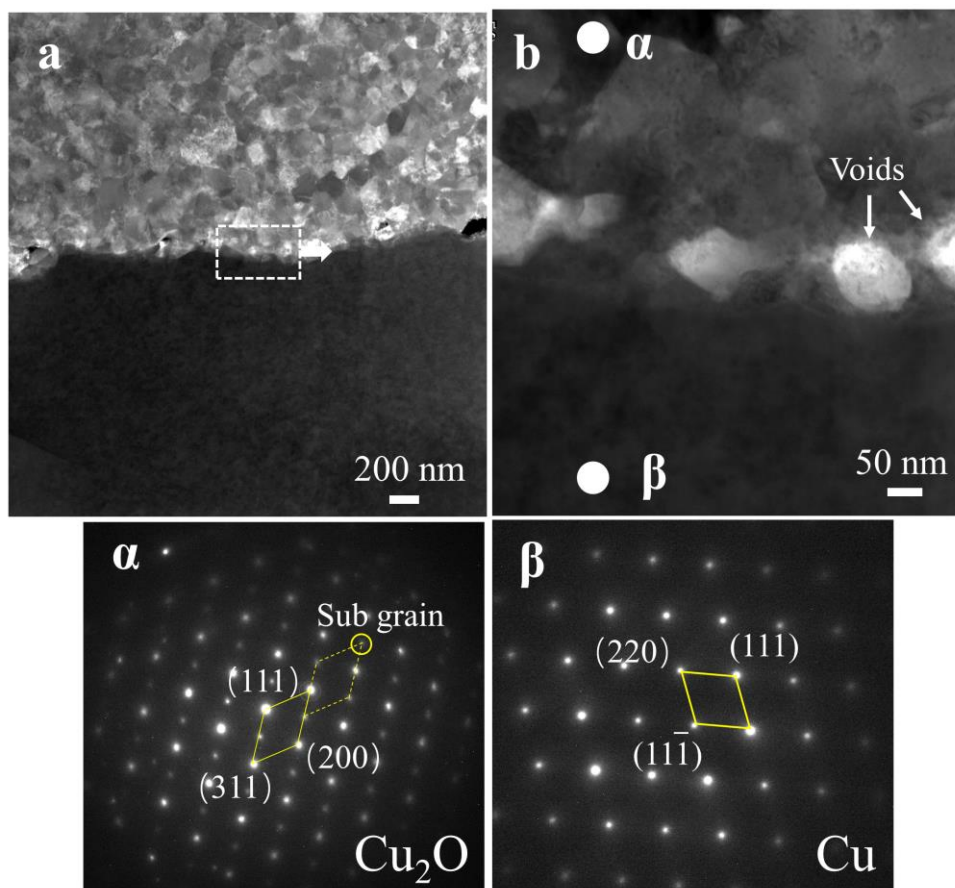


Figure 5.6 TEM of bonding interface of the #1 joint after aging for 504 hours: (a) STEM images, (b) enlarged view in image(a), and (α , β) diffraction pattern of the areas marked by white points.

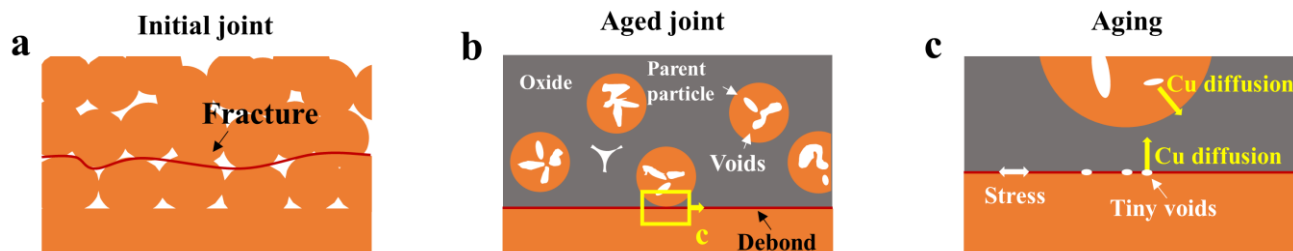


Figure 5.7 Schematic diagram of failure modes of the #1 joints (a) before and (b) after aging, and (c) voids formation during aging.

Based on the above discussion, the fracture mechanisms of #1 joints before and after aging are illustrated in **Figure 5.7** and addressed as follows. In as-sintered joints, a large number of gaps between the microparticles are uniformly distributed in the sintered matrix, readily inducing stress concentration and cracks initiation. Therefore, adhesive failure mainly occurs within the sintered matrix, as revealed in **Figure 5.7 a**. After thermal aging, Cu oxide forms on both particle and substrate surface, filling the gaps that would have caused stress concentration due to volume expansion. The oxide formed on substrates, as well as nearby Cu microparticles accumulate and integrate for generating a continuous oxide interlayer between the sintered matrix and substrates. Moreover, the formation of oxide leads to formation of many voids inside the microparticles because Cu atoms tend to diffuse outside to react with oxygen. In such case, the fracture mainly occurs at the substrate/oxide interlayer interface, as shown in **Figure 5.7 b**, and the reason is illustrated in **Figure 5.7 c**. The shear stress is induced by volume expansion of Cu oxide, which gradually increased with the thickening oxide because brittle oxide barely accommodates thermal misfit dislocation plastically [3]. The tiny voids are generated at the bonding interfaces due to interdiffusion between Cu atoms and vacancies, inducing stress concentration in return. Consequently, the shear strength of the aged joints dramatically decreases, and the fracture mainly occurs at the bonding interfaces. With further aging, once sufficient voids were clustered, eventually brittle debonding occurs at oxide layer/substrate interfaces, thereby causing separation of the whole sintered matrix.

5.3.3 Microstructure transformation of the Ag-sintered joints obtained with the ultrasonic process

After aging for varying time intervals, #3 joints were sheared, and their fracture surfaces were observed, as shown in **Figure 5.8**. Overall, a considerable number of dimples were left in all upper and bottom fracture surfaces, revealing that the aging barely changed the ductile fracture pattern of the original joints. As explained in *Chapter 3*, the initial joints left most sintered matrix on the one side, and many dense layer residues were observed on the other side; therefore, it is concluded that failure mainly occurred at the dense layer/sintered matrix interface. However, after aging of 168 h, #3 joints left clear

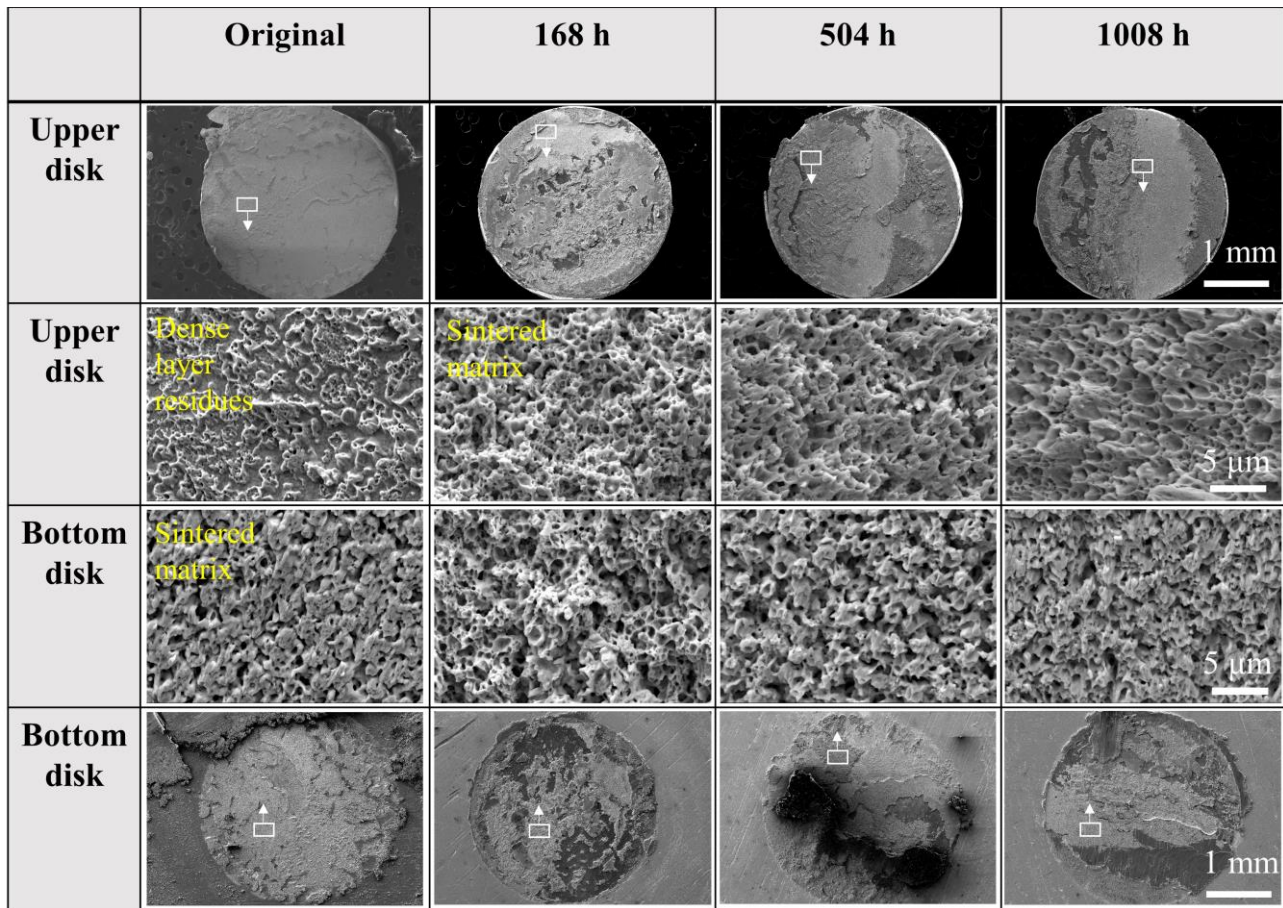


Figure 5.8 Fracture surfaces of the #3 joints after aging for different time.

sintered matrix on both upper and bottom sides; it affirms that fracture location transferred to the interior of the sintered matrix. The fracture location and failure mode did not change, even when aging time was extended to 1008 h.

Cross-sectional SEM images of #3 joints after aging for different time are shown in **Figure 5.9**. Additionally, porosity and void size (diameter) were measured and calculated by three different cross-sectional SEM images, as shown in **Figure 5.10**. According to the two figures, the most intuitive effects of thermal aging on the microstructural transformation are the densification of the sintered matrix and the accumulation of voids. In the initial joint, dense layers at the bonding interfaces (discussed in *Chapter 3*) and irregular voids are readily observed, as shown in **Figure 5.9 a-1** and **a-3**. These irregular voids are gaps between the microparticles and needles. After aging for 168 h, a large area of dense microstructures (marked as DM in the figure) appeared in the interior of the sintered matrix, as observed in the overview (**Figure 5.9 b-2**). Moreover, spherical pores with a normalized diameter of 5 μm formed in the dense microstructure (**Figure 5.9 b-3**). For ease of expression, the voids with normalized diameters large than 2 μm are termed as pores. After aging for 504 h, dense microstructures connected and accumulated, separated with areas where voids concentrated, as shown in **Figure 5.9 c-1, 2, 3**. After further aging of 1008 h, as shown in **Figure 5.9 d**, most voids were changed into spherical shape, and pores with large

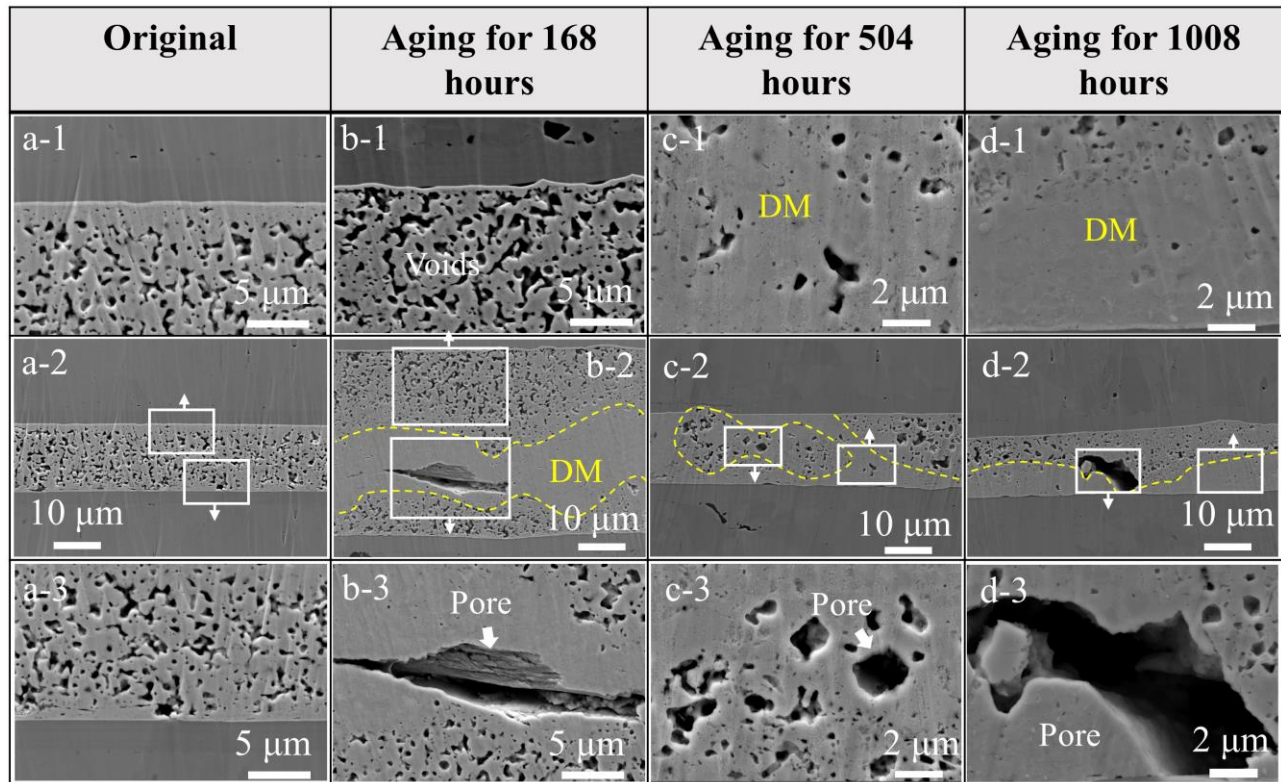


Figure 5.9 Cross-sectional SEM images of the #3 joints after aging for different time.

diameter appeared in the sintered matrix. Meanwhile, continuous dense microstructures formed around pores and voids, which separated pores from other void areas (Figure 5.9 d-3).

The change in porosity and void size with increasing aging time is shown in Figure 5.10. The initial joint exhibited a porosity of 16.57 % and an average void size of 0.44 μm . After 168 h of aging, porosity and average void diameter increased slightly by 2.8 % and 0.02 μm , respectively, and then decreased with aging time to a minimum of 7.43 % and 0.28 μm . Taking Siow's illustration as a reference [4], we summarize the transformation of sintered microstructures, including the evolution of voids, porosity, and dense microstructures, as follows. Because the Ag microparticles were sintered at approximately 240 $^{\circ}\text{C}$, the aging at 200 $^{\circ}\text{C}$ can be regarded as a continuation of sintering or subsequent annealing for the sintered joints. During the first 168 h of the aging process, evenly distributed voids started to segregate and merge, increasing in void size with reduction in void number; therefore, both the porosity and void size slightly increased. With aging continuing, the high aging temperature promotes grain boundary and lattice diffusion, through which mass transports within the sintered matrix became possible. Lots of free surfaces and micro deformation remain at the sintered microstructures after the ultrasonic process, which tends to be replaced by interfacial grain boundaries to reduce the surface energy and are eliminated by following grain growth. During this process, vacancies in the grain diffuse towards the grain boundary, and the voids shrink or disappear through grain boundary and surface diffusion, hence the decrease in porosity and void

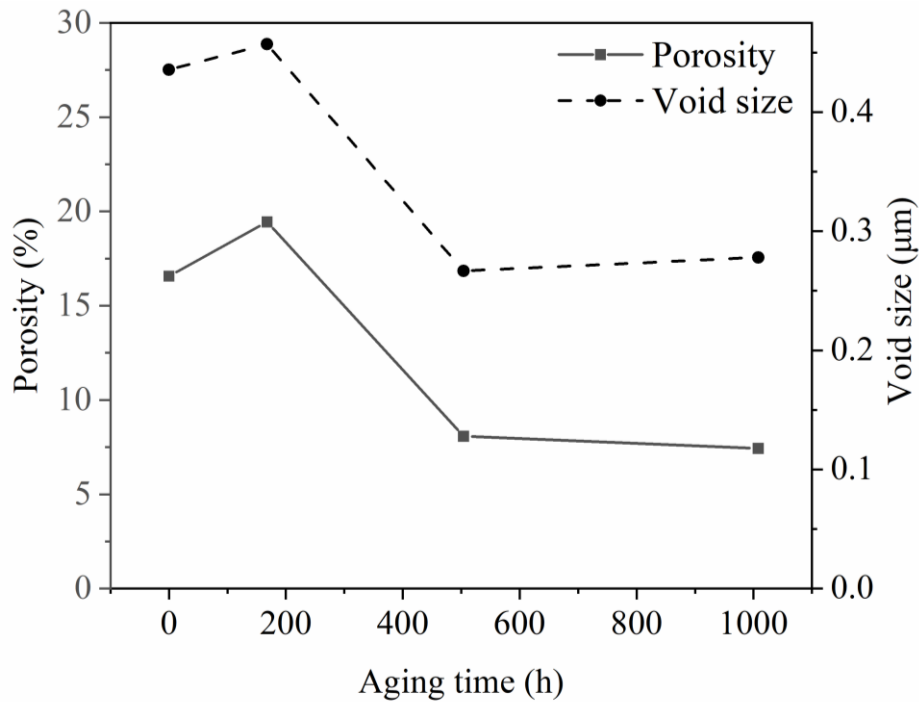


Figure 5.10 Porosity and size of voids (average diameters) with increasing aging time.

size [5]. Finally, porosity stops declining when the microstructure matured and vacancies in grain boundaries are saturated.

In addition, void shapes gradually transformed from irregular to sphere, and the number of voids decreased when large pores appeared. Fu et al. reported that the void shape is highly correlated with sintering parameters, and increasing sintering temperature or extending hold time increases the proportion of spherical voids [6]. The driving force for irregular voids transforming into spherical is the reduction of surface energy, which means the reduction of total internal voids surface area. It drives vacancies diffused from voids to pores and induces the disappearance of small voids and the growth of large pores [7]. Therefore, the irregular voids with higher specific surface energy merged and were transformed into larger sphere pores.

Based on the above discussion, we surmise the relationship between transformation of sintered microstructures and failure modes, as illustrated in **Figure 5.11**. Fracture position of the original #1 joints is the sintered matrix/dense layer interfaces, which has been discussed in *Chapter 3* and shown in **Figure 5.11 a**. After aging, dense microstructures appeared within the sintered matrix, instead of being generated at upper and bottom bonding interfaces as original joints. With the formation of dense microstructures within the sintered matrix, void areas where voids and pores evenly distributed also formed. Stress concentration readily occurs in the void areas, leading to crack initiation. When the void areas occupy most of the sintered matrix, cracks can pass through these void areas and break through the whole sintered

matrix, as shown in **Figure 5.11 b**. With extending aging, vacancy diffusion segregates voids and generates pores, which equally causes the disappearance of voids to generate large areas of the dense microstructures separating pores. To propagate between pores, cracks need to pass through a long distance in dense microstructures, as shown in **Figure 5.11 c**. Therefore, both path length and required fracture energy for cracks propagation increase, hence the higher shear strength.

ENIG substrates have been previously reported to cause Ag-sintered joint to form a dense layer at bonding interfaces after aging, while voids are generated at the dense layer/ENIG interfaces because excessive Ag atoms diffused into Au-plating layers, which eventually cause delamination [8]. Additionally, Yang et al. suggested that the Ag dense layers formed during aging, accompanied by a loose microstructure formed between the sintered Ag matrix and the dense sintered layer [9]. Although the diffusion of Ag into the plating layer was observed by EPMA as shown in **Figure 3.15**, no such degradation occurred, while diffusion behavior and other possible degradation during thermal aging still need investigation.

The cross section of joints after aging was examined by EPMA, and results are shown in **Figure 5.12**. Overall, due to Ag's excellent resistance to oxidation, the oxide content in the sintered matrix remains extremely low even after aging for 1008 h. Due to the hindrance of the Ni plating layer, no diffusion of Au and Ag into the Cu nor the diffusion of Cu and Ni into the sintered matrix were observed. Therefore, the diffusion behavior of the joints during aging simply involved the Ag and Au in the sintered matrix. After aging for 168 h, interdiffusion between Ag in the sintered matrix and Au in the plating layer made the Au plating layer a solid solution of Ag and Au. As the aging time is extended, Au continuously diffuses into the sintered matrix. However, due to the very thin plating layer of Au (~50 nm), the Au diffusion did not cause obvious delamination and interfacial voids, even after aging for 1008 h. It can be concluded that the material and vacancy transport between the substrate and sintered matrix has little influence on the joints.

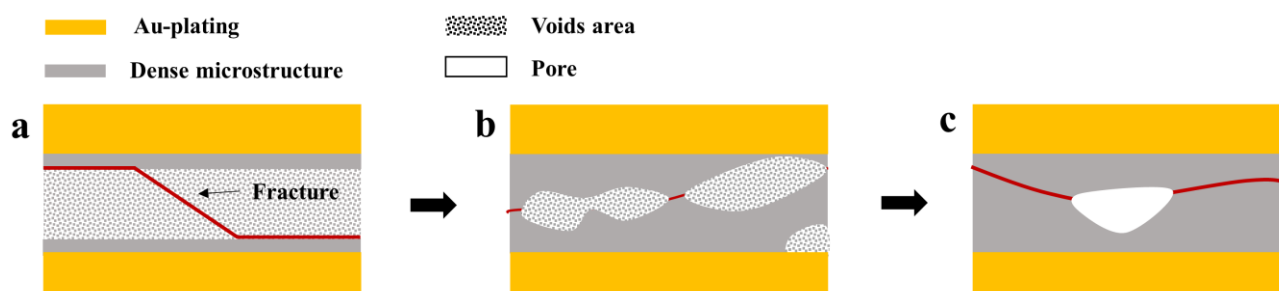


Figure 5.11 Schematic diagram of failure modes of #3 joints after aging.

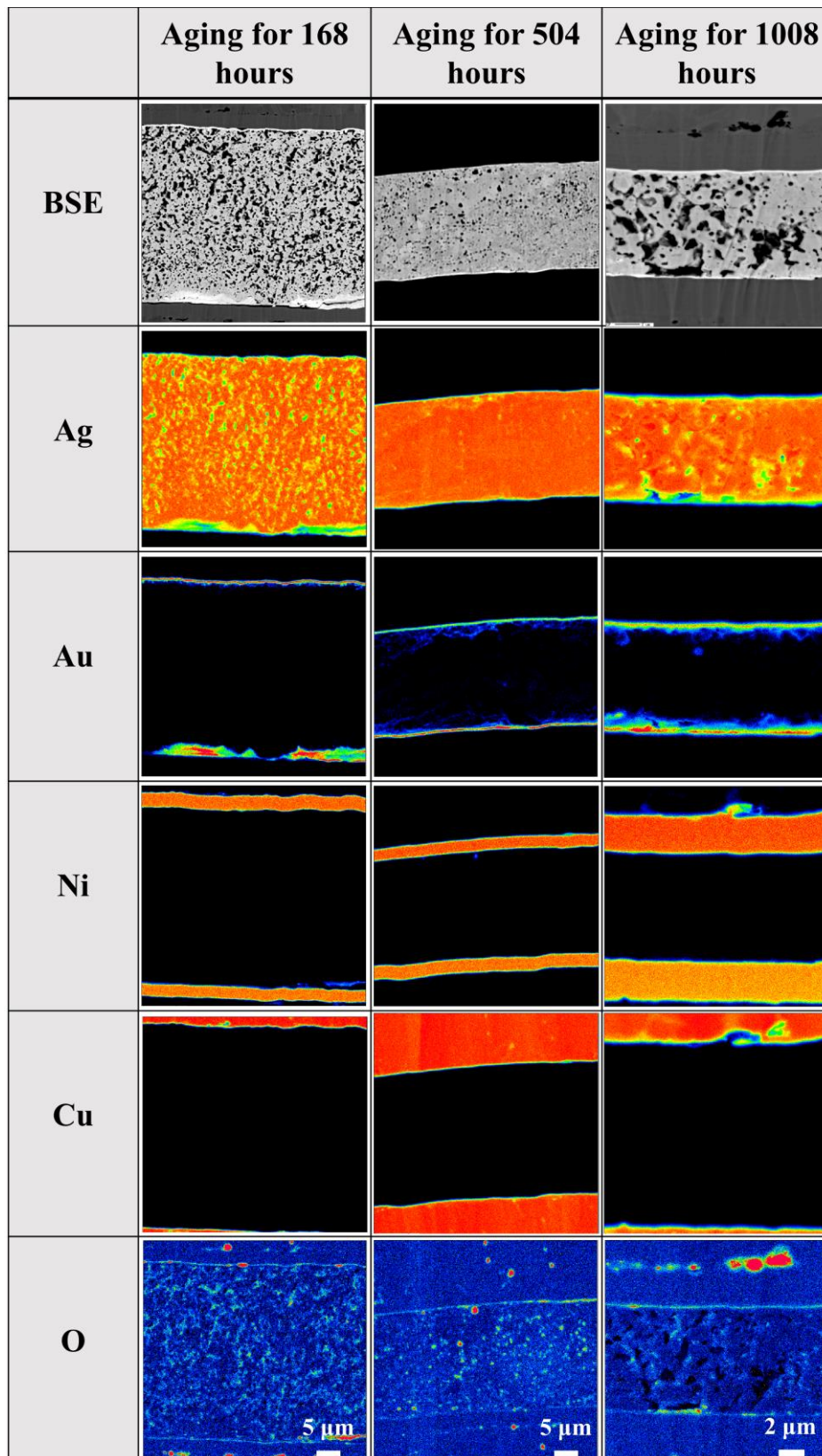


Figure 5.12 EPMA results of the #3 joint after aging for different time.

5.3.4 Microstructure transformation of the Cu/Cu joints obtained by ultrasonic-assisted bonding method using organic-protected Cu microparticles

The #4 joints, which were assembled through the ultrasonic process with Cu microparticles, were observed on their fracture surfaces to investigate the failure mode before and after aging, and the fractography SEM images are shown in **Figure 5.13**. Overall, thermal aging barely affected the fracture position of the joints but changed the fracture mode. It is considered that the original joints and the aged joints both fractured within the sintered matrix, according to residues of the sintered matrix on both upper and bottom fracture surfaces. However, a large number of dimples on the fractography of the original joints indicated a ductile fracture, while the flat fracture surfaces of the joints after aging 168 and 504 h suggested obvious brittle cleavage, where intact parent microparticles embedded in the oxide. It is deduced that the failures of the joints after aging were mainly due to oxide fracture, and the crack propagated along the edge of the parent microparticles rather than passing through them. On the fracture surface of the joint after aging for 1008 h, a small area was observed to fail at the bonding interface (marked in the white box), exposing bare substrate on the bottom fracture surface. Both the upper and bottom fracture surfaces of this area are observed to have dimples; this suggests that the interfacial ductile

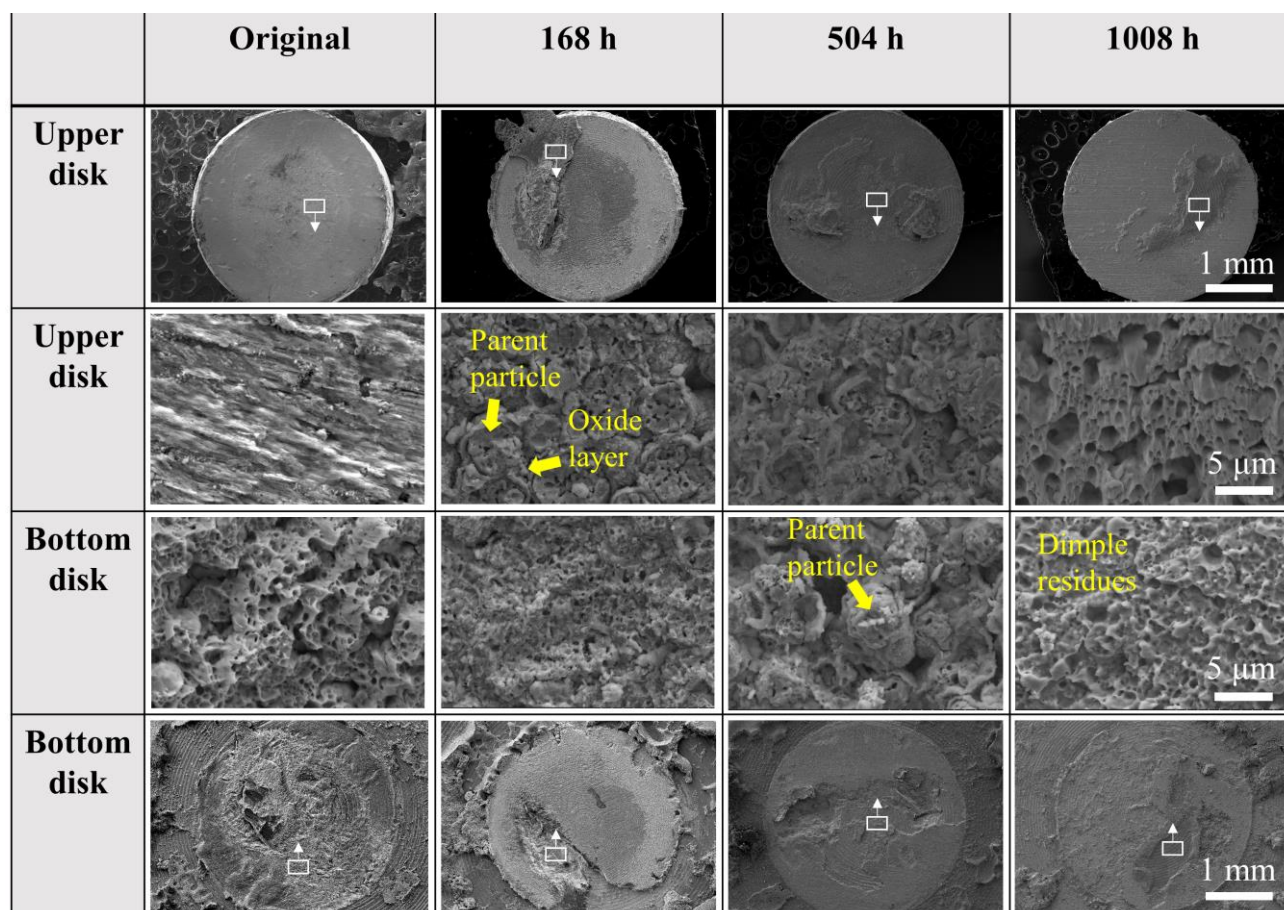


Figure 5.13 Fracture surfaces of the #4 joints after aging for different time.

failure of the #4 joint was substantially different from the brittle interfacial debonding of the #1 joints after aging.

Cross-sectional SEM images of #4 joints after aging for various time intervals are shown in **Figure 5.14**. Similar to the aged #1 joints (**Figure 5.5**), the oxide was generated in the sintered matrix after aging, coating the parent microparticles and filling voids, because of the poor oxidation resistance of Cu. Additionally, voids inside the parent microparticles also formed due to Cu atoms diffused outward to generate oxide. After aging for 504 h, oxide layers formed in certain regions of the upper interface, separating the sintered matrix from the substrate; however, there is a direct bond between the microparticles and substrates without an oxide interlayer between them. Even after the aging for 1008 h, the oxide layer formed at the upper interface remained thin and discontinuous.

The findings above coupled with analysis in *Chapter 4* that base on ultrasonic vibration effect on sintered microstructure, the details account of failure mechanism is expressed through **Figure 5.15** and expressed below. As regards the initial joints, the microparticles compactly bond the substrate at the bonding interface because the ultrasonic vibration promotes deformation and recrystallization. Nevertheless, the weakest part whereby the fracture occurs within is the sintered matrix containing massive voids, which cause stress concentration, as depicted in **Figure 5.15 a**. Although the microparticles and the substrate are oxidized during aging, the tightly bonding between them prevents formation of the continuous oxide layer at interfaces. Therefore, the joint shear strength barely decreased after aging for less than 504 h. As the aging progresses, the proportion of oxide in the sintered matrix

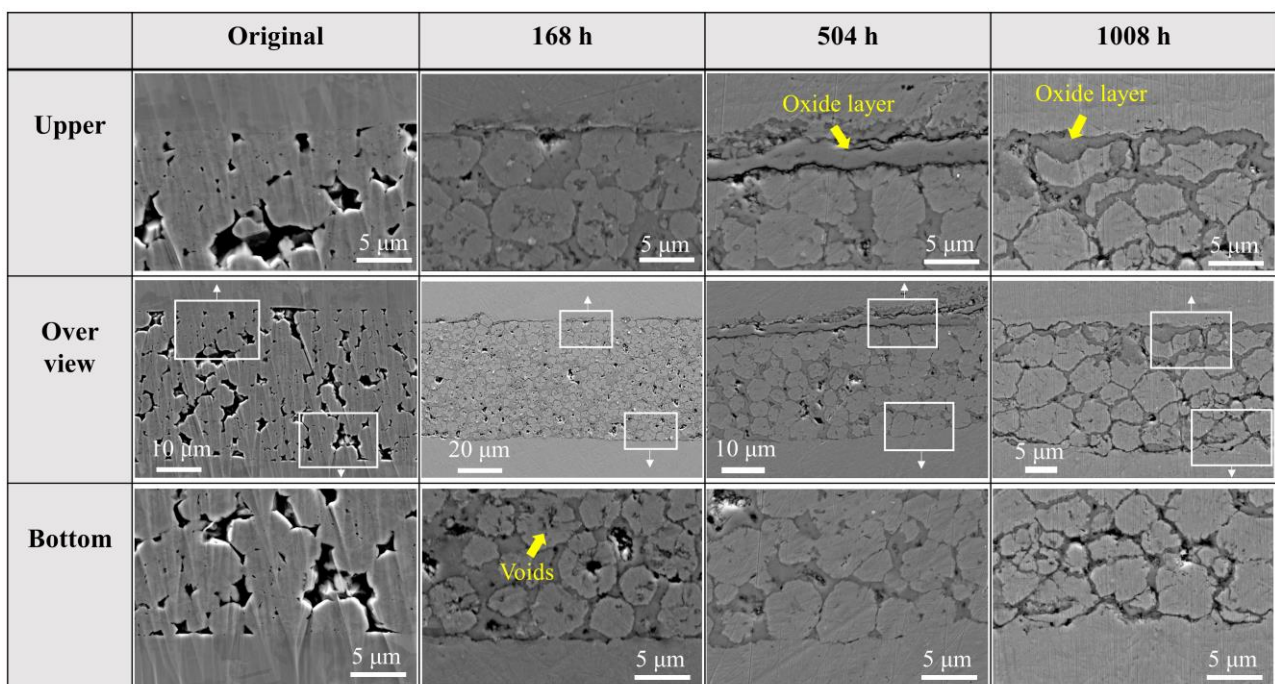


Figure 5.14 Cross-sectional SEM images of #4 joints after aging for different time

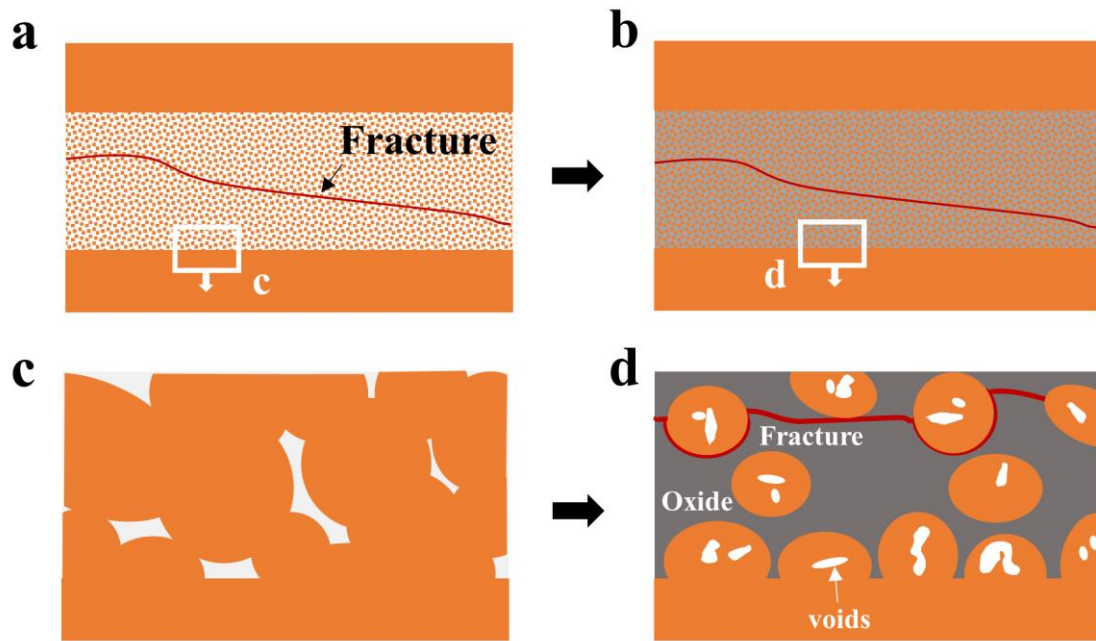


Figure 5.15 Schematic diagram of the fracture mode of the #4 joints before (a, c) and after aging (b, d).

gradually increased. There is an initiation of cracks in oxide propagating along the parent microparticles edge leading to failure in shear tests, as depicted in **Figure 5.15 d**.

5.3.5 Effects of substrates, and bonding methods on the long-term reliability of Cu microparticle-sintered joints

Comparing #3 joints with #4 joints, we conclude that the long-term reliability of sintered joints is primarily impacted through oxidation of sintered microstructures. The #3 joints, which were assembled by sintering Ag microparticles on the anti-oxidation ENIG substrates, maintained high shear strength during the high-temperature aging in the air; however, the #4 joints, which were assembled by the similar ultrasonic process, decreased in shear strength after the aging because the sintered matrix and substrates were composed of Cu. Moreover, shear strength of the #1 and #2 joints assembled by sintering of the Cu microparticles decreased even more significantly. Therefore, Thus, priority is placed on the prevention of packaging hermetic encapsulant failure, as well as oxygen infiltration so as to maintain reliability of Cu/Cu joints. In the case of Cu/Cu joints serving in exposed ambient, various means should be considered to improve the oxidation resistance of the whole component. By comparing shear strength and microstructural transformation of #1 - #4 joints, variables are controlled to discuss the influence of substrates and bonding method on the long-term reliability of Cu microparticle-sintered joints at high temperature.

The #1 joints and #2 joints were assembled by the similar process using the same microparticle, but the substrate of the former was Cu disk while that of the latter was ENIG disk. Both joints decreased

dramatically in shear strength after aging and failed naturally after aging for 1008 h due to the debonding of the sintered matrix. Little dissimilarities exist between the two joints regarding the decline in shear strength, interfacial debonding, and surface morphologies after debonding. According to the previous discussion, interfacial debonding occurs due to the formation of the oxide interlayer which induces considerable shear stress at interfaces because of its expansion, while whether substrate affects the formation of the oxide interlayer has not yet been investigated. Therefore, EPMA was conducted to analyze the cross-section of #1 and #2 joints after aging for 504 h, and results are shown in **Figure 5.16**.

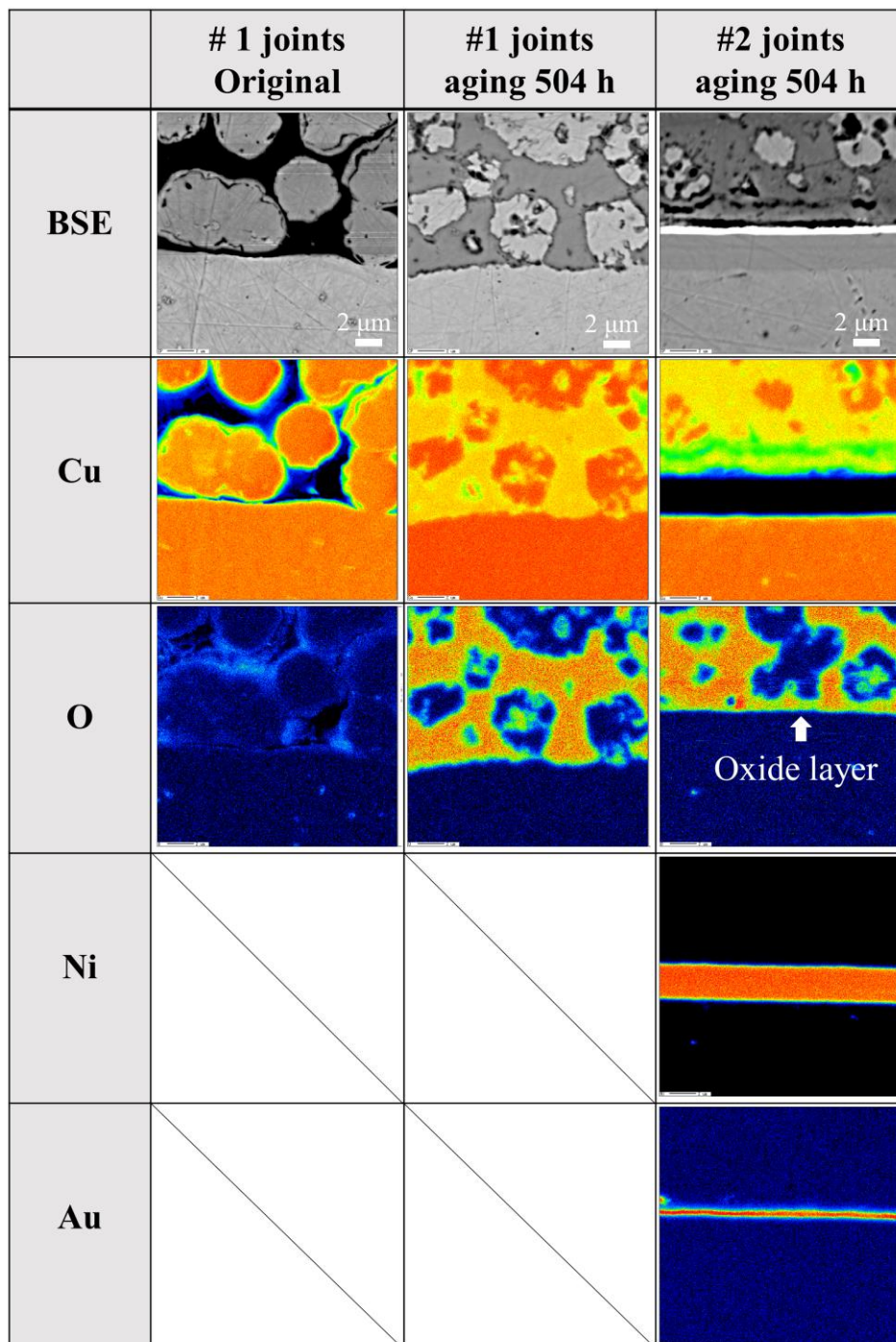


Figure 5.16 EMPA results showing element distribution at bonding interfaces of #1 and #2 joints before and after aging for 504 h.

As a result of the poor solid solubility between Cu and Au, the diffusion of Cu-Au is hardly noticed after aging, and there was no obvious enhancement of ENIG disk on microstructures. Additionally, regardless of which substrate was used, the continuous oxide layer formed at the sintered matrix/substrate interfaces; because the oxide layer is a result of particle and substrate oxidation. Thus, it is surmised that the formation of the continuous oxide interlayer is hardly prevented through the improvement of substrate antioxidant performance.

The #1 and #4 joints were obtained with the same Cu microparticle and the same Cu substrate, but the former were assembled by reductive sintering and the latter were assembled by the ultrasonic process with a pressure of 7 MPa. The two joints exhibited little difference in shear strength before the thermal aging (~26 MPa), while the difference became significant after the aging. The amount of oxide and interfacial oxide layers denoted the microstructure difference between the two joints. In the case of the #1 joint, preoxidized Cu microparticles were sintered under negligible pressure, and the reduction of Cu oxide during the process cause shrinkage of the sintered matrix; both factors lead to the formation of massive oxide by introducing a large number of oxygen paths. Contrastingly, internal stress, which was induced through pressure alongside ultrasonic vibration, residues within the sintered matrix, promoting elastic deformation that blocked oxygen pathways. As oxygen hardly infiltrates into the deformed interface, only distorted oxide formed in some portion; this apparently likewise causes oxide content of the #4 joints to be lower than that of the #1 joints. Therefore, shear strength of the #1 joints decreases with increasing aging time while that of the #4 joints does not until sufficient oxide formed in the sintered matrix to allow fractures to propagate through the whole joints. It is concluded that different methods lead to different behavior in thermal aging because they generate a sintered matrix with different density and different resistance to oxidation. Joints with dense sintered matrix and impact interfaces exhibit better reliability in the air at high temperatures.

5.4 Conclusions

In this chapter, the microstructural transformation of the joints fabricated using the processes presented in *Chapter 2-4* during the aging at 200 °C in the air were separately examined. By contrasting the joints assembled under various circumstances, factors impacting the long-term reliability of Cu sintered joints were examined, and the main conclusions are addressed thusly.

1. Oxidation denotes the main effect of the aging on the Cu-Cu bonding, which affects both shear strength and failure modes. Affecting by the formation of oxide, the Cu sintered-joints obviously

decreased in shear strength, and brittle fracture occurred at interfaces. By contrast, the Ag sintered-joints with high oxidation resistance are mainly affected by vacancy diffusion, which maintained high shear strength after aging.

2. As a result of the oxygen paths residue in the joints assembled through sintering procedure without applying pressure, continuous oxide interlayers that induces shear stress concentration were generated at the sintered matrix/substrate interface and eventually result in a natural debonding. The oxide interlayer is a combined product of microparticles and substrate oxidation; Thus, this issue is hardly improved by improvement of substrate antioxidant performance.
3. The joints assembled by the ultrasonic process exhibited the absence of the continuous oxide layer due to the tight bonding between the microparticles and substrate. Consequently, fracture mainly occurred within oxide in the sintered matrix. Adopting bonding processes that are capable of fabricating densified sintered microstructure may enhance the reliability of Cu-Cu bonding when it is exposed to ambient.

Reference

1. Khazaka, R., L. Mendizabal, and D. Henry, Review on joint shear strength of nano-silver paste and its long-term high temperature reliability. *Journal of electronic materials*, **43** (2014) 2459-2466.
2. Chua, S. and K.S. Siow, Microstructural studies and bonding strength of pressureless sintered nano-silver joints on silver, direct bond copper (DBC) and copper substrates aged at 300 C. *Journal of Alloys and Compounds*, **687** (2016) 486-498.
3. Hong, S. and C. Fu, Theoretical study on cracking behavior in two-phase alloys Cr–Cr₂X (X= Hf, Nb, Ta, Zr). *Intermetallics*, **9** (2001) 799-805.
4. Siow, K.S., *Die-Attach Materials for High Temperature Applications in Microelectronics Packaging*, Springer, (2019) 15-17.
5. Chen, C. and K. Suganuma, Microstructure and mechanical properties of sintered Ag particles with flake and spherical shape from nano to micro size. *Materials & Design*, **162** (2019) 311-321.
6. Fu, S., Y. Mei, X. Li, P. Ning, and G.-Q. Lu, Parametric study on pressureless sintering of nanosilver paste to bond large-area ($\geq 100 \text{ mm}^2$) power chips at low temperatures for electronic packaging. *Journal of Electronic Materials*, **44** (2015) 3973-3984.
7. Mayo, M.J., Processing of nanocrystalline ceramics from ultrafine particles. *International materials reviews*, **41** (1996) 85-115.
8. Wang, X., Y. Mei, X. Li, M. Wang, Z. Cui, and G.-Q. Lu, Pressureless sintering of nanosilver paste as die attachment on substrates with ENIG finish for semiconductor applications. *Journal of Alloys and Compounds*, **777** (2019) 578-585.
9. Yang, F., W. Zhu, W. Wu, H. Ji, C. Hang, and M. Li, Microstructural evolution and degradation mechanism of SiC–Cu chip attachment using sintered nano-Ag paste during high-temperature ageing. *Journal of Alloys and Compounds*, (2020) 156442.

Chapter 6

Summary and future works

6.1 Summary

In this dissertation, rapid die-attach processes have been developed to assemble reliable Cu/Cu joints at low temperatures using Cu microparticles, as alternatives to processes including soldering and the TLP bonding for high-temperature applications. To improve the poor sinterability of Cu microparticles at low temperatures, the reductive reaction was first involved in the bonding process, assembling robust sintered joints by promoting the formation of interfacial common phases. Then, to subsequently reduce the process time and the bonding temperature, the feasibility of introducing low-power ultrasonic vibration in the

bonding process was explored. The chestnut-burr-like Ag microparticle was used as filling materials to study the effects of the ultrasonic vibration on sintering and microstructural transformation of metallic microparticles. Under the influence of the ultrasonic vibration, the average shear strength of the Ag-sintered joints doubled within 150 s. In combination of the reductive reactions and the ultrasonic vibration, Cu spherical shapes microparticles were bonded at an actual temperature of 200 °C to assemble robust Cu/Cu joints within 15 min. Lastly, isothermal aging tests at 200 °C were conducted on the joints assembled through the above processes, simulating the situation where encapsulant fails in high-temperature services, to study the long-term reliability of the Cu/Cu joints and its transformation under different situation.

In chapter 1, discussion was provided on the background of power devices using wide bandgap (WBG) semiconductor and corresponding die-attach methods currently using for high-temperature applications. The Cu/Cu joints, which accommodate high temperatures and current encountered in WBG semiconductors service conditions, and corresponding bonding methods using Cu microparticles as filling materials were presented. Due to the poor sinterability of Cu microparticles, the development of the bonding process is highly challenging. Therefore, assisting approaches including reductive reactions and ultrasonic vibration were proposed, and their feasibility of assisting in bonding processes was estimated.

In chapter 2, we demonstrate and optimize a bonding process, which reductively sinters preoxidized Cu microparticles in a formic-acid atmosphere. Spherical Cu microparticles were preoxidized at 280°C for 30 min, then were made as paste and sintered in the formic acid atmosphere at 300 °C for 30 min to assemble Cu/Cu joints with average shear strength above 23 MPa. Based on the transformation of Cu microparticles at different preoxidation and following reduction intervals, the bonding mechanism of the microparticles in the process was revealed. It was found oxide fragments that formed in preoxidation intercalated between the Cu microparticles, then transformed into linkages in the reductive sintering. The generation of the linkages is critical for bonding quality and is driven by the reduction in surface energy during the transformation of free surfaces to grain boundaries.

In chapter 3, the feasibility of the low-power ultrasonic vibration assisting the bonding process and the effects of the ultrasonic vibration on sintered microstructures were studied using anti-oxidation chestnut-burr-like Ag microparticles. With the ultrasonic vibration, average shear strength of the joints assembled at 240 °C has been doubled to 36.2 MPa. Based on the characterization of sintered microstructures obtained with different ultrasonic time and power, the effects of the ultrasonic vibration were studied. Ultrasonic vibration was found to induce localized high temperatures and acoustic softening

effect. The materials are softened by the two effects, hence promoted plastic deformation and densification of Ag microparticles. Under the two effects, micro bridges and dense layers were generated; the former provided reliable bonding between the microparticles, and the latter reinforced the joints by eliminating brittle interfacial debonding.

In chapter 4, a low-temperature bonding process using Cu microparticles was successfully developed based on the findings observed in *Chapter 2* and *Chapter 3*, and the process parameters including protective solvents, heating profile, and process time were optimized. With the protection of L-ascorbic acid and glycerin and assisting of the ultrasonic vibration, Cu microparticles successfully bonded at 200 °C within 15 min, assembling Cu/Cu joints with an average shear strength of 27 MPa. Micro-region deformation and dislocation tangles were observed at the particle interface due to the acoustic softening effects and localized high temperature induced by the ultrasonic vibration. The two high-energy features consequently drove dynamic recrystallization at interfaces, achieving reliable bonding between Cu microparticles.

In chapter 5, the long-term reliability of the Cu/Cu joint and its transformation under different situations were studied. The sintered joints prepared through the processes in *Chapters 2 - 4* with different materials and substrates were isothermally aged at 200 °C in the air. Oxidation was found to be the main effect of the aging on the Cu/Cu joints, affecting both shear strength and failure modes. The Cu/Cu joints degraded because brittle fractures occurred due to the existence of oxide: continuous oxide interlayers tend to form between the sintered matrix and the substrate, inducing natural debonding. This issue was barely improved by the anti-oxidation plating on the substrates because the oxide layers were combined products of microparticle and substrate oxidation. However, the joints prepared with ultrasonic vibration exhibited the absence of the oxide layer, hence the better long-term reliability.

6.2 Environmental assessment on various die-attach materials and corresponding bonding processes

Based on the explanation in chapter 1, the bonding processes developed in this study are promising candidates for WBG die-attach methods and potentially replace soldering, TLP bonding process, and MNP sintering in high-temperature applications. On the basis of performance study, environmental aspects for practical use should also be evaluated. In this section, comparative investigation through a critical consideration was given attention to the perspective of materials used and process energy consumption to present an environmental assessment. Sn-37Pb high-temperature solder, Cu-Sn TLP

system, and Cu nanoparticles are picked to represent materials for soldering, TLP bonding, and MNP sintering, respectively.

The respective materials were assessed from the perspective of waste fluid produced in materials manufacturing, the toxicity of materials themselves, and additives in the paste or applied for procedures, as revealed in **Table 6.1**. The composition of Sn-37Pb solder pastes is ordinarily a combination of solder powders and fluxes, and the former is fabricated commercially through gas atomization from the molten solder alloy that did not generate any waste fluid [1]. Notwithstanding, the application of Pb-based solder has been forbidden in most electronics because of its pollution and toxicity as discussed in Chapter 1. Furthermore, additives such as fluxes are inevitable for soldering processes to protect molten solder and promote spreading, which equally contain organic acid and surfactants, and various solvents. Cu-Sn TLP bonding adopts materials in form of sheet [2] or coating particles [3]; the former is fabricated by mechanical rolling that produces no waste fluid, and the later is fabricated by matured electroplating processes, which produce electroplating wastes that can be purified in a variety of sophisticated methods [4]. Cu and Ag nanoparticles are commercially fabricated by chemical synthesise. Strong reductive agents such as hydrazine and sodium borohydride are widely used in the synthesise, which are extremely toxic, polluting, and barely removed by usual solution and degradation [5]. Furthermore, it has been reported that nanoparticles exhibit biological effects on the environment, and therefore the large-scale commercial application of nanoparticles remains currently controversial [6]. The metallic microparticles are usually fabricated by the gas atomization method that produces no waste fluid. Additionally, the Cu and Ag

Table 6.1 Comparison of various die-attach materials in term of the environmental perspective [2, 3, 7-9]

	Waste fluid	Toxicity of materials	Additives	Summary	Ref.
Sn-37Pb solder	-	Toxic of Pb	Fluxes containing surfactants, reductive agent.	Forbidden	[7]
Cu-Sn TLP systems	-	-	-	Good	[2, 3]
Cu MNPs	hydrazine, sodium borohydride, etc.	Pollution of nanoparticles	Dispersant, reductive agents	Poor	[8, 9]
Cu/Ag MNPs	-	-	Glycol, terpeneol, ascorbic acid, glycerol	Good	This study

microparticles are non-toxic and have been used widely in powder metallurgy. The additives in the paste are L-ascorbic acid and glycerin; both are common products in nature, and no toxic issue arises.

The environment assessment of corresponding processes is evaluated and compared in the perspective of energy consumption (involving process temperature and process time) and gas waste, as shown in **Table 6.2**. The soldering of Sn-37Pb, which has been widely used before, is capable of assembling reliable joints with relatively low temperatures and short process time. A protective atmosphere is usually unnecessary because of the fluxes application, while fluxes probably result in a minute proportion of stream or decomposition products during processing. The TLP bonding process of the Cu-Sn system, as well as Cu-MNP sintering, is ordinarily protected through an inert gas, such as N₂, which barely affects the environment as an emission. Their long process time (above 30 min) and high process temperature (300 °C), however, consumes much energy. As for processes introduced in this dissertation, the waste gas produced in the reductive sintering process is mainly unconsumed formic acid vapor, which could be collected using a purifier. Nevertheless, its purification efficiency, especially for utilization in large-scale industries, is still in need of further clarification. The ultrasonic process is conducted in ambient air and produces no waste gas. Moreover, there is less energy consumption as joints are heated through the hotplate for a shorter time, unlike other techniques executed via furnaces where there is need to preheat the entire chamber before heating of joints.

Table 6.2 Comparison of various die-attach process [2, 3, 7, 10, 11]

	Energy consuming		Waste gas	Shear strength	Summary	Ref.
	Process temp.	Process time				
Sn-37Pb soldering	220-250 °C	7 min	Possible flux decomposition	63 MPa	Good	[7, 10]
Cu-Sn TLP	300 °C	30 min	N ₂	25 MPa	Acceptable	[2, 3]
Cu MNPs sintering	300 °C	60 min	N ₂	34 MPa	Acceptable	[11]
Reductive sintering	300 °C	40 min	Formic acid gas	28 MPa	Poor	This study
Ultrasonic process (Cu)	240 °C	15 min	-	27 MPa	Good	This study

6.3 Future work

6.3.1 Optimization of the reductive sintering process

The reductive sintering of MMPs, which is presented in *Chapter 2*, is a die-attach bonding process with excellent compatibility for various furnaces and facilities. The preoxidized Cu microparticles were bonded because the interfacial reaction generates a common phase. However, the penetration of formic acid towards the center sintered matrix and the reduction of Cu are time-consuming; therefore, the whole process time too long for practical industries, and components have to be exposed to the acid atmosphere for a long time. Therefore, the optimization of this process is necessary from the perspective of shortening process time and reducing acid atmosphere.

One possible way is to adopt a catalyst to accelerate the reaction and decomposition of formic acid vapor so that components contact with deacidified reactants. The key point is to ensure reductive reactions occur at particle interfaces to maintain the high-rate reaction-controlled diffusion. It has been reported that Pt-catalyzed formic acid vapor could reduce Ag_2O into pure Ag, realizing robust Ag-sintered joints at 160 °C [12]. Another possible way is to develop filling pastes that decomposed into pure metals at high temperatures (e. g. Cu formate), generating a common phase at particle interfaces to achieve bonding. The decomposition is supposed to occur spontaneously at high temperatures without the participation of any reactant; therefore, the slow infiltration of gas into the sintered matrix is avoided, and the process time can be shortened.

6.3.2 Improvement of the ultrasonic process and other antioxidation methods

Although the ultrasonic-assisted process for the Cu/Cu joints, introduced in *Chapter 4*, drives dynamic recrystallization of the microparticles to achieve bonding rapidly, the pressure of 7 MPa((50 N) is inevitable for the efficiency of ultrasonic vibration propagation. However, applying pressure is not desirable in die-attach processes because it may damage the circuit on the semiconductors and lead to the failure of chips. Therefore, reduce in loading pressure, as well as the applied position of ultrasonic vibration, is necessary to be further optimized.

One possible way is applying ultrasonic vibration directly to the sintered matrix instead of the substrate or the semiconductor. For example, ultrasonic waves could be applied to microparticles to induce natural vibration in the process; however, further investigation is needed on this feasibility because the ultrasonic waves have been reported to mainly affect molten metals, causing cavitation and convection effects, effects on particle solid sintering at low temperature are barely studied. Additionally, as shown in

Figure 4.9, although the oxide content detected in the sintered matrix was relatively low (<5 at.%), the carbon contents, which is the main indicator for estimating organic residues, were relatively high. The organic residues could adversely affect thermal and electrical conductivities of sintered joints; therefore, adjusting the formula of protective solvent and looking for alternative environment-friendly anti-oxidation approaches are necessary to achieve higher protection efficiency and reduce additives. The inert gas such as N₂, for example, could be adopted as a protection atmosphere.

6.3.3 Reliability assessment of proposed bonding processes for real application

The die-attach processes proposed in *Chapter 2 - 4* are currently developed at the preliminary stage, tested using cylinder bulk materials in this dissertation; however, they have not yet been applied to practical die attaching. Therefore, to apply the processes to bond chips on the widely used direct bonding copper (DBC) substrate is planned, to evaluate the mechanical, thermodynamic, and electrical performances and explore the possible reliabilities.

The GaN or Si chips and the DBC substrates (which is a common substrate for high-temperature die-attach) are suitable for practical testing. Additionally, despite the studies on the long-term reliability of the joints obtained with different processes and the transformation of the sintered microstructures during aging, several reliability issues under other conditions such as thermal shock are needed to address. Due to the mismatch of coefficient of thermal expansion (CTE) between the sintered matrix and chips or even substrates, the thermal shock and thermal cycle in practical use will cause periodic stress, which results in fatigue failure of the sintered matrix or the breakage of the chips. Therefore, it is necessary to conduct thermal cycling tests with standards such as MIL-STD-883H on the assembly to investigate possible internal defects by non-destructive characterization. Additionally, the study on microstructural transformation after thermal cycling and hermetic aging could provide a better understanding of the microstructural evolution of Cu/Cu joints in practical serving. In the same way, power cycling that offers similar temperature and current swing should also be carried out on the assembly. In summary, the reliability of the practical assembly should be further verified by a series of standard tests such as thermal and power cycling.

Reference

1. Yan, J., D. Zhu, Y. Liu, and J. Xu, Effect of Aging Treatment on Microstructural Evolution of Rapidly Solidified Eutectic Sn-Pb Alloy Powders. *Applied Sciences*, **9** (2019) 392.
2. Lee, B.-S., S.-K. Hyun, and J.-W. Yoon, Cu–Sn and Ni–Sn transient liquid phase bonding for die-attach technology applications in high-temperature power electronics packaging. *Journal of Materials Science: Materials in Electronics*, **28** (2017) 7827-7833.
3. Liu, X., S. Zhou, and H. Nishikawa, Thermal stability of low-temperature sintered joint using Sn-coated Cu particles during isothermal aging at 250 °C. *Journal of Materials Science: Materials in Electronics*, **28** (2017) 12606-12616.
4. Šćiban, M., B. Radetić, Ž. Kevrešan, and M. Klašnja, Adsorption of heavy metals from electroplating wastewater by wood sawdust. *Bioresource Technology*, **98** (2007) 402-409.
5. Xianghong, R., The Hydrazine Fuels and the Environment Pollution [J]. *Inner Mongolia Environmental Protection*, **4** (2001), 1.
6. Taghavi, S.M., M. Momenpour, M. Azarian, M. Ahmadian, F. Souri, S.A. Taghavi, M. Sadeghain, and M. Karchani, Effects of nanoparticles on the environment and outdoor workplaces. *Electronic physician*, **5** (2013) 706.
7. Islam, R., B. Wu, M. Alam, Y. Chan, and W. Jillek, Investigations on microhardness of Sn–Zn based lead-free solder alloys as replacement of Sn–Pb solder. *Journal of alloys and compounds*, **392** (2005) 149-158.
8. Li, J., X. Yu, T. Shi, C. Cheng, J. Fan, S. Cheng, G. Liao, and Z. Tang, Low-temperature and low-pressure Cu–Cu bonding by highly sinterable Cu nanoparticle paste. *Nanoscale research letters*, **12** (2017) 1-6.
9. Wu, S.-H. and D.-H. Chen, Synthesis of high-concentration Cu nanoparticles in aqueous CTAB solutions. *Journal of colloid and interface science*, **273** (2004) 165-169.
10. Gan, G., D. Xia, X. Liu, C. Liu, H. Cheng, Z. Ming, H. Gao, D. Yang, and Y.-p. Wu, Microstructure and Property of Sn–37Pb Solder Bumps in Ø0.6 mm Ball during Thermal Shock. *MATERIALS TRANSACTIONS*, **60** (2019) 364-368.
11. Ishizaki, T., A. Kuno, A. Tane, M. Yanase, F. Osawa, T. Satoh, and Y. Yamada, Reliability of Cu nanoparticle joint for high temperature power electronics. *Microelectronics Reliability*, **54** (2014) 1867-1871.

12. He, L., J. Li, X. Wu, F. Mu, Y. Wang, Y. Lu, and T. Suga, Robust Ag-Cu Sintering Bonding at 160° C via Combining Ag₂O Microparticle Paste and Pt-Catalyzed Formic Acid Vapor. *Metals*, **10** (2020) 315.

Research achievements

I List of publications

Peer-reviewed journal articles

1. **Gao, R.**, He, S., Shen, Y. A., & Nishikawa, H. (2019). Effect of Substrates on Fracture Mechanism and Process Optimization of Oxidation–Reduction Bonding with Copper Microparticles. *Journal of Electronic Materials*, 48(4), 2263-2271.
2. **Gao, R.**, He, S, Shen, Y, A, Jiahui Li & Nishikawa, H (2020). Pressuless Cu-Cu bonding using pre-oxidized Cu microparticles and formic acid. *Journal of Materials Science: Materials in Electronics*, (2020) 31:14635–14644.
3. **Gao, R.**, Shen, Y. A., Li, J., He, S., Nishikawa, H. (2020). Mechanical and Microstructural Enhancements of Ag Microparticle-sintered Joint by Ultrasonic Vibration. *Journal of Materials Science: Materials in Electronics*, (2020) 31: 21711–21722.
4. He, S., **Gao, R.**, Li, J., Shen, Y. A., & Nishikawa, H. (2019). In-situ observation of fluxless soldering of Sn-3.0 Ag-0.5 Cu/Cu under a formic acid atmosphere. *Materials Chemistry and Physics*, 122309.
5. He, S., **Gao, R.**, Yu-An Shen, Jiahui Li, Hiroshi N. (2020). Wettability, Interfacial Reactions, and Impact Strength of Sn-3.0Ag-0.5Cu Solder/ENIG Substrate Used for Fluxless Soldering under Formic Acid Atmosphere. *Journal of Materials Science*, 55, 3107–3117.
6. Shen, Y. A., Lin, C. M., Li, J., & **Gao, R.**, & Nishikawa, H. (2019). Suppressed Growth of (Fe, Cr, Co, Ni, Cu) Sn₂ Intermetallic Compound at Interface between Sn-3.0 Ag-0.5 Cu Solder and FeCoNiCrCu 0.5 Substrate during Solid-state Aging. *Scientific reports*, 9(1), 10210.

Conference proceedings

1. **Gao, R.**, Li, J., Shen, Y. A., & Nishikawa, H., A Cu-Cu Bonding Method Using Preoxidized Cu Microparticles under Formic Acid Atmosphere, in 2019 International Conference on Electronics Packaging (ICEP2019), 2019.
2. **Gao, R.**, Li, J., He, S. and Hiroshi Nishikawa, H., A Pressureless All-Cu Bonding Method by Reduction of Preoxidized Cu Microparticles, in the 2019 International Symposium on Advanced Power Packaging (ISAPP2019), 2019.
3. He, S., **Gao, R.**, Li, J. and Nishikawa, H., Sn Steaming phenomenon under formic acid atmosphere. In

the 5th international symposium on visualization in Joining & Welding Science through Advanced Measurements and Simulation (Visual-JW2019), 2019.

II List of presentations

1. (Poster) Japan-Taiwan Workshop on Electronic Interconnection II, 2018, Mie, Japan
2. (Poster) 4th Osaka Uni-JWRI/NTU-MSE Workshop, 2019, Taipei, Taiwan, China
3. (Oral) 2019 International Conference on Electronics Packaging (ICEP2019), 2019, Niigata, Japan
4. (Poster) 2019 International Symposium on Advanced Power Packaging (ISAPP2019), 2019, Osaka, Japan

Acknowledgment

Firstly, I would like to express my sincere gratitude to my advisor: Prof. Hiroshi Nishikawa for his valuable advice and patient support during my Ph. D program. His careful guidance helped me a lot in this thesis and will continuously affect me in my future academic career. Additionally, thank the rest of my thesis committee: Prof. Soshu Kirahara and Prof. Yuji Ohishi, for their insightful comments and professional suggestion that incited me to widen my research from different perspectives.

I would also like to thank unknown reviewers who reviewed my articles for their great guidance and help, no matter the decisions are acceptance or rejection. I will remember their selfless contribution and continue spreading this spirit in the academic world. Additionally, thank China Scholarship Council (CSC) for doctoral research assistantships.

My special thanks are given to Mrs. Alexandra Elbakyan for her great assistance in the literature reference during the COVID-19 epidemic period.

Last but not the least, I would like to thank my parent and my wife, for their support, understanding, and selfless love; I would never go that far without them.